Turbulence transition in pipe flow

DISSERTATION

zur Erlangung des Doktorgrades
der Naturwissenschaften
(Dr. rer. nat.)

dem Fachbereich Physik
der Philipps-Universität Marburg
vorgelegt

von
Holger Faisst
aus Böblingen

Marburg/Lahn 2003

Vom Fachbereich Physik der
Philipps-Universität Marburg als
Dissertation angenommen am: 08.07.2003
Erstgutachter: Prof. Dr. Bruno Eckhardt
Zweitgutachter: Prof. Dr. Peter Lenz
Tag der mündlichen Prüfung: 22.07.2003

Turbulence transition
in pipe flow

or, in Lord Reynolds' words

A Numerical Investigation of the Circumstances which determine whether the Motion of Water shall be Direct or Sinuous

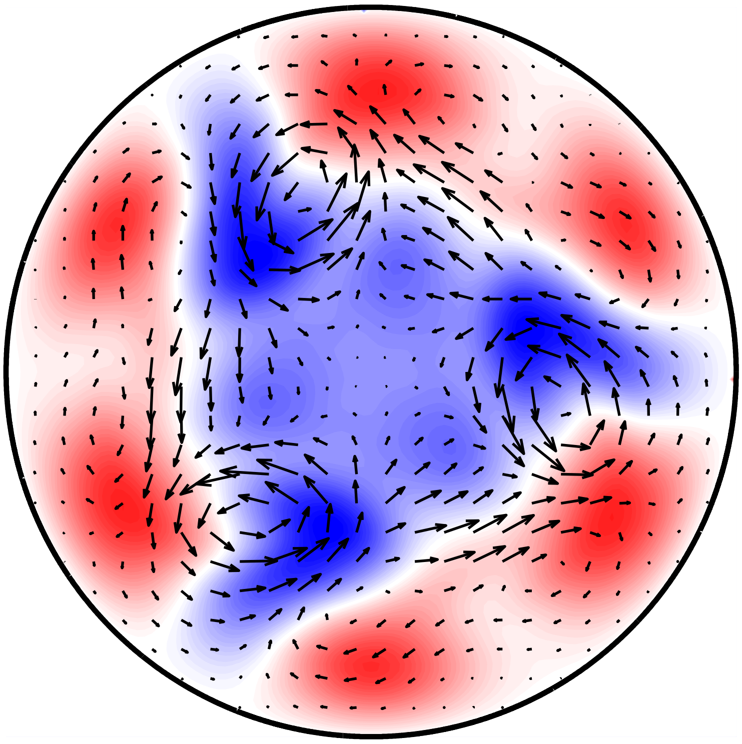

Contents

List of figures

1 Überblick

1.1 Einleitung

Turbulenz ist ein Alltagsphänomen, das ebenso faszinierend wie in weiten Teilen unverstanden ist. Die Entstehung von Turbulenz ist selbst für manch klassische Scherströmungen mit einfachster Geometrie ein noch ungelöstes Problem, obwohl diese schon seit Jahrzehnten intensivst untersucht werden.

Wann und wie werden Scherströmungen turbulent? Für eine Annäherung an diese Frage kann man Scherströmungen, je nach der Stabilität ihrer laminaren Grundströmung, zunächst in zwei Klassen einteilen, deren unterschiedliche Transitionsszenarien jetzt vorgestellt werden.

Da sind zum einen die Scherstömungen, bei denen der Turbulenzübergang von der linearen Instabilität der laminaren Grundströmung bestimmt wird. Ihre berühmtesten und ausführlichst untersuchten Vertreter sind das thermisch getriebene Rayleigh-Bénard System im Schwerefeld, und das zentrifugal getriebene Taylor-Couette System zwischen zwei rotierenden, konzentrischen Zylindern. Im folgenden wollen wir den Übergang am Taylor-Couette System mit rotierendem Innenzylinder exemplarisch vorstellen. Für diese Diskussion benötigen wir den zentralen dimensionslosen Parameter in der Hydrodynamik, die Reynoldszahl, die wir hier zunächst einmal nur als ein Maß für die Stärke des Antriebs der Strömung auffassen wollen. Unterhalb einer gewissen, sehr kleinen, Reynoldszahl, d.h. bei einem nur sehr schwachen Antrieb, ist die laminare Strömung der einzige Zustand, der asymptotisch angenommen werden kann. Jede beliebige Störung dieses Zustands zerfällt hier monoton. Deutlich oberhalb dieser sogenannten Energie-Reynoldszahl, gibt es eine wohldefinierte, erste krititsche Reynoldszahl, bei der das vormals linear stabile Grundprofil linear instabil und damit repulsiv wird. Das heißt, infinitesimale Abweichungen vom Grundprofil werden nicht mehr gedämpft sondern wachsen exponentiell an. Die Strömung entfernt sich dabei vom laminaren Profil und relaxiert dann durch den Einfluss von schwach nichtlinearen Effekten auf ein sekundäres Strömungsmuster. Im Falle des Taylor-Couette Systems mit rotierendem Innenzylinder sind das z.B. die Taylor-Wirbel. Dies ist ein stationärer Strömungszustand der aus Paaren von gegeneinander rotierenden Wirbeln besteht, die sich wie Tori um den Innenzylinder winden. Dabei wird die kontinuierliche axiale Translationssymmetrie in eine diskrete Translationssymmetrie gebrochen, d.h. der neue Zustand hat geringere Symmetrie und etwas mehr räumliche Struktur, die aber immer noch sehr einfach ist. Diese primäre Bifurkation ist im Rahmen der klassischen linearen Stabilitätstheorie sehr gut verstanden; es gibt präzise Übereinstimmung zwischen einfacher Numerik und unzähligen Experimenten. Dieser erste Übergang ist sogar von analytischen Modellen quantitativ erfassbar [31]. Wenn man die Reynoldszahl ausgehend von diesem sekundären Zustand ein wenig weiter erhöht, kann man mit Hilfe von schwach nichtlinearen Theorien die Entwicklung des Zustands gut nachvollziehen. Bei einer etwas höheren zweiten kritischen Reynoldszahl wiederholt sich derselbe Vorgang noch einmal: Der sekundäre wird nun seinerseits linear instabil, es kommt zu einer weiteren Symmetriebrechung und die Strömung relaxiert schwach nichtlinear auf einen tertiären Zustand. Im Taylor-Couette System entspricht dies z.B. dem Brechen der kontinuierlichen axialen Rotationssymmetrie des Taylor-vortex flow und einer Relaxation in eine diskrete Rotationssymmetrie des sogenannten “wavy-vortex flow”. Dies ist ein zeitlich periodischer Zustand, bei dem die Wirbelschläuche azimuthal moduliert sind, und der in einem geeignet mitrotierenden System stationär ist. Dies setzt sich erst mal so fort, wobei sich die Abfolge der Zustände folgendermaßen darstellt: laminares Grundprofil, Taylor-Wirbel, wavy-vortex flow, modulierter wavy-vortex flow, turbulente Taylor-Wirbel. Durch eine Folge von symmetriebrechenden Bifurkationen wird die Struktur der anfänglich trivialen laminaren Strömung also Schritt für Schritt nachvollziehbar komplizierter. Sie bleibt dabei aber immer noch sehr glatt und regelmässig. Die Anzahl der dabei dynamisch aktiven Freiheitsgrade nimmt nur sehr langsam zu. Diese Folge geht jedoch nicht endlos so weiter. Wenn die modulierten Wellen instabil werden, ist die entstehende Dynamik nicht mehr länger glatt sondern unregelmäßiger und komplexer. Dennoch sind die großen Wirbelstrukturen weiterhin dominant; es handelt sich um eine niederdimensionale, chaotische Bewegung. Mit steigender Reynoldszahl wird diese allmählich immer kleinskaliger und schließlich auf so vielen räumlichen und zeitlichen Skalen dynamisch aktiv, dass man sie turbulent nennt. Die Dynamik spielt sich bei all diesen Strömungen auf Attraktoren ab, welche entweder eine reguläre und einfache Dynamik zeigen oder chaotisch sind. Zu ersteren gehören die stationären, zeitlich periodischen oder quasiperiodischen Zustände. Bei diesen gibt es zum Teil durchaus eine Koexistenz von Attraktoren im Phasenraum. Es hängt also nicht nur vom Systemparameter, der Reynoldszahl, ab, welcher Strömungszustand sich einstellt, sondern auch von den Anfangsbedingungen, von denen aus sich die Strömung genähert hat. So gibt es z.B. im Taylor-Couette System viele stabile Zustände von moduliertem wavy-vortex flow, die sich nur in den Wellenlängen voneinander unterscheiden. Bei den turbulenten Taylor-Wirbeln und deren immer komplexer werdenden Dynamik handelt es sich um eine Bewegung auf einem chaotischen Attraktor. Auch dies ist ein zeitlich invariantes Phasenraumobjekt, das die innerhalb seines Attraktionsgebiets liegenden Trajektorien, d.h. Strömungen, anzieht. Das Übergangsszenario in einer solchen von linearen Instabilitäten dominierten Scherströmung stellt sich also folgendermaßen dar: bei einer Abfolge genau bestimmbarer kritischer Reynoldszahlen wird durch symmetriebrechende Vorwärtsbifurkationen die Strömung Schritt für Schritt komplizierter, bis sich schließlich eine turbulente Strömung auf einem chaotischen Attraktor einstellt.

Ganz anders ist die Situation für die Klasse von Scherströmung ohne lineare Instabilität. Zu dieser Klasse gehören die Strömung durch ein Rohr mit kreisförmigem Querschnitt, die ebene Couette Strömung zwischen ebenen, gescherten Platten sowie die druckgetriebene Strömung zwischen parallelen Platten, die ebene Poiseuille Strömung, deren lineare Instabilität bei relativ hohen Reynoldszahlen liegt. Den Turbulenzübergang für diese Klasse von Strömungen wollen wir am Beispiel der in dieser Arbeit numerisch untersuchten Rohrströmung vorstellen. Die ersten experimentellen Untersuchungen des Turbulenzübergangs gehen hier bis zurück in das Jahr 1883, in dem Osborne Reynolds seine berühmten Experimente veröffentlichte [68]. Bereits Reynolds konnte zeigen, dass es bei guter Präparation des Experiments auch bei sehr hohen (später nach ihm benannten) Reynoldszahlen[1] noch möglich ist, die laminare Grundströmung zu realisieren. Der Grund dafür ist, dass das laminare, parabolische Hagen-Poiseuille Profil in der Rohrströmung linear stabil für alle Reynoldszahlen ist. Nur für sehr kleine Reynoldszahlen ($Re < 81.5$) ist sie nachgewiesenermaßen die einzige und global attraktive Lösung [72]. In einer Vielzahl von Experimenten $[19, 30, 68, 95, 96]$ konnte ab einem Reynoldszahlbereich von ca. 1800 bis 2300 turbulente Dynamik beobachtet werden. Dabei kann es sich zum einen um den 'natürlichen' Übergang aufgrund unvermeidbarer Störungen insbesondere am Einlassbereich des Rohres handeln. Dieser tritt abrupt und unvermittelt auf und führt zu einem stark intermittenten Wechsel von laminaren und turbulenten Bereichen. Zum anderen können gezielt Störungen von außen eingebracht werden, wie in den für diese Arbeit relevantesten Experimenten von Darbyshire & Mullin [19]. In diesen Experimenten zeigte sich, dass es stark von Details des experimentellen Aufbaus sowie der Struktur zusätzlich eingebrachten Störungen abhängt, ob Transition erfolgt oder nicht. Experimentell konnte bisher nur die laminare oder die turbulente Strömung realisiert werden, sowie der intermittente Wechsel zwischen beiden. Dabei zeigen die turbulenten Bereiche von Anfang an eine hochdimensionale und komplexe Dynamik. Es kommt dabei zur Bildung großskaliger, reproduzierbarer Strukturen, sogenannten "puffs" und "slugs". Für die Rohrströmung sind bisher keinerlei Strömungszustände von mittlerer Komplexität oder mit wenigen beteiligten Freiheitsgraden bekannt. Damit fallen weitere methodische Zugänge aus, wie z.B. schwach nichtlineare

---

[1] Die Reynoldszahl ist für die Rohrströmung definiert als

$$Re \equiv \frac{(\text{mittlere Strömungsgeschwindigkeit}\, U) \times (\text{Rohrdurchmesser}\, D)}{\text{kinematische Viskosität}\ \nu}$$

Ansätze über Amplitudengleichungen. Verglichen mit linear instabilen Scherströmungen erfordert ein Verständnis des Turbulenzübergangs hierbei andere konzeptuelle Zugänge. Lineare Stabilitätstheorie, die so erfolgreich für zentrifugal und thermisch getriebene Instabilitäten ist, versagt bei diesen von Scherkräften dominierten Strömungen. Es kommt nicht einmal zu einer qualitativen Veränderung des Eigenwertspektrums bei Reynoldszahlen, ab denen eine turbulente Dynamik beobachtet werden kann.

Der Turbulenzübergang in der Rohrströmung ist also durch starke Intermittenz, eine große Unsicherheit und schlechter Reproduzierbarkeit in den Übergangs-Reynoldszahlen und einer empfindlichen Abhängigkeit von Anfangsbedingungen gekennzeichnet. Eine Auswahl grundlegender experimenteller Ergebnisse zur Transition in Rohrströmungen wird in Kapitel 3 präsentiert, um eine breitere Diskussionsgrundlage für unsere Untersuchungen und Ergebnisse zu schaffen.

Diese je nach Stabilität des Grundprofils völlig verschiedenen Transitionsszenarien können in einem sehr instruktiven Experiment miteinander in Verbindung gebracht werden [33]. Im Taylor-Couette System gibt es die Möglichkeit (insbesondere numerisch) die Radien der Zylinder beliebig groß werden zu lassen, so dass man sich asymptotisch der ebenen Couette Strömung nähert. Das heißt, es steht ein kontinuierlicher Geometrieparameter zur Verfügung, mit dessen Hilfe man die kritische Reynoldszahl der linearen Instabilität des Grundprofils stetig verschieben kann, im Limes der ebenen Couette-Strömung sogar bis unendlich. Dabei verschiebt sich natürlich auch das Transitionsszenario von einem von linearen Instabiliäten und attraktiven kohärenten Strukturen dominierten Übergang hin zu einem stark intermittenten Übergang mit einer sofort hochdimensionalen Dynamik. Es hat sich dabei gezeigt, dass Zustände, die aus höheren Bifurkationen stammen, also nicht direkt mit dem laminaren Profil verbunden sind, wie z.B. der tertiäre wavy-vortex flow, durchaus bei etwa den gleichen Reynoldszahlen weiterexistieren können; sogar bis in den Bereich hinein, in dem es keine lineare Instabilität des laminaren Profils mehr gibt. Der entscheidende Punkt ist, dass aus der sekundären Vorwärtsbifurkation eine Rückwärtsbifurkation wird, die zu kleineren Reynoldszahlen hinführt. Im Limes der ebenen Strömung können tertiäre Zustände also nicht mehr aus sekundären Bifurkationen entstanden sein. Vielmehr enstehen sie nun aus Sattel-Knoten-Bifurkationen bei einer kritischen Reynoldszahl, ohne jede Verbindung zum laminaren Profil also gewissermaßen aus dem Nichts. Man nennt dies auch eine Bifurkation aus dem Unendlichen. Die Zustände verlieren dabei in der Regel ihre lineare Stabilität und werden repulsiv, das heißt linear instabil. Aber damit haben sie ihre dynamische Relevanz nicht verloren, sie hat sich jedoch verändert. Auch wenn sie nicht mehr das bisherige große und zum Teil globale Attraktionsgebiet haben, so besitzen sie dennoch eine hochdimensionale stabile Mannigfaltigkeit und nur wenige instabile Richtungen. Obwohl linear instabil existieren diese Strukturen weiterhin im Phasenraum, wo sie gewissermaßen als ordnendes Element wirken. Transient sind sie durchaus in der Lage, Trajektorien entlang ihrer stabilen Mannigfaltigkeit anzuziehen, bevor diese dann entlang der instabilen Mannigfaltigkeit wieder entweichen und vielleicht in das Attraktionsgebiet eines weiteren kohärenten Zustands gelangen. Bei einem genügend dichten Geflecht aus solchen Zuständen ist ein Wandern zwischen ihnen über lange Zeiträume möglich, bis die Dynamik schließlich doch wieder zerfällt, das heißt wieder laminar wird. Solch eine Dynamik, die auf dem chaotischen Streuen zwischen linear instabilen Zuständen basiert, ist also zunächst einmal nur transient, existiert also nur für eine endliche Zeit. Die Menge der instabilen Zustände bildet also keinen chaotischen Attraktor sondern einen chaotischen Repellor, aus dem Trajektorien mit einer von der Reynoldszahl abhängigen charakteristischen Entweichrate wieder zu einer laminaren Strömung zerfallen. Eine feste mittlere Entweichrate hat eine exponentielle Verteilung der Zeiten, die eine Trajektorie turbulent bleibt, also ihrer turbulenten Lebensdauer, zur Folge. Diese wurde in der ebenen Couette Strömung experimentell [9] und auch numerisch [74] nachgewiesen sowie numerisch auch in Parameterbereichen der Taylor-Couette Strömung identifiziert [27]. Unter anderem dadurch wurde die Existenz eines Repellors in diesen Systemen bestätigt. Der Repellor und das laminare Profil sind nun koexistierende, invariante Phasenraumobjekte, die beide ein endliches, komplexes Attraktionsgebiet haben [33, 73]. Selbst das laminare Attraktionsgebiet ist keineswegs einfach, sondern in manchen ausgezeichneten Richtungen hoher Symmetrie sogar unbeschränkt.

Das Ziel der vorliegenden Arbeit ist es, die Natur des Turbulenzübergangs in der Rohrstömung zu identifizieren. Dabei soll insbesondere untersucht werden, inwieweit die Interpretation der Transition in Couette-Strömungen, durch eine Repellorbildung aus kohärenten Zuständen, auf die Rohrströmung übertragbar ist. Ein tieferes Verständnis der nichtlinearen Mechanismen in der Rohrströmung ist von grundlegender theoretischer Bedeutung für eine der ältesten klassischen Fragestellungen in der Hydrodynamik. Weiterhin sind Strömungen durch Rohre auch von großer technischer Bedeutung. Besonders Mechanismen, die zu einer Reduktion der Turbulenzintensität führen und damit den Strömungswiderstand senken, sind von größtem Interesse.

Bei einer Annäherung an diese Ziele konnten auf zwei unterschiedlichen Feldern Ergebnisse durch direkte numerische Simulation gewonnen werden, die nach einer kurzen Darstellung der Numerik aufgezeigt werden.

1.2 Direkte numerische Simulation

Es ist bemerkenswert, dass so viele Fragen der Turbulenzforschung noch ungeklärt sind, wo doch die zugrundeliegenden Bewegungsgleichungen seit 150 Jahren bekannt sind. Dies ist auf die ungeheure Komplexität und Vielfalt der Lösungsstruktur und die große Zahl der dynamisch aktiven Freiheitsgrade zurückzuführen.

Ein zentraler Anteil dieser Arbeit bestand darin, ein neues, für unsere Aufgaben optimiertes numerisches Simulationsprogramm zu entwickeln, dass unsere Untersuchungen der dreidimensionalen Rohrströmung erst ermöglichte. Bei den zu lösenden Bewegungsgleichungen handelt es sich um die Navier-Stokes-Gleichungen für ein inkompressibles, newtonsches Fluid. Dies sind nichtlineare, partielle Differentialgleichungen, die zusammen mit verschiedenen Rand- und Nebenbedingungen gelöst werden mussten. Hierbei konnten wir auf fundierte Erfahrungen aus Simulationen von Couette-Scherströmungen zurückgreifen. Dabei erwies sich die Rohrströmung in vielerlei Hinsicht als ein numerisch deutlich komplexeres Problem als die Couette Strömungen, was insbesondere auf die Koordinatensingularität in den dem Problem angemessenen Zylinderkoordinaten zurückzuführen war. Für die räumliche Darstellung des Geschwindigkeitsfeldes verwendeten wir ein Fourier-Legendre Kollokationsverfahren, das spektrale Genauigkeit und die effiziente Berechnung der advektiven Nichtlinearität ermöglichte. Die Haft-Randbedingungen an der Rohrwand, sowie die Forderungen nach Inkompressibilität, Regularität und Analytizität des Geschwindigkeitsfeldes konnten über Lagrangeverfahren erster und zweiter Art berücksichtigt werden. Die Simulation turbulenter Dynamik entsprach dabei der zeitlichen Integration eines Anfangs- und Randwertproblems, die Suche nach kohärenten Lösungen basierte dagegen auf einem modifizierten Newton-Verfahren und einer Methode zur Erzeugung ausgezeichneter Anfangsbedingungen. Die Erläuterung der wichtigsten von uns ausgewählten Methoden und Algorithmen zur direkten numerischen Simulation der Rohrströmung erfolgt in Kapitel 4. Um die hier vorliegenden Ergebnisse zu erzielen wurden Gesamtrechenzeiten in der Größenordnung von CPU-Jahren auf verschiedenen Hochleistungsrechnern benötigt.

Bei der Entwicklung von Programmen dieser Komplexität ist eine umfangreiche Verifikation im Sinne von signifikanten Tests von größter Bedeutung. Als Meilensteine der Programmentwicklung und -verifikation wurden die Lösung der linearisierten Bewegungsgleichungen, die nichtlineare Zeitentwicklung 'optimaler' Strömungsmoden sowie die Simulation dreidimensionaler turbulenter Strömungen zugrunde gelegt. Aufgrund der umfangreichen Literatur über numerische Arbeiten zur Rohrströmung sind hochpräzise Daten vorhanden, denen wir unsere Rechnungen in Kapitel 5 gegenüberstellen. Dabei wird gleichzeitig großer Wert darauf gelegt, die wichtigsten auftretenden physikalischen Effekte und Mechanismen herauszuarbeiten.

1.3 Exakte kohärente Strukturen in der Rohrströmung

Eine Familie von nichtlinearen dreidimensionalen Wellenlösungen der vollen Navier-Stokes Gleichungen konnte gefunden werden. In einem geeignet mitbewegten Koordinatensystem handelt es sich hierbei um stationäre Strömungen. Sie weisen diskrete axiale Rotationssymmetrien auf, wobei der Zustand mit dreizähliger Symmetrie die niedrigste kritische Reynoldszahl von 1250 hat. Ihre Struktur wird von Wirbeln mit Achse in Strömungsrichtung sowie schlauchartigen Bereichen relativ hoher bzw. niedriger Geschwindigkeit in Strömungsrichtung dominiert. Die Wellenlösungen erinnern damit einerseits an stationäre Strömungen in ebenen Scherströmungen [17, 51, 74], andererseits auch an experimentell beobachtete kohärente Strukturen in turbulenten Wandschichten [41]. Sie entstehen in Sattel-Knoten-Bifurkationen ohne jede Verbindung zum laminaren Profil. Bereits an der Bifurkation sind sie linear instabil, jedoch nur in einer bis vier Richtungen. Die beiden bifurkierenden Äste bilden dabei je ein zweidimensionales Kontinuum von Lösungen. Das Auffinden dieser Lösungen gelang mittels einer transversalen Volumenkraft, die aufgrund von Beobachtungen in anderen Scherströmungen richtig konstruiert werden konnte. Unseres Wissens handelt es sich hierbei um die ersten nichttrivialen exakten kohärenten Zustände, die in der Rohrströmung gefunden wurden. Die Vorstellung der neu gefunden Familie von dreidimensionalen Wellenlösungen und die Analyse ihrer Struktur und Stabilität erfolgt in Kapitel 6. Dort wird auch die Methode detailliert beschrieben, mit der ihr Auffinden erst möglich wurde. Diese kohärenten Zustände sind in vielerlei Hinsicht von fundamentalem Interesse. Sie zeigen auf, wie in der Rohrströmung eine dauerhafte nichttriviale Dynamik möglich ist, die dennoch um ein vielfaches einfacher strukturiert ist als eine turbulente Strömung, die sofort mit irregulärer Dynamik auf einer Vielzahl von Längen- und Zeitskalen verbunden ist. Somit sind sie grundlegend für das Verständnis komplexerer Strömungen sowie für die Bildung niedrigdimensionaler dynamischer Systeme, mit denen Eigenschaften der Rohrströmung modelliert werden können. Der Nachweis erster exakter kohärenter Zustände stützt die Theorie der Bildung eines chaotischen Repellors im Phasenraum. Im Rahmen der Theorie periodischer Orbits [25] wäre es als ein längerfristiges Ziel denkbar, turbulente dynamische Größen, wie z.B. Dimensionen des Repellors, Lyapunov-Exponenten oder Entweichraten, durch eine Entwicklung nach kohärenten Strukturen systematisch zu approximieren.

1.4 Simulation des Turbulenzübergangs in der Rohrströmung

Durch die dynamische Untersuchung turbulenter Rohrströmungen bei Reynoldszahlen zwischen 1600 und 2200 konnten neue Ergebnisse im Übergangsbereich zwischen rasch zerfallenden und langlebig turbulenten Strömungen erzielt werden, die in Kapitel 7 präsentiert werden. Dabei wurde die Amplitude der eingebrachten Störung sowie die Reynoldszahl systematisch variiert. Die Lebenszeit turbulenter Trajektorien zeigte eine starke Sensitivität auf kleinste Änderungen in den Anfangsbedingungen und in den Systemparametern. So konnten beispielsweise relative Änderungen in den Anfangsbedingungen im sub-promille Bereich zu einer Erhöhung der Lebensdauer um eine Größenordnung führen. Diese Sensitivität konnte durch die Berechnung des größten positiven Lyapunov-Exponenten entlang einer Vielzahl turbulenter Trajektorien quantifiziert werden. Dem Wert des Lyapunov-Exponenten von ca. 0.07 in Einheiten der mittleren Geschwindigkeit und des Rohrdurchmessers bei Reynoldszahlen um 2000 entspricht eine Halbierung der Vorhersagbarkeit der Strömung alle 10 Zeiteinheiten. Es zeigte sich, dass die Einzugsbereiche schnell zerfallender und langlebiger turbulenter Trajektorien durch eine sehr verwobene und komplexe Stabilitätsgrenze getrennt sind. Dies ist in Übereinstimmung mit den Laborexperimenten von Darbyshire & Mullin [19]. Bei der statistischen Untersuchung von Ensembles von transienten turbulenten Trajektorien wurde eine exponentielle Verteilung der turbulenten Lebensdauern identifiziert. Diese entspricht einer konstanten Entweichrate, die ein Hauptcharakteristikum eines Repellors darstellt.

All diese Ergebnisse stützen die Erklärung des Turbulenzübergang in der Rohrströmung im Rahmen der Theorie dynamischer Systeme: instabile exakte kohärente Zustände existieren im Phasenraum, deren Anzahl und Grad der Vernetzung durch heterokline und homokline Verbindungen mit der Reynoldszahl wächst. Diese Zustände bilden das Skelett eines chaotischen Repellors, der das Auftreten langlebiger turbulenter Strömungen erst ermöglicht.

Der Turbulenzübergang in der Rohrströmung erweist sich nun in zentralen Aspekten als eng verwandt mit der ebenen Couette Strömung [9, 17, 51, 73, 74], sowie dem Taylor-Couette System bei großen Radien [27, 33], wodurch der universelle Charakter eines Übergangsszenarios für linear stabile Scherströmungen untermauert wird.

2 Introduction

Hagen-Poiseuille flow through a pipe of circular cross-section belongs to the class of shear flows with a linearly stable profile for all Reynolds numbers. As in the case of plane Couette flow and Taylor-Couette flow with the inner cylinder at rest, the transition to turbulence is not related to series of symmetry-breaking linear instabilities. On the contrary, laboratory experiments show a strongly intermittent transition [19, 68, 95, 96]. The Reynolds number, based on pipe diameter and mean flow velocity, down to which turbulent dynamics can be observed strongly varies between 1800 and 2300. Whether transition is triggered or not depends very much on details of the experimental setup and on the type of the injected finite amplitude disturbance [19]. Further key features of pipe flow turbulence transition experiments will be presented in chapter 3.

Our aim is to shed some light on this transition process.

For the direct numerical simulation of pipe flow transition a new spectral code had to be developed to solve the full three-dimensional nonlinear Navier-Stokes equations accurately and efficiently. We use a Fourier-Legendre collocation method in cylindrical coordinates, with Lagrangian multipliers to account for no-slip boundary conditions at the wall and the constraint that the flow field is solenoidal, analytical and regular at the centerline. Details on the equations of motion and the various numerical methods involved in their solution will be provided in chapter 4. In chapter 5 the pipe code will be thoroughly tested by reproducing literature values for the linearized problem, for the nonlinear dynamics of optimal modes, and for the statistical properties of fully developed turbulent flow up to Reynolds numbers of 5000.

Based on extensive numerical calculations we give evidence for an explanation for the pipe flow transition scenario. According to this explanation turbulence transition in a pipe is dominated by linearly unstable nonlinear 3-d states that are not connected to the laminar profile and that form a chaotic saddle. This would then be similar to the situation in plane Couette flow [9, 17, 51, 73, 74] and certain parameter regimes of Taylor-Couette flow [27, 33].

As one indicator for this process we present a family of three-dimensional travelling waves for flow through a straight pipe of circular cross-section in chapter 6. These are the first nonlinear 3-d exact coherent states identified in pipe flow. They were found by a continuation of transversally forced travelling waves by a modified Newton-Raphson method which was implemented with a spatial resolution of up to 21 modes in azimuthal and downstream direction and 44 Legendre polynomials radially. This corresponds to about 8700 dynamically active velocity coefficients. They originate in saddle-node bifurcations at Reynolds numbers as low as 1250, which is well below transitional Reynolds numbers. All states are immediately linearly unstable at the bifurcation and they differ in their discrete axial rotation symmetry. Their dominating structures are streamwise streaks and streamwise vortices that closely resemble coherent states in other shear flows like the wavy-vortex flow in Taylor-Couette, plane Couette or plane Poiseuille flow [17, 33, 51, 94].

In chapter 7 we analyse extensive numerical simulations of turbulent trajectories at transitional Reynolds numbers. Numerically this corresponds to the solution of initial-boundary value problems which have been implemented with up to 33 Fourier-modes in azimuthal direction and 29 Fourier-modes in downstream direction, as well as 50 Legendre polynomials radially. This is a compromise between maximum resolution, maximum cut-off lifetime and largest statistics. We show the very sensitive dependence on initial conditions quantified by the largest Lyapunov exponent of turbulent trajectories, a complex stability border between long-living and quickly decaying transient states, and the exponential distribution of life times of the turbulent state. These findings strongly support the existence of a strange saddle (repellor) in phase space.

Our findings give evidence that the transition to turbulence in pipe flow is connected with the existence of unstable exact coherent states that provide a skeleton for the formation of a chaotic saddle that can explain the intermittent transition to turbulence and the sensitive dependence on initial conditions in this classic shear flow.

3 Laboratory transition experiments in pipe flow

Figure 3.1: The hall of fame: Gotthilf Hagen, Jean Poiseuille, Osborne Reynolds (from left to right)

In this chapter we want to give a short overview over key features of laboratory pipe flow transition experiments in order to provide a basis for the discussion of many of our numerical experiments and findings in chapter 6 and 7. Due to the tremendous amount of literature this list cannot claim to be exhaustive.

Three names are once and for all connected to pipe flow experiments: These are on the one hand Gotthilf Hagen (1797-1884), a German scientist from Königsberg, and Jean Poiseuille (1797-1869), a French scientist from Paris, both of which investigated in laminar pipe flow which now bears their names. On the other hand there is Osborne Reynolds (1842-1912), an Irish scientist from Belfast, whose famous experiments from 1883 [68] were the starting point for the study of transition from laminar to turbulent flow in a pipe. Reynolds found that the various parameter dependencies can be boiled down to a single dimensionless parameter, the Reynolds number $Re = UD/\nu$, where U is the mean flow velocity, D the pipe diameter, and ν the kinematic viscosity. He observed that

> ”…there were two critical values for the velocity in the tube, the one at which steady motion changed into eddies, the other at which eddies changed into steady motion.” [68]

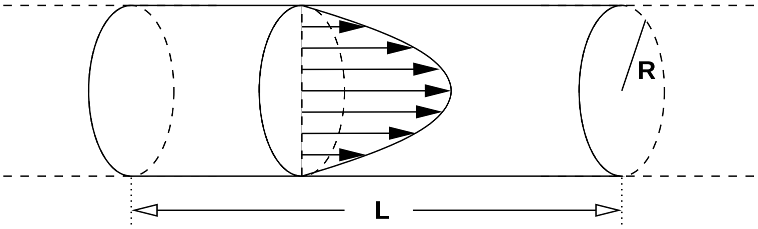

Figure 3.2: Sketch of a section of a straight pipe of uniform circular cross-section with the laminar Hagen-Poiseuille flow profile.

The latter corresponds to the Reynolds number of about 2000 above which turbulent flow can intermittently be maintained if transition has been induced. Literature values for this number scatter between 1800 and 2300 [19, 68, 95, 96]. The former corresponds to the Reynolds number at which 'natural' transition occurs. Natural transition is induced by unavoidable imperfections of the experimental setup and hence it strongly depends on experimental details. It can be delayed up to $Re > 10^5$ [60] since the laminar flow (sketched in Fig. 3.2) stays linearly stable to infinitesimal disturbances. The finite smoothness of the pipe inlet continously disturbs the flow and instabilities in the boundary layer might develop long before the laminar flow becomes fully developed [95]. At transitional Reynolds numbers this leads to an intermittent transition where series of turbulent spots and laminar regions alternate. (At high enough Reynolds numbers the pipe flow finally stays turbulent over its full length.) Between the turbulent patches there are patches of laminar flow where the level of turbulence is not only somewhat decreased but exactly zero and a disturbance from outside is required to initialize a new burst. The intermittent character of pipe turbulence is most intriguing and has already been described by Reynolds:

> "Another phenomenon very marked in smaller tubes was the intermittent character of the disturbance. The disturbance would suddenly come on through a certain length of the tube and pass away and then come again, giving the appearance of flashes, and these flashes would often commence successively at one point in the pipe. The appearance when the flashes succeeded each other rapidly was as shown…" [68]

…in Fig. 3.3, which is Reynolds' original sketch.

In order to observe the flow structure it is necessary to visualize the working fluid, which is usually chosen to be water. Flow visualization can be based on methods as simple as the injection of of a thin band of dyed fluid, as sketched in Fig. 3.3, or the seeding with anisotropic light-reflecting plates. Or it might be as fancy as high-speed stereoscopic particle image velocimetry [22] to obtain highly resolved data on all three velocity components on

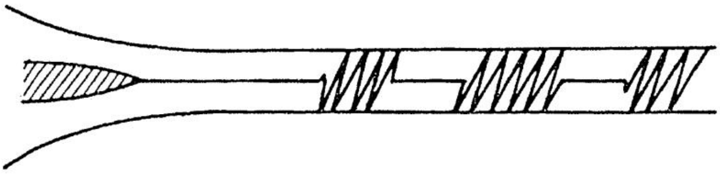

Figure 3.3: The intermittent character of transition in pipe flow as sketched by Reynolds.

two-dimensional cuts through the flow.

As we have a mean straight flow in the laboratory frame of reference and only finite pipe lengths the maximal observation time is limited. It must remain unanswered whether a turbulent patch that leaves the pipe stays sustained or is only a transient. This is in contrast to the closed Taylor-Couette flow and to plane Couette flow where an experimental device has been developed which allows for arbitrary observation times [9]. This technique has not been transfered to the pipe geometry yet.

The pipe length needed for a certain degree of development of the laminar profile has already been given in [16]. The estimate for the pipe length where the centerline velocity deviates by less than 1% from the Hagen-Poiseuille profile is

$$L_{99\%} = 0.112\, R\, Re\,. \tag{3.1}$$

By optimizing and smoothing the pipe inlet this distance can somewhat be reduced but the degree of development still changes with Reynolds number. This initial pipe section of course reduces the experimentally available test section of the pipe and therefore the maximum observation time.

In the early experiments the flow was driven by a constant pressure gradient between both ends of the pipe. Sometimes the spatial intermittency was sometimes tried to be explained by the drop in Reynolds number due to a turbulent patch which then leads to re-laminarization [89]. But this explanation failed as in experiments by Darbyshire & Mullin [19], which we present below, the volume flux is held constant and similar intermittency is observed.

It is not possible to force a turbulent pipe flow with a constant pressure drop as well as with a constant volume flux. The energy balance derived from the equations of motions (which will be presented later in chapter 4) reads

$$\partial_t E = -\nu \frac{1}{V} \int ||\nabla u||^2 dV + \frac{\Delta p}{L} U\,, \tag{3.2}$$

i.e. the rate of change in kinetic energy density is due to dissipation and forcing. Since the

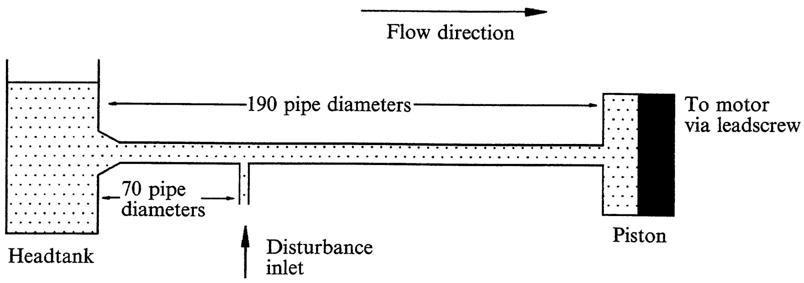

Figure 3.4: Sketch of the experimental setup for transition experiments by Darbyshire & Mullin [19]. The fluid (water) is pulled out of the tank and through the pipe by a piston which is motor driven via a lead screw. Some distance downstream of the pipe inlet a disturbance can be injected. 100 pipe diameters further downstream it is observed whether turbulence transition has occurred or not.

first two terms are strongly fluctuating functions of time and are not exactly correlated the rightmost term cannot be held constant for a turbulent flow.

Different realisations of constant-flux experiments exist. In the experiments by Draad *et al.* [23] a magnetic inductive flow-meter monitors the instantaneous flow rate and any deviations from the target flux are used to control the pump. This keeps the flow rate constant to within variations of 0.5% and allows for a continuous operation. An alternative realisation has been used by Darbyshire & Mullin [19], which is sketched in Fig. 3.4. There the fluid is pulled through the pipe by a cylindrical piston which is led by a leadscrew. The speed of the driving motor is held constant to within 0.5%. In both experiments the control of the flux and of the temperature results in an accuracy in the experimental Reynolds number of ± 15 at transitional Reynolds numbers of about 2000.

The alternative to natural transition is to induce a finite amplitude controlled localized disturbance. This has been done, for instance, in the experiments by Darbyshire & Mullin [19], which are particularly relevant to the present analysis. Some of their results are shown in Fig. 3.5. They inject an initial disturbance by jets or suction devices and record whether or not transition occurs some distance downstream. This is repeated for many combinations of initial amplitude and Reynolds number.

Fig. 3.5 shows that a sufficiently high disturbance amplitude and $Re > 1800$ are necessary for transition. The minimum necessary disturbance amplitude decreases with Re. They clearly find a strong sensitivity to perturbations and a broad intermittent range of decaying and turbulent perturbations in an amplitude vs. Reynolds number plane. These results do not change qualitatively for different types of initial disturbances. Darbyshire & Mullin interpret their findings as evidence for the existence of disconnected solutions.

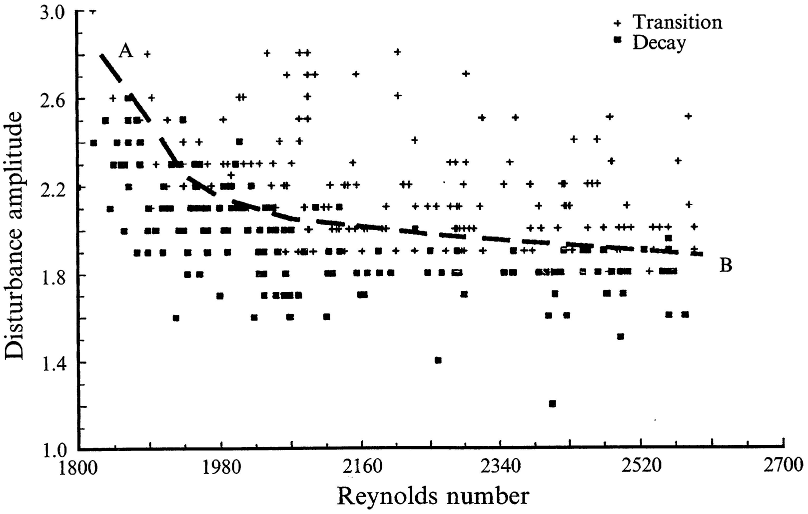

Figure 3.5: Laboratory transition experiments by Darbyshire & Mullin [19]. 100 pipe diameter downstream of the disturbance inlet the decision is made whether a turbulent patch can be observed (+), which then corresponds to transition, or whether the disturbance has decayed (■). The experiment is repeated with different disturbance amplitudes and Reynolds numbers. The dashed line from A to B is a guide for the eye but it not possible to divide the transition region from the decay region by such a smooth line. The experimental setup is sketched in Fig. 3.4.

Puffs and slugs

Turbulent spots in pipe flow evolve within very reproducible enveloping large scale structures which have been termed (turbulent) ’puff’ and ’slug’ by Wygnanski & Champagne [95]. They are sketched in Fig. 3.6 where the turbulent fluctuations have been neglected. The puff has a well-defined upstream interface which is sharp in the center of the pipe. Disordered motion of large-scale structures forms an intermediate downstream interface which is pre-

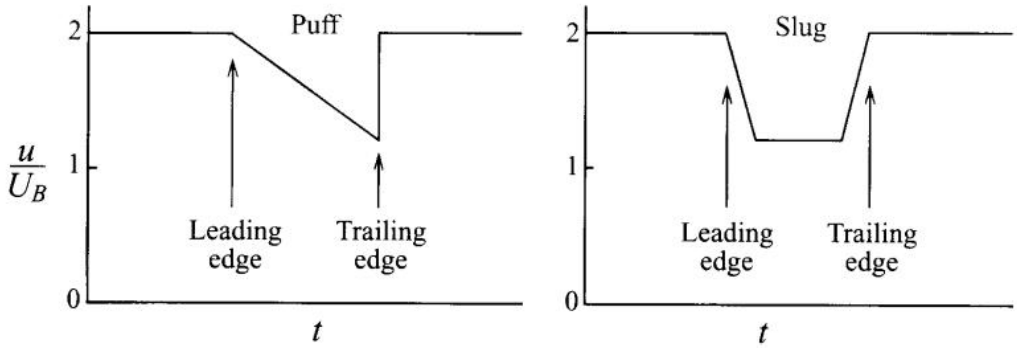

Figure 3.6: Time evolution of the streamwise centerline velocity at a fixed observation point as a turbulent puff or slug passes by [76].

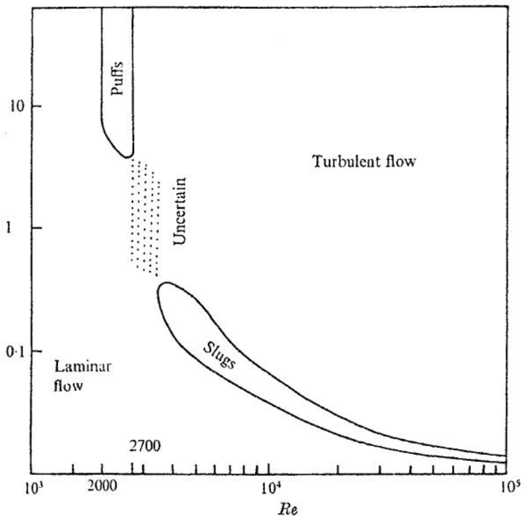

Figure 3.7: The parameter regions in which puffs and slugs occur (from [95] after Coles [18]); initial disturbance level at the pipe inlet vs. Reynolds number.

ceded by undisturbed laminar fluid. The slug shows well-defined interfaces at both ends and extends over almost the whole pipe cross-section. Streamwise vortices and streaks can be observed at the laminar-turbulent interfaces [30]. The parameter regions where puffs and slugs appear are displayed in Fig. 3.7. Puffs can only be seen for $2000 \lesssim Re \lesssim 2700$ whereas slugs occur for $Re \gtrsim 3200$.

The velocities of the laminar-turbulent interfaces of slugs and puffs as a function of Reynolds number is shown in Fig. 3.8. At $2100 < Re < 2400$ the fronts travel at about the mean flow velocity and 'equilibrium puffs' which neither grow nor shrink nor split are found [96]. For larger Reynolds numbers the turbulent region increases in size as the slug is advected along the pipe. The leading downstream front velocity of a slug first increases with the Reynolds number, becomes maximal at about $Re = 10^4$, and finally decreases to values slightly above the mean velocity. The trailing upstream front velocity decreases monotonously but stays positive for the Reynolds number range shown in Fig. 3.8. That is, disturbances are always swept away out of the test section and therefore only convective instabilities are induced by finite amplitude disturbances.

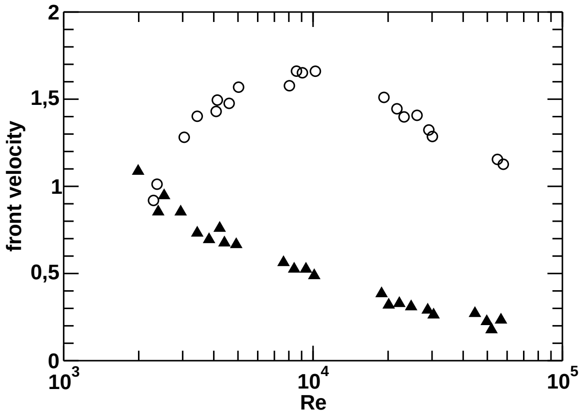

Figure 3.8: Propagation speed of the leading (open symbols) and trailing (filled symbols) interface for puffs and slugs as a function of Reynolds number. Velocities are given in units of the mean flow velocity. The data were obtained in three different pipes and is taken from [95].

4 A new spectral code for pipe flow

Why a *new* pipe code? A variety of codes using different algorithms have successfully been applied to simulate nonlinear pipe flow, for instance, [28, 46, 57, 66, 76, 90]. But none of these codes seems to meet our claim to combine highest spectral spatial precision with the lowest number of degrees of freedom. The method of Lagrange multipliers for the treatment of various different linear constraints on the flow enables us to use the Lagrange II mechanism, i.e. to work in the subspace of velocity fields that obey all constraints on the velocity field:

- $\nabla \cdot u \equiv 0$ (incompressibility)
- $u(r = R) \equiv 0$ (no-slip)
- regularity (no singularities at pipe center-line)
- analyticity (spectral precision).

This minimizes the remaining number of active degrees of freedom which is essential for the search algorithm for exact coherent states since the computation time scales with the third power of the total number of degrees of freedom [32, 74]. The development of most accurate and efficient numerical schemes for polar coordinates is still an active field of research. For a comparison of different spectral and finite difference methods for polar coordinates see [50] and references therein.

In the following the equations of motion are formulated and key algorithms that have been employed for their solution are presented.

4.1 Equations of motion

The pipe flow system consists of a smooth, non-rotating, straight pipe of uniform circular cross section, as sketched in Fig. 3.2. The pipe is filled with a Newtonian fluid of kinematic viscosity ν which is driven through the pipe by a uniform axial pressure gradient. The fluid is supposed to be incompressible so that the mass density ρ is constant. In streamwise direction periodicity is assumed with a wavelength L. We measure lengths in units of the pipe radius R and velocities in units of half the mean streamwise flow velocity, $U/2$, where

$$U = \frac{1}{V} \int_V u_z \, dV \, , \tag{4.1}$$

and where the integral goes over one fundamental periodic volume. This corresponds to measuring velocities in units of the center-line velocity of a laminar Hagen-Poiseuille flow of the same mean flow velocity U. The unit of time is D/U with pipe diameter D. This leaves us with two dimensionless parameters, the Reynolds number, based on mean flow and pipe diameter,

$$Re = \frac{UD}{\nu}\,, \tag{4.2}$$

and the streamwise length L of the periodic domain. The Reynolds number can be interpreted as the ratio of inertial forces ($(u \cdot \nabla)\, u \simeq U^2/D$) to viscous forces ($\nu \Delta u \simeq \nu U/D^2$) or as the ratio of the viscous diffusion time scale D^2/ν to the inertial time scale D/U.

The governing equations of motion are the Navier-Stokes equations and the continuity equation for an incompressible fluid:

$$\begin{aligned} \frac{\partial \mathbf{u}}{\partial t} + (\mathbf{u} \cdot \nabla)\mathbf{u} &= \nu \Delta \mathbf{u} - \nabla p \\ \nabla \cdot \mathbf{u} &= 0\,. \end{aligned} \tag{4.3}$$

The impermeable and no-slip boundary condition imply that the fluid is at rest at the wall.

The appropriate coordinate system are cylindrical coordinates $\mathbf{r} = (r, \phi, z)$[1]. This allows for the most accurate and simple handling of the boundary conditions, the price to be paid is the treatment of a coordinate singularity at the center-line and the various problems which arise from it - but that can be overcome (see below).

The fluid state at a time instant is completely described by the velocity field $\mathbf{u}(\mathbf{r}) = (u_r, u_\phi, u_z)(r, \phi, z)$ and the pressure field $p(r, \phi, z)$. The equations of motion (4.3) together with boundary and initial conditions now explicitly read:

$$\begin{aligned} \partial_t u_r + (\mathbf{u} \cdot \nabla)\, u_r - \frac{1}{r} u_\phi^2 &= -\partial_r p + \nu \left(\Delta u_r - \frac{2}{r^2} \partial_\phi u_\phi - \frac{1}{r^2} u_r \right) \\ \partial_t u_\phi + (\mathbf{u} \cdot \nabla)\, u_\phi + \frac{1}{r} u_r u_\phi &= -\frac{1}{r} \partial_\phi p + \nu \left(\Delta u_\phi + \frac{2}{r^2} \partial_\phi u_r - \frac{1}{r^2} u_\phi \right) \\ \partial_t u_z + (\mathbf{u} \cdot \nabla)\, u_z &= -\partial_z p + \nu \Delta u_z \\ \left(\partial_r + \frac{1}{r} \right) u_r + \frac{1}{r} \partial_\phi u_\phi + \partial_z u_z &= 0 \\ \mathbf{u}(r = 1) &= \mathbf{0} \\ \mathbf{u}(t = 0) &= \mathbf{u}_0\,, \end{aligned} \tag{4.4}$$

---

[1] For problems that might result from a treatment with finite differences in Cartesian coordinates see [42].

where

$$(\mathbf{u}\cdot\nabla) = u_r\partial_r + \frac{1}{r}u_\phi\partial_\phi + u_z\partial_z,$$
$$\Delta = \partial_{rr} + \frac{1}{r}\partial_r + \frac{1}{r^2}\partial_{\phi\phi} + \partial_{zz}.$$

For the optimal treatment of the coordinate singularity at the pipe center-line this set of equations must be completed by regularity and analyticity constraints.

4.2 Regularity constraints

Due to the periodic boundary conditions in azimuthal and streamwise direction the velocity field is expanded in terms of Fourier modes in those directions, $\mathbf{u}(r,\phi,z) = \sum_{n,m}\exp(in\phi + imk_z z)\mathbf{u}_{n,m}(r)$, with $k_z = 2\pi/L$ and $n, m \in \mathbb{Z}$. The complete spectral method and the treatment of the radial coordinate will be discussed in detail in section 4.4 below. For a solenoidal velocity field the solution to the linearized equations of motion are bounded along the center-line of the pipe ($r = 0$) if and only if certain regularity conditions are fulfilled [48]. They are given in a way which closely resembles a scalar product being equal to zero, $\langle F_j|u\rangle = 0$, with linear 'forces' F_j, which enables a formalism further discussed in section 4.5.

for $n = 0$:

$$u^r_{0,m}\Big|_{r=0} = 0 \tag{4.5}$$
$$u^\phi_{0,m}\Big|_{r=0} = 0 \tag{4.6}$$
$$\frac{\mathrm{d}u^z_{0,m}}{\mathrm{d}r}\Big|_{r=0} = 0 \tag{4.7}$$
$$u^z_{0,m}\Big|_{r=0} + \frac{2}{imk_z}\,\frac{\mathrm{d}u^r_{0,m}}{\mathrm{d}r}\Big|_{r=0} = 0 \tag{4.8}$$

$n = \pm 1$:

$$u^z_{\pm1,m}\Big|_{r=0} = 0 \tag{4.9}$$
$$\frac{\mathrm{d}u^r_{\pm1,m}}{\mathrm{d}r}\Big|_{r=0} = 0 \tag{4.10}$$
$$\frac{\mathrm{d}u^\phi_{\pm1,m}}{\mathrm{d}r}\Big|_{r=0} = 0 \tag{4.11}$$
$$u^r_{\pm1,m}\Big|_{r=0} \pm i\, u^\phi_{\pm1,m}\Big|_{r=0} = 0 \tag{4.12}$$

$n = \pm 2$:

$$\left. u^{r,\phi,z}_{\pm 2,m} \right|_{r=0} = 0 \tag{4.13}$$

$$\left. \frac{\mathrm{d}u^{z}_{\pm 2,m}}{\mathrm{d}r} \right|_{r=0} = 0 \tag{4.14}$$

$$\left. \frac{\mathrm{d}u^{r}_{\pm 2,m}}{\mathrm{d}r} \right|_{r=0} \pm i \left. \frac{\mathrm{d}u^{\phi}_{\pm 2,m}}{\mathrm{d}r} \right|_{r=0} = 0 \tag{4.15}$$

and for $|n| > 2$:

$$\left. u^{r,\phi,z}_{n,m} \right|_{r=0} = 0 \tag{4.16}$$

$$\left. \frac{\mathrm{d}u^{r,\phi,z}_{n,m}}{\mathrm{d}r} \right|_{r=0} = 0\,. \tag{4.17}$$

4.3 Analyticity constraints

In order to obtain spectral accuracy we need the numerically represented velocity field to be analytical. This gives us extra restrictions for the expansion of the velocity field.

Theorem 4.1 (Priymak & Miyazaki [64])
Consider an analytic vector field $\mathbf{u}(r,\phi) = e^{in\phi}[u_r(r)\mathbf{e}_r + u_\phi(r)\mathbf{e}_\phi + u_z(r)\mathbf{e}_z]$, $n \in \mathbb{Z}$, *for* $r \leq \epsilon$ *for some* $\epsilon > 0$. *The radial, azimuthal and axial components must then satisfy the following conditions:*

$$\begin{array}{lll} u_r = r f_E(r), & u_\phi = r g_E(r) & (n = 0) \\ u_r = r^{|n|-1} f_E(r), & u_\phi = r^{|n|-1} g_E(r) & (n \neq 0) \\ u_z = r^{|n|} h_E(r) & & (\forall n \in \mathbb{Z}) \end{array} \tag{4.18}$$

where f_E, g_E, *and* h_E *are analytic and even functions.*

Similar to the regularity constraints above the analyticity constraints are written as a scalar product being equal to zero, $\langle F_j | u \rangle = 0$:

For $n = 0$:

$$\left. \frac{\mathrm{d}^k u^{r}_{0,m}}{\mathrm{d}r^k} \right|_{r=0} = 0, \qquad k = 0, 2, 4, \ldots \tag{4.19}$$

$$\left. \frac{\mathrm{d}^k u^{\phi}_{0,m}}{\mathrm{d}r^k} \right|_{r=0} = 0, \qquad k = 0, 2, 4, \ldots \tag{4.20}$$

$$\left. \frac{\mathrm{d}^k u^{z}_{0,m}}{\mathrm{d}r^k} \right|_{r=0} = 0, \qquad k = 1, 3, 5, \ldots \tag{4.21}$$

and for $n \neq 0$:

$$\left.\frac{\mathrm{d}^k u^r_{n,m}}{\mathrm{d}r^k}\right|_{r=0} = 0, \qquad k = 0, 1, 2, \ldots, |n| - 2, |n|, |n| + 2, \ldots \tag{4.22}$$

$$\left.\frac{\mathrm{d}^k u^\phi_{n,m}}{\mathrm{d}r^k}\right|_{r=0} = 0, \qquad k = 0, 1, 2, \ldots, |n| - 2, |n|, |n| + 2, \ldots \tag{4.23}$$

$$\left.\frac{\mathrm{d}^k u^z_{n,m}}{\mathrm{d}r^k}\right|_{r=0} = 0, \qquad k = 0, 1, 2, \ldots, |n| - 1, |n| + 1, |n| + 3, \ldots \tag{4.24}$$

Note that the regularity equations (4.5–4.7) are contained in the analyticity conditions (4.19–4.21). The regularity equations (4.9–4.11, 4.13, 4.14, 4.16, 4.17) are contained in the analyticity conditions (4.22–4.24).

It is convenient to divide the total velocity field into the laminar profile $\mathbf{u}^{(0)}$ and a not necessarily small disturbance. The laminar flow, which is known as Hagen-Poiseuille flow, is purely axial and only a function of the radial coordinate: $u_z^{(0)}(r) = U_{CL}(1 - r^2)$ where U_{CL} is the laminar axial center-line velocity.

4.4 Fourier-Legendre collocation

For the spatial discretization we use a spectral method due to its high spatial accuracy with a low number of degrees of freedom. Due to periodic boundary conditions Fourier modes are appropriate for the expansion of the velocity field as a function of the azimuthal and axial coordinates, as has already been addressed in section 4.2. For the radial coordinate with no-slip boundary condition at the wall normalized Legendre polynomials have been used[2], which belong to the class of Jacobian polynomials that are particularly suitable as their convergence properties depend only on the smoothness of the function being expanded and not on a definite boundary condition: expanding a smooth (C^∞) function the remainder after N terms of the expansion goes to zero more rapidly than any finite power of $1/N$ as $N \to \infty$ [37]. This is the important advantage over finite differences or other methods.

We use a Legendre collocation over the pipe diameter where the collocation points are distributed according to the Gauss-Lobatto quadrature.

In a collocation method the approximating function is defined by its values at certain distinct points of the computational domain. It has been chosen as spectral method because of its efficiency in calculating the quadratic nonlinearities in the Navier-Stokes equation. The results of the collocation method do not only depend on the polynomials that are used but also

---

[2] The Legendre polynomials are normalized with respect to the scalar product induced by the Legendre Gauss-Lobatto quadrature, see below.

on the collocation points. The best choice for a set of collocation points corresponds to the quadrature formula of maximum precision:

$$\int_I f(x)dx = \sum_{j=0}^{J} f(x_j)w_j \tag{4.25}$$

where the w_j and the x_j are the positive weights and the abscissae of the quadrature, respectively. The use of a Gauss-Lobatto quadrature in which the first and last quadrature abscissae are chosen to be the end points of the integration interval I simplifies the treatment of no-slip boundary conditions. The other $(J-1)$ abscissae and the $(J+1)$ weights are defined by the demand that Eqn. (4.25) is exact for any Legendre polynomial up to degree (2J-1). Stable methods to calculate these weights and abscissae exist [63].

The density of collocation points near the wall increases quadratically with the number of collocation points whereas it only goes linearly near the center. This leads to a high spatial resolution where it is needed: close to the wall where velocity gradients are expected to be largest. The fact that Legendre polynomials P_n have a definite parity, $P_n(r) = P_n(-r)(-1)^n$, considerably simplifies the implementation of the analyticity constraints. We only use even numbers of collocation points so that no point is directly at the coordinate singularity.

When calculating quadratic nonlinearities with collocation methods the implicit multiplication of polynomials might result in polynomials of an order which is too high to be properly accounted for in the expansion. In practice this can slightly corrupt amplitudes of low order polynomials [14], but during our calculations errors or instabilities due to this aliasing have not been encountered. Thus, we have not made use of explicit de-aliasing methods.

Spatial derivatives

The velocity field expanded in Fourier modes and normalized Legendre polynomials taken at a collocation point $r = r_j$ reads:

$$\begin{pmatrix} u_r \\ u_\phi \\ u_z \end{pmatrix} (r_j, \phi, z; t) = \sum_{n,m} e^{i(n\phi + mk_z z)} \begin{pmatrix} \tilde{u}_r \\ \tilde{u}_\phi \\ \tilde{u}_z \end{pmatrix}_{n,m,j} (t), \quad j = 0, .., J \tag{4.26}$$

where the expansion coefficients are complex in general. By inserting this expansion into the equations of motion (4.4) the partial differential equations are transformed into an infinite set of coupled ordinary differential equations which has to be truncated for numerical purposes.

Partial derivatives with respect to ϕ and z are trivial due to the Fourier expansion in these directions, partial differentiation with respect to the radial coordinate is accomplished by a matrix multiplication in collocation space using the derivative matrix D_{jk} for which an explicit analytical representation exists in terms of the values of the highest order Legendre polynomial at the collocation points [79].

4.5 Lagrange method of the first kind

The problem of most discretisations of the incompressible Navier-Stokes equation (4.3) is the treatment of the pressure to which no boundary conditions exist [14][3]. The pressure adjusts itself instantaneously to changes in the velocity according to the continuity condition $\nabla\cdot\mathbf{u}$=0. An elegant method to solve this problem is the method of Lagrange multipliers [32, 74].

Instead of a direct solution of the coupled equations (4.4), the gradient of the pressure is treated as a boundary force which ensures the freedom of divergence. First $\partial\mathbf{u}/\partial t$ is calculated from Eqns. (4.4) neglecting the contribution from the pressure gradient and then the result is projected on the subspace of velocity fields that obey the linear constraints: The no-slip boundary conditions and the continuity equation together with the regularity and analyticity conditions build up constraints which can be written as inner products

$$\sum_l F_{kl}u_l \equiv F_k^\dagger u \equiv 0 \tag{4.27}$$

for all constraints $k = 1, .., K$, where the summation goes over all velocity coefficients u_l, $l = 1, .., L(> K)$. Here l is a multi-index and the dagger (†) represents the adjoint of a linear operator. Note, however, that the definition of adjointness depends on the definition of the inner products. Due to the cylindrical coordinates and the factor r in the integration measure the adjoint of a linear differential operator is not necessarily the transpose of the complex conjugate in the matrix representation. For instance, the operator for the divergence, ($\nabla\cdot$), reads ($\mathbf{e}_r(r^{-1}+\partial_r)+\mathbf{e}_\phi r^{-1}\partial_\phi+\mathbf{e}_z\partial_z$) whereas its adjoint operator is the transpose of the complex conjugate of the gradient operator, (∇), that reads ($\mathbf{e}_r\partial_r+\mathbf{e}_\phi r^{-1}\partial_\phi+\mathbf{e}_z\partial_z$).

The fact that the constraints decouple with respect to the Fourier modes reduces the numerical efforts considerably. To eliminate all components of the velocity field along the directions F_k a projector $\mathbb{P}$ on the subspace of velocity fields that obey all the constraints is constructed:

$$\mathbb{P}u = u - \sum_k F_k\lambda_k \equiv u - F\lambda, \tag{4.28}$$

where the complex Lagrange parameters are denoted λ_k. Premultiplying (4.28) by $F^\dagger$ gives

$$F^\dagger\mathbb{P}u = 0 = F^\dagger u - F^\dagger F\lambda \tag{4.29}$$

$$\Leftrightarrow \qquad \lambda = \left(F^\dagger F\right)^{-1} F^\dagger u \tag{4.30}$$

---

[3] The driving pressure drop along the pipe length is of course excluded from these considerations

and therefore

$$\mathbb{P} = \mathrm{Id} - F\left(F^{\dagger}F\right)^{-1}F^{\dagger}, \tag{4.31}$$

where Id is the identity. The various linearly dependent constraints have to be boiled down to a linear independent set of constraints to guarantee the invertibility of the Hermitian matrix $(F^{\dagger}F)$.

The above projections and thus the definition of the projector $\mathbb{P}$ are only correct if an orthonormal (with respect to the scalar product induced by the Legendre Gauss-Lobatto quadrature) basis is used to construct the constraints F [32]. Only then do the forces due to the constraints not change the energy content of the field. The collocation method transforms the orthonormalised Legendre basis into an orthogonal but non-orthonormal basis. Consequently, all the constraints have been formulated in spectral space, i.e. expanded in terms of *normalized* Legendre polynomials. The resulting Lagrange projector is then linearly transformed into collocation space by a one-to-one mapping. Now the action of the projector is equivalent to the action of the gradient of the pressure.

Time stepping
For the solution of the initial-boundary value problem (4.4) a standard solver for nonlinear ordinary differential equations has been chosen, an explicit fourth-fifth order Runge-Kutta-Fehlberg algorithm with adaptive step size control [82]. It includes an automatic error estimation and maximizes the step size while keeping the relative time stepping error below a certain threshold (typically 5×10^{-8}). Starting from arbitrary initial conditions the dynamical time evolution of the pipe flow field is simulated by the solution of the initial-boundary value problem (4.4).

Considerably higher numerical efforts are necessary for the search for exact coherent states in pipe flow, as they are expected to be linearly unstable and cannot be found by simple time integration. With the Lagrange method of the second kind the problem can be transformed into the search for a zero of nonlinear equations of motion of considerably reduced dimension. This will be explained in the next two sections.

4.6 Lagrange method of the second kind

Singular value decomposition (SVD) enables the explicit construction of orthonormal bases for the null-space and the range of any linear operator.

Using SVD on the Lagrange projector $\mathbb{P}$ on the subspace of velocity fields obeying the correct boundary conditions we construct a basis of the range of $\mathbb{P}$ and transform the whole problem into this new basis. In other words, we reduce the problem to the relevant subspace. This represents the transition to the Lagrange method of the second kind, which is equivalent to the Lagrange method of the first kind, but which has an important advantage: the number of variables one has to converge on in a Newton-Raphson cycle has decreased considerably and the Jacobian becomes regular.

For the treatment of coherent states that have a certain discrete spatial symmetry the span of the Lagrange projector $\mathbb{P}$ has to be divided into symmetric and antisymmetric basis vectors and the ones of the incorrect symmetry are neglected. This usually distinguishes between real and imaginary parts of certain velocity components and therefore it cannot be included by linear constraints in the above projection operator.

4.7 Search and continuation of travelling waves

On top of the code for the initial-boundary value problem we develop methods to find and continue travelling waves in pipe flow.

We first reduce the search for a travelling solution to a search for a fixed point. For this we get rid of the contribution from Navier-Stokes which merely acts as downstream translation of the velocity field: assume a travelling wave with downstream phase velocity v, $u(z,t) = u(z+vt,t_0)$. Then $\partial_t u(z,t) = v\partial_z u(z,t)$, that is, $v = \partial_z u \partial_t u / ||\partial_z u||^2$. This gives the reduced contribution from the Navier-Stokes equations, $\partial_t u' = \partial_t u - v\partial_z u$, which is equivalent to a transformation into the downstream comoving inertial frame of reference. Finding a travelling wave in pipe flow is now equivalent to finding a zero to the set of nonlinear equations $\partial_t u' = 0$. The method of choice for this task is a 'modified Powell hybrid method' [36] a combination of a Newton-Raphson method and a scaled conjugate gradient method, which has proven to be much more robust than other methods including hand-optimized Newton methods, and which still has a fast rate of convergence near a solution. The Jacobian is updated by the rank-1 method of Broyden [82] as long as this produces satisfactory progress.

The continuation of a travelling wave is accomplished by Keller's pseudo-arclength continuation method [21], which allows for a larger continuation step size as well as for the continuation of solution branches around folds, by the expense of enlarging the dimensionality of the problem by 1. This continuation method cannot, however, be applied to changes in the streamwise fundamental periodicity L, as then the projection operator $\mathbb{P}$ has to be rebuild and the following SVD randomly permutes the basis vectors of the span of $\mathbb{P}$. Changes in L are therefore numerically especially expensive.

To get a rough idea of the total size of this software project pipe code: the total number of lines of Fortran90 code without comment lines is about 5000 (and thus comparable to the number of LaTeX lines underlying this thesis). Additionally, various highly efficient routines for the solution of standard linear or nonlinear algebra problems have been employed (matrix inversion, eigenvalue decomposition, single value decomposition, Powell-hybrid method etc.).

5 Physics of pipe flow and verification of the new pipe code

Extensive tests on the validity and accuracy of the new numerical pipe program for the simulation of pipe flow have been carried out. In this chapter we will present a comparison with high-precision literature data for the linearized problem (section 5.1), for the non-normal and nonlinear dynamics of optimal modes (section 5.2), and for the statistical properties of fully developed turbulent flow up to Reynolds numbers of 5000 (section 5.3). Along the lines of these tests various interesting properties of pipe flow dynamics show up and will be discussed.

5.1 Linearized equations of motion

The first milestone and already one of the most important tests on the numerics is the accurate solution of the linearized problem. This is already the crucial verification, mode by mode, for many of our concepts which have been discussed in the previous chapter:

- spatial representation by Legendre polynomials including integration and differentiation,
- treatment of the boundary conditions,
- regularity and analyticity constraints,
- implementation of the linear Navier-Stokes equation,
- projection mechanism based on the method of Lagrange multipliers.

Two major difficulties emerged which had to be overcome: the problematic representation of r^{-1} and r^{-2} terms that appear in the differential operators in terms of Legendre polynomials had to be catered for, and the correct space and scalar product for the projection mechanism for the method of Lagrange multipliers had to be found. These problems could finally be overcome and the linearized equations could be solved with full *spectral* accuracy.

Let us write the eigenvalue problem as

$$L v_\lambda = e^{\lambda t} v_\lambda \tag{5.1}$$

eigenvalue		author
-0.02317	+ i 0.95048	Salwen *et al.*, 1980 [70]
-0.023170795764	+ i 0.950481396668	Leonard & Wray, 1982 [45]
-0.0231707957650042152055	+ i 0.9504813966699031794843	Priymak & Miyazaki, 1998 [64]
-0.023170795765	+ i 0.950481396670	present work

Table 5.1: Comparison with selected literature data on the least stable eigenvalue at $Re = 9600$. (n=1,m=1)-mode and $L/R = 2\pi$. Here our result is 'limited' to 12 leading decimal places due to double precision arithmetic. For a more detailed comparison with literature data see Appendix A.

with the linearized evolution operator L, the eigenfunctions $\{v_\lambda\}$ and the eigenvalues $\{\lambda\}$. As usual we measure lengths in units of the pipe radius and velocities in units of the laminar Hagen-Poiseuille centerline velocity, so that the eigenvalues λ are expressed as a multiple of U_{CL}/R.

We successfully compare our numerical eigenvalues with high precision literature data [72], [48], which have been obtained by independent numerical methods: in Appendix A we present tables of the least stable eigenvalues and visualizations of eigenfunctions of the linearized Navier-Stokes equations in detail.

Historically, research concentrated on a few test cases for the eigenvalue problem which we would also like to follow, such as a streamwise pipe length of $L/R = 2\pi$ and $Re = 9600$. Exemplarily we here give a first comparison with selected literature values for the least stable eigenvalue in Table 5.1.

We observe two factors limiting the accuracy: for the first leading eigenvalues the accuracy is mainly limited by the finite number of digits available in double precision arithmetic whereas for higher eigenvalues the finite spectral resolution dominates.

The main feature of the eigenvalue spectrum is the fact that all eigenmodes lie in the stable half of the complex plane, that is, the Hagen-Poiseuille profile is linearly stable with respect to infinitesimal disturbances. Any improper handling especially of the coordinate singularity could lead to spurious linearly unstable eigenmodes which could corrupt the whole character of the transition process.

Fig. 5.1 exemplarily shows the well known 'swear hand' distribution of the least stable eigenvalues $\{\lambda\}$ of the $(1, 1)$-mode together with four selected eigenvectors[1]. The notation (n,m)-

---

[1] As a single eigenvector of a complex conjugate pair does not correspond to a velocity field we here visualize the velocity field that corresponds to the real part of the eigenvector.

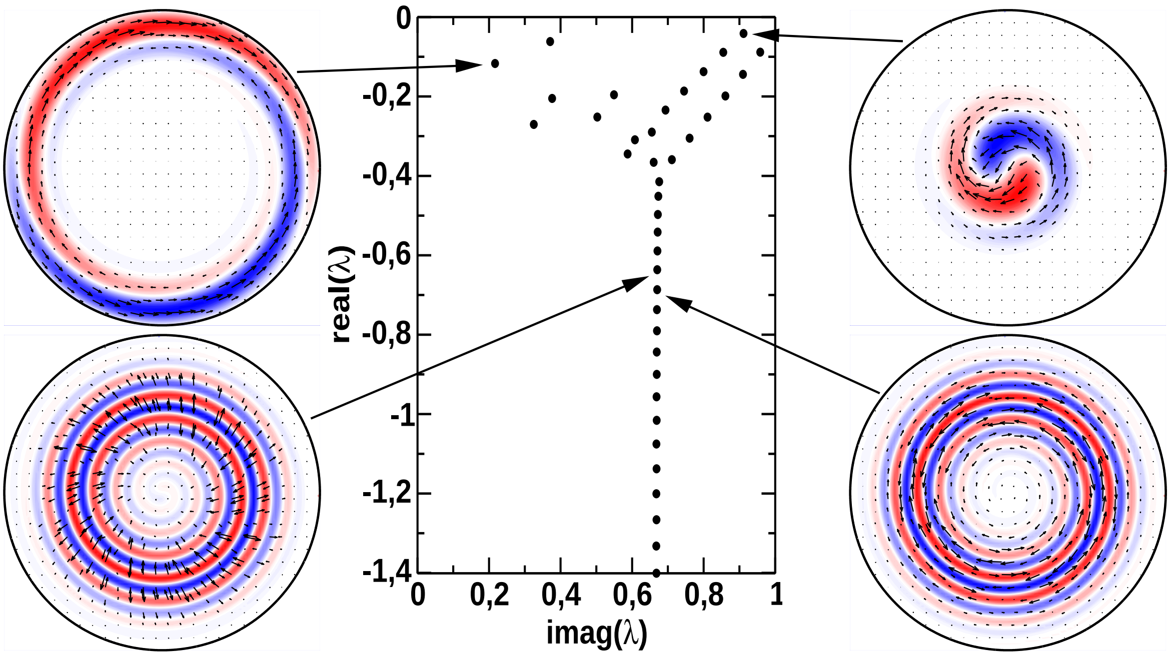

Figure 5.1: 'Swear hand' distribution of eigenvalues $\{\lambda\}$. $(1,1)$-mode at $Re = 3000$ and $k_z = 1$. The upper left branch of eigenvalues consists of 'wall modes', the two branches in the upper right are 'center modes', the straight lower branch consists of 'mean modes' (see text). The velocity fields corresponding to the real part of the eigenvectors number $1, 5, 27$, and 28 are shown (counterclockwise, beginning with the upper right graph); for the eigenvalues see Tab. A.3) .

mode always corresponds to an azimuthal wavenumber n and a streamwise wavenumber m. The distribution is similar to plane shear flows like plane Couette and plane Poiseuille flow [24]. The eigenfunctions can be classified into 'wall modes', 'center modes' and 'mean modes'. Apart from obvious visual reasons (see Fig. 5.1, wall modes localized near the wall, center modes localized near the center-line), these classifications are defined by the asymptotic behaviour of the phase velocity $v = \text{imag}(\lambda)/k_z$ of the modes for large values of the product $(Re\, k_z)$ [72]:

$$\text{wall modes:} \quad v \to 0 \quad \text{as} \quad Re\, k_z \to \infty\,; \tag{5.2}$$

$$\text{center modes:} \quad v \to 1 \quad \text{as} \quad Re\, k_z \to \infty\,; \tag{5.3}$$

$$\text{mean modes:} \quad v \to 2/3 \quad \text{as} \quad Re\, k_z \to \infty\,. \tag{5.4}$$

That is, for instance, the phase velocity of center modes approaches the laminar pipe centerline velocity in this limit.

5.2 Two-dimensional nonlinear equations of motion

The second milestone of the development and verification of the pipe code is the time-integration of 'optimal' modes. This section is concerned with the evolution of streamwise invariant flows: three-component velocity fields in two (spatial) dimensions ('3c-2d'),

$$\mathbf{u}(\mathbf{r};t) = \begin{pmatrix} u_r \\ u_\phi \\ u_z \end{pmatrix} (r, \phi; t)\,. \tag{5.5}$$

This class of two-dimensional modulations of the basic flow is of special interest as the initial disturbances of largest linear transient energy amplification are those without streamwise modulation and with azimuthal wavenumber $n = 1$, as has been shown in [5]. Note that only the $n = 1$ mode perturbs the mean centerline velocity, in contrast to disturbances with higher azimuthal wavenumber as well as axisymmetric modes. The precise shape of the optimal disturbance has been identified in [72]: it is a pair of streamwise vortices with 40% of the energy in the radial component and 60% in the azimuthal component. Zikanov [97] chose a simple but very close approximation to this optimal disturbance and studied its linear transient dynamics, its nonlinear behaviour and the stability of the transient dynamics.

We want to reproduce some of Zikanov's results on initial-boundary value problems in order to check the implementation of

- the dynamical time integration method,
- the (two-dimensional) advective nonlinearity in the Navier-Stokes equations,
- the volume forcing in terms of an axial uniform pressure gradient,
- various service routines.

All aspects tested in Section 5.1 will here undergo a further and complementary test.

As the initial condition for the disturbance of the laminar profile we take Zikanov's nearly optimal ($n = \pm 1, m = 0$)-mode,

$$\mathbf{u}(\mathbf{r}) = c \begin{pmatrix} 1 - 3r^2 + 2r^3 \\ i(1 - 9r^2 + 8r^3) \\ 0 \end{pmatrix} e^{i\phi} + cc\,, \tag{5.6}$$

which is divergence free and satisfies no-slip boundary conditions at the wall [2]. This vortex pair is visualized in Fig. 6.2, page 46. We scale the initial amplitude c so that the energy

---

[2] Note that this approximation to the optimal initial condition is no longer analytic in a neighbourhood of the pipe centerline as it violates Theorem 4.1 from page 20. In our numerics only (arbitrary close) analytical approximations are employed.

of the initial disturbance takes a certain value ($E(t{=}0)/E_{lam}$ = 0.01, 0.005, 0.0025, 0.001, or 0.0001 in units of the energy of the laminar profile). Additionally we consider the case of linearized equations which corresponds to the limit $E(t{=}0) \to 0$. The non-normal and nonlinear evolution of a two-dimensional disturbance which is close to the optimal initial condition that leads to maximal non-normal amplification is shown in Fig. 5.2.

Our results nicely agree with Zikanov's [97] original data which are shown in Fig. 5.3. The differences are within plotting accuracy, which is even more surprising considering the completely different numerical schemes that have been employed[3]. Our calculations have been carried out with 40 Legendre polynomials radially and 21 Fourier modes azimuthally. Control runs with 40 polynomials and 51 modes as well as with 60 polynomials and 21 modes show that our results have converged to within plotting accuracy. The results have similarly converged with respect to the time stepping. The linear evolution leads to a maximum energy amplification of 648.5 at time $T = 146.8$, which is very close to the result by Schmid & Henningson [72], who found a maximum energy amplification of 649 at time 147 for the optimum initial condition.

Non-normality

No exponential linear growth can be expected, as the laminar profile is linearly stable. Nevertheless, there is a strong transient algebraic linear growth. Both the amplitude and the time instant of the maximal transient amplification of the velocity field grow linearly with Reynolds number. Non-normality of the linear evolution operator L is mathematically reflected by the fact that it does not commute with its adjoint operator, $[L, L^\dagger] \neq 0$, and that its eigenfunctions are not mutually orthogonal. This can be understood in the following way: the laminar profile advects disturbances downstream, i.e. the eigenmodes are mostly oriented (anti-)parallel to the laminar flow. This makes the eigenmodes collapse into the main streamwise direction. Therefore a misfit disturbance has large coefficients when expressed in terms of the eigenmodes. It grows algebraically, turns into the main direction of the eigenmodes and decays exponentially.

The nonlinear evolution in time changes the mean flow in such a way that non-normality is effectively reduced. For the nonlinear calculations an increase in initial energy hence reduces the maximal energy amplification and shifts it to earlier times. The trajectories increase their initial oscillations in energy until they start to decay monotonously.

All trajectories with Zikanov's initial conditions decay asymptotically to the laminar profile as in fact do all streamwise independent (3c-2d) velocity fields [97]. It follows that for a self-sustaining dynamics streamwise dependent structures are needed to feed back on the initial

---

[3] In a recent publication [49] a 'very good' agreement with Zikanov's computations has already been claimed even though the work showed obvious quantitative differences.

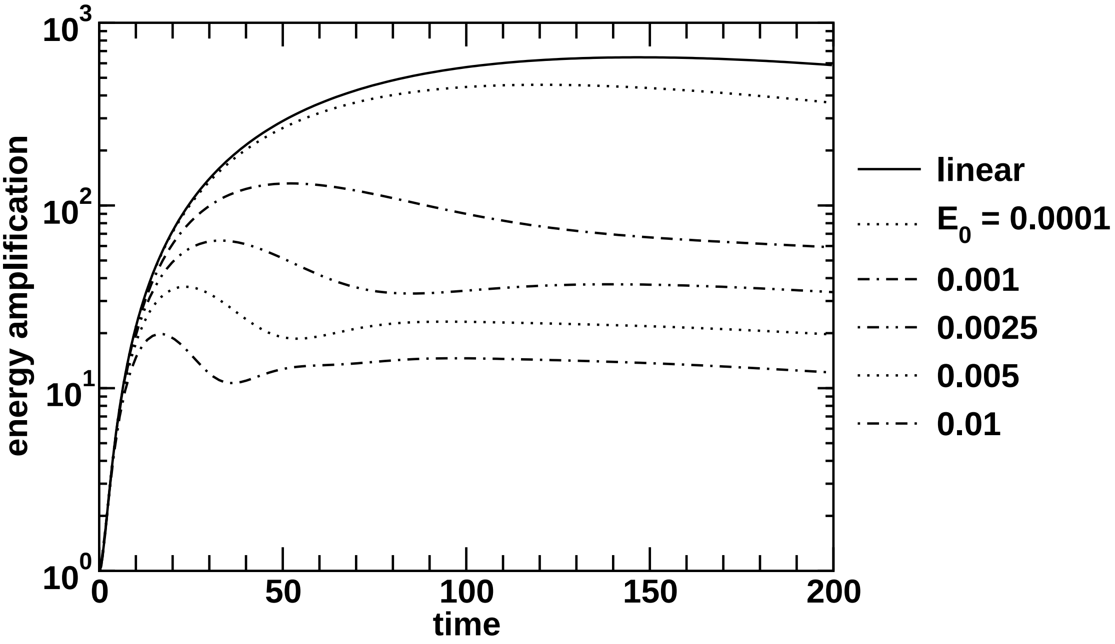

Figure 5.2: Non-normal linear and nonlinear evolution of a nearly optimal two-dimensional disturbance. Relative energy amplification $E(t)/E(0)$ vs. time at $Re = 3000$. The linear evolution leads to a maximum energy amplification of 648.5 at time $T = 146.8$, the time unit is, as always, D/U.

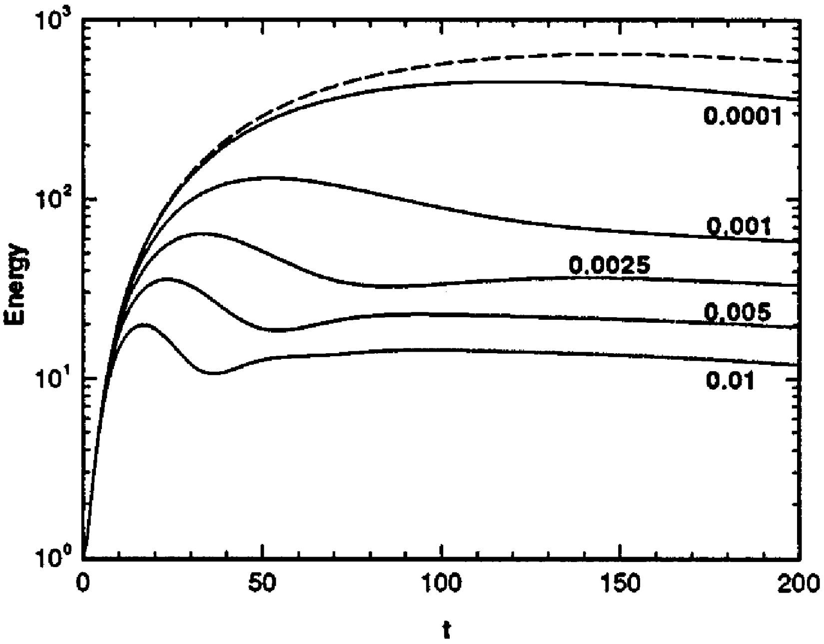

Figure 5.3: Zikanov's original data (Fig. 1 from [97]). As in Fig. 5.2: relative energy amplification $E(t)/E(0)$ vs. time at $Re = 3000$.

streamwise rolls by nonlinear self-interaction, cf. [92]. Therefore all of the presumed exact coherent structures like travelling waves and unstable periodic orbits must be streamwise modulated.

The above transient dynamics shows a further interesting feature: the almost steady streaky flow develops inflection points in its profile which lead to inviscid instabilities with respect to three-dimensional disturbances. This opens the possibility for 3-d structures to grow, localized near the inflection points at first, but finally destabilizing the streaks and taking over to a turbulent dynamics. This *streak breakdown* mechanism is a possible route to turbulence in shear flows [97]. A visualisation of this process will be shown in Fig. 5.9 in section 5.3.

Note that all our calculations so far were performed at a constant forcing, i.e. with a fixed pressure drop along the length of the pipe. Later on (Chapter 7) we want to drive pipe flow at a constant volume flux. We use this well controlled 2-d situation to develop the necessary tools we need for constant mass flux forcing and discuss the dynamical changes in the next section.

5.2.1 Constant-flux pipe flow

Fig. 5.4 once again shows the nonlinear time evolution of the nearly optimal two-dimensional disturbance at Re=3000 and $E(t{=}0){=}0.01$ as in Fig. 5.2. But now we compare the constant-pressure-drop simulation (black lines) with the constant-volume-flux simulation (red lines), where the mean flux is kept at its laminar value. The latter is accomplished by an instantaneously adjusted linear pressure gradient in the explicit time marching scheme. This guarantees the absence of numerical instabilities or artificial temporal oscillations in the flux. The upper graph of Fig. 5.4 shows the energy traces. In the constant flux simulation the decay is faster. This is due to the changes in the eigenvalue spectrum for the (n=0, m=0)-mode where, for instance, the least stable eigenvalue has changed to zero (see table A.1 in Appendix A). The middle graph of Fig. 5.4 shows the total pressure drop normalized by the laminar Hagen-Poiseuille linear pressure gradient as a function of time. In the constant volume flux situation the pressure drop over the pipe length has to be increased considerably, at $t \approx 28$ the necessary total pressure gradient has almost doubled. The lower graph of Fig. 5.4 shows the temporal development of the total flux. At constant pressure drop the total flux goes down as the friction increases. At time 276 (not shown) the flux takes its minimum and then slowly increases back to its laminar value. For the constant-flux case the initial maximum pressure drop is delayed in comparison to the maximum in energy. This phase lag is due to the time it takes for smaller structures to develop by instabilities of the initial larger scale structures and thereby increase the friction. Energy dissipation will then take place much more efficiently at the smaller scales.

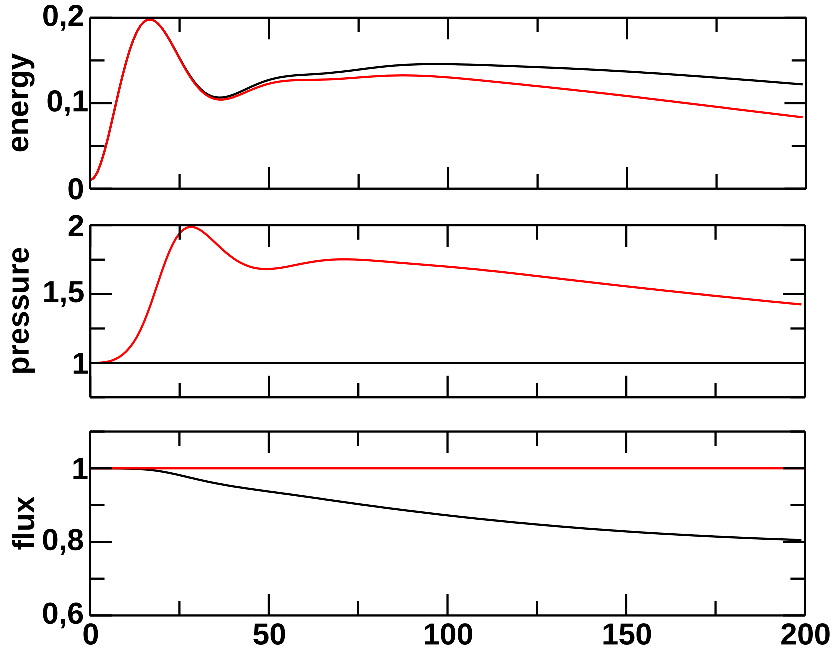

Figure 5.4: Constant-pressure-drop (black lines) vs. constant-flux pipe flow (red lines). Exemplary comparison of nonlinear 2-d calculations with Zikanov's initial condition with $E(t=0) = 0.01$ at $Re = 3000$. Upper graph: energy amplification factor; middle graph: total pressure drop in units of the laminar pressure drop; lower graph: total streamwise volume flux in units of the laminar flux.

5.3 Three-dimensional nonlinear equations of motion

Having precisely reproduced linear and 2-d nonlinear results in sections 5.1 and 5.2 we now go for the final test of our pipe code: solving initial-boundary-value problems for the full 3-d nonlinear Navier-Stokes equation i.e. simulating turbulent pipe flow. In order to compare our numerics with suitable experimental and numerical literature data we have to go up to a Reynolds number of 5000, which is considerably above the transitional Reynolds number range we are mostly interested in. By reproducing turbulent experimental and numerical data we want to test

- the implementation of the full 3-d nonlinear equation of motion,
- the accuracy with which the flow stays regular and analytic, especially for long turbulent time integrations.

5.3.1 Turbulent pipe flow at $Re = 5000$: a comparison with laboratory and DNS literature data

We start from random initial conditions of sufficiently high amplitude to trigger transition to a turbulent dynamics. After 200 initial time units that are needed for the relaxation on to the turbulent state a single long turbulent trajectory of more than 1000 time units is analysed. The spatial resolution for this calculation is $|n|/24 + |m|/20 \leq 1$, i.e. up to 49 Fourier-modes in azimuthal direction and 41 modes in axial direction. 60 Legendre polynomials have been used radially and the streamwise wavelength is $L/R = 10$.

The distribution of mean kinetic energy on the Fourier-modes is shown in a two dimensional energy spectrum in Fig. 5.5. It is normalized in such a way that the energy of the (0,0)-mode is 1. The (0,0)-mode including the mean profile is of course by far the dominant mode, followed by a handful of modes that contribute a considerable amount of energy, and then the energy content of the modes slowly goes down. No piling up of energy can be observed at the smallest scales, which would have occurred for a severely under-resolved calculation.

The various numbers that can be extracted from the mean turbulent profile are compared to numerical and experimental literature values in Tab. 5.2. Quantities based on the overall

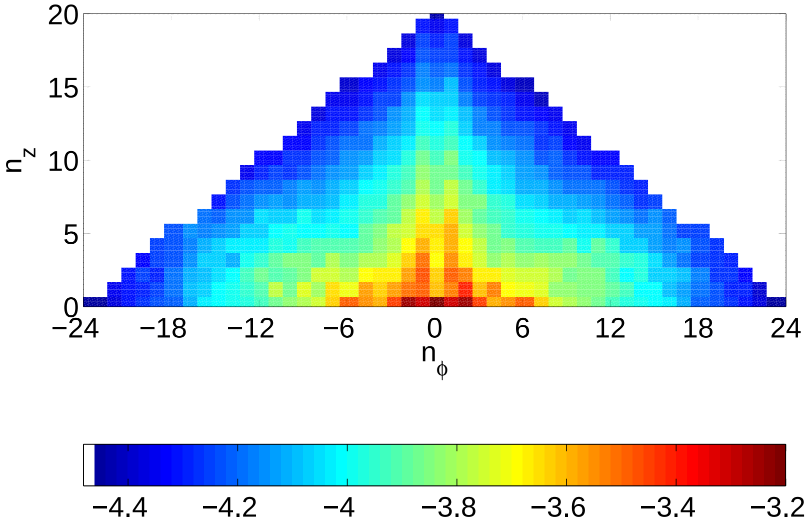

Figure 5.5: Two-dimensional energy spectrum at $Re = 5000$. The spatial resolution for the simulation is $|n|/24 + |m|/20 \leq 1$. 60 Legendre polynomials have been used radially. Only the upper half of the spectrum is shown as the (-n,-m)-mode is related to the (n,m)-mode by complex conjugation due to the reality of the velocity field.

	present work	Quadrio & Sibilla (DNS) [66]	Eggels *et al.* (DNS) [28]	Eggels *et al.* [28]	Reich & Beer [67]
Re	5000	4900	5300	5450	5000
δ^*	0.148	0.145	-	-	-
Θ	0.093	0.089	-	-	-
H	1.60	1.63	-	-	-
u_{CL}/U	1.31	1.31	1.31	1.30	1.27
U/u_τ	13.2	14.24	14.73	14.88	14.59
c_f	0.0115	0.00986	0.00922	0.00903	0.00939
Re_{CL}	6550	6419	6950	7100	6350
Re_τ	186	172	180	183	171

Table 5.2: Scalar properties of the mean turbulent profile. Comparison with two DNS and two experimental data sets. These are the definitions of the various characteristics of the laminar profile. $\delta^* = \int(1 - U_z)dr$, $\Theta = \int U_z(1 - U_z)dr$, $H = \delta^*/\Theta$: integral shape factors for the mean profile U_z normalized by its mean centerline value. u_{CL}, U are the mean center-line velocity and mean streamwise velocity, respectively. $u_\tau = \sqrt{\tau_W/\rho}$: friction velocity based on the wall shear stress $\tau_W = \rho\nu(dU/dy)(y = 0)$. Re_{CL}: Reynolds number based on mean center-line velocity u_{CL}. Re_τ: Reynolds number based on u_τ.

shape of the laminar profile are in very good agreement, whereas those that mainly base on the slope at the wall show deviations of about 5%.

A direct comparison of the mean profile with experimental data from much higher Reynolds numbers is given in Fig. 5.6. Here the distance from the wall is given in wall units, $y^+ = (1 - r)/\delta_\nu$, where $\delta_\nu = \nu/u_\tau$ is the viscous length scale and u_τ is the friction velocity as defined in Tab. 5.2. At $y^+ \approx 20$ both data sets change from a linear to a logarithmic scaling ('law of the wall') but with slightly different constants.

A much more sensitive test on the numerical convergence is to not consider mean values like the mean profile or the mean energy spectrum but to focus on fluctuations. Fig. 5.7 shows the radial profiles of the root-mean-square (rms) velocity fluctuations, in wall units, compared to DNS literature data from [66]. The amplitudes as well as the the overall features are very similar, only the positions of the maxima differ slightly.

We are satisfied with these various reasonable good agreements. The comparison showed that we are able to reproduce experimental and numerical literature results on nonlinear turbulent pipe flow at Reynolds numbers that are considerably above the transition region we are mainly interested in.

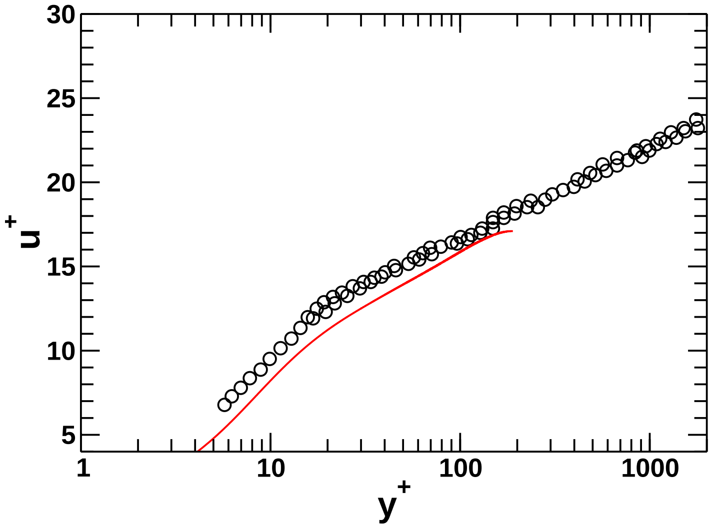

Figure 5.6: Mean velocity profile of turbulent pipe flow. Experimental data (circles) from Zagarola & Smits (1997) at $Re = 32000$ for $y/R < 0.1$, taken from [62], in comparison to the present results (line) for $Re = 5000$.

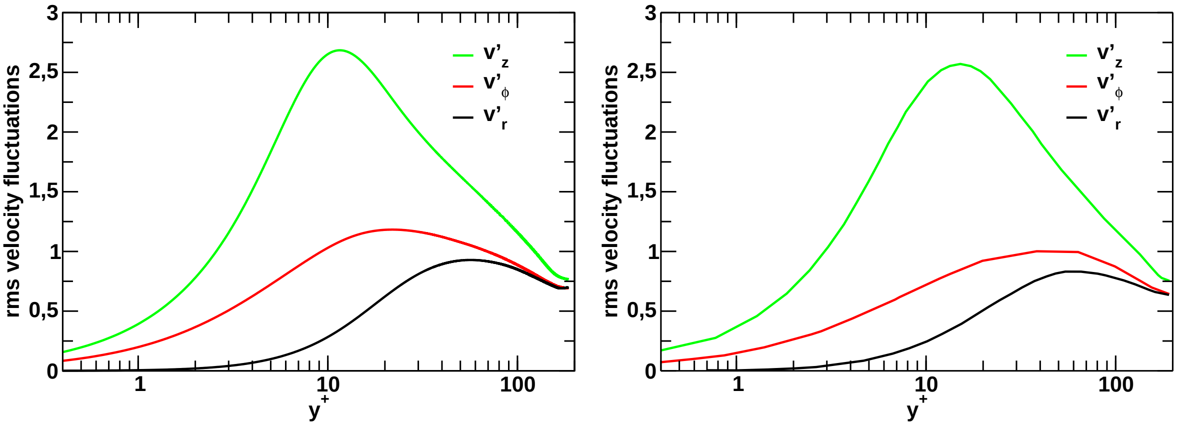

Figure 5.7: Radial profiles of rms velocity fluctuations in wall units at $Re = 5000$. Present work.

Figure 5.8: Radial profiles of rms velocity fluctuations in wall units at $Re = 4900$, taken from DNS data from [66].

Visualisations of the temporal evolution of the axially averaged flow field show important dynamical aspects of 3-d turbulent pipe flow: counter-rotating streamwise vortices transport slow fluid from near wall regions into the bulk and fast fluid from the bulk towards the boundary thus generating streamwise low-speed and high-speed streaks. This lift-up effect is well known from other shear flows. In Fig. 5.9 we exemplarily show the evolution of the streak-breakdown transition to turbulence which has already been introduced in section 5.2.

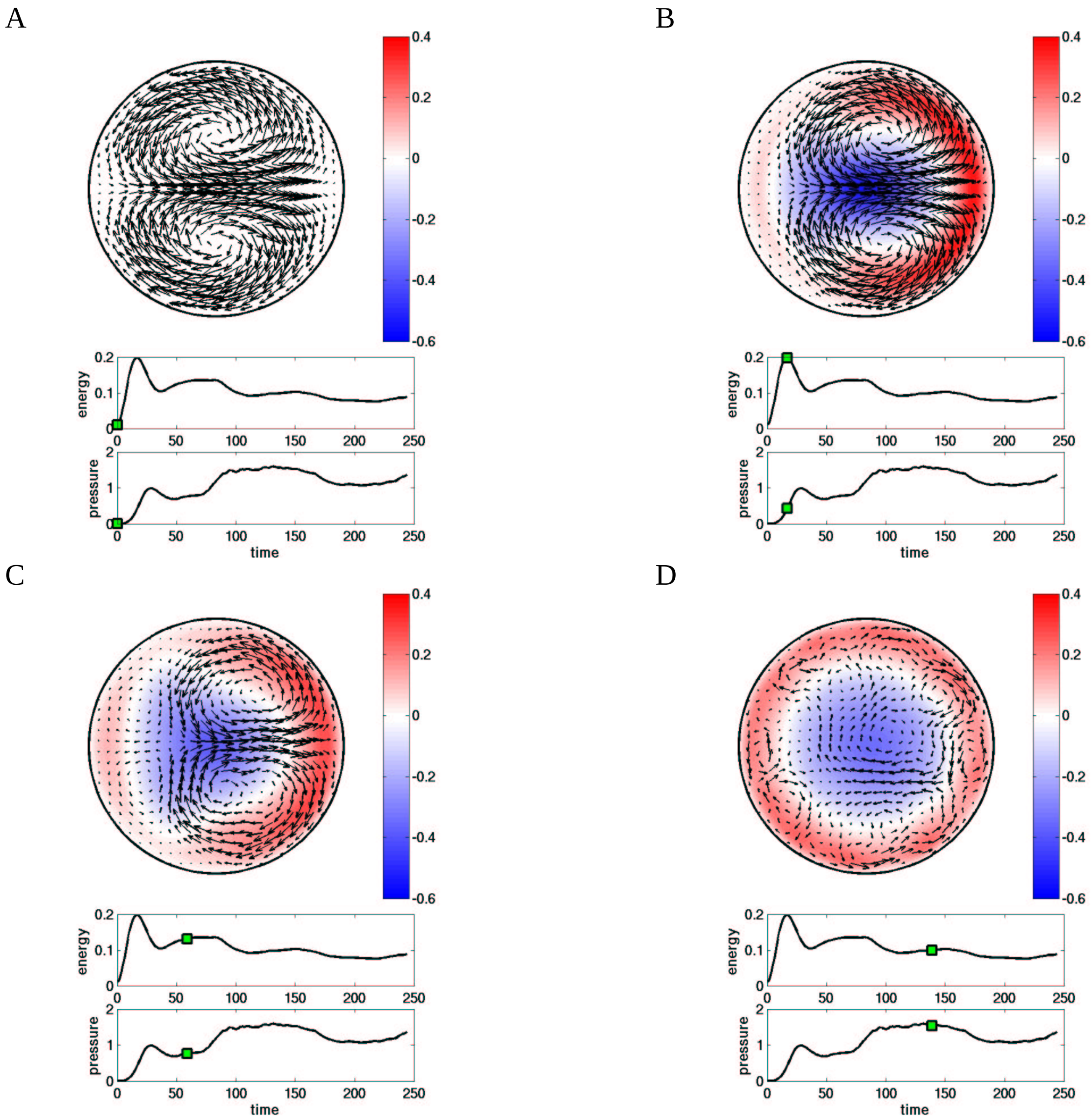

Figure 5.9: Snapshots of an animation illustrating the different stages of a well-controlled streak-breakdown turbulence transition process. The streamwise averaged deviation from the laminar profile is shown, arrows for the in-plane motion and color-coding for the axial component in units of the laminar center-line velocity. Re=3000 and the volume flux is fixed. Fig. A: Optimal (1,0)-’Zikanov’-mode chosen as initial condition. Fig. B: Lift-up. The vortex pair pumps the slow fluid from the left wall into the bulk, and the fast fluid from the center to the right wall, thus generating high-speed (red) and low speed (blue) streaks. Fig. C: Streak-breakdown. Initial very low-amplitude 3-d noise has been amplified by the inflection instability of the modified profile and destroys the (apparent) symmetry of the large vortex pair. Fig. D: Turbulence. Fluctuating high speed streaks close to the wall, large center region has considerably been slowed down, pairs of smaller vortices dominate the near wall dynamics.

5.3.2 Optimal resolution for transitional Reynolds numbers

Unfortunately it is not feasible to use the above resolution for our investigations since a single run over 2000 time units already takes about 25 CPU days on a 1.3 GHz IBM power4 processor. As a compromise we need a spatial resolution which is high enough to accurately represent the dynamics but low enough to enable us to obtain good statistics of many and long trajectories. We have to compare different spatial resolutions relative to each other as we do not have appropriate literature values for transitional Re. We compare a ’low’ resolution, $|n|/16 + |m|/14 \leq 1$ and 50 Legendre polynomials, a ’medium’ resolution, $|n|/20 + |m|/20 \leq 1$ and 50 Legendre polynomials, and a ’high’ resolution, $|n|/24 + |m|/20 \leq 1$ and 60 Legendre polynomials. The latter resolution has been proven above to be reasonably accurate even at $Re = 5000$. In all cases $L/R = 10$.

Fig. 5.10 shows the comparison of these resolutions for a turbulent run. Exemplarily, the turbulent friction factor as defined in Eqn. (6.8) is shown as a function of time. The first 200 time steps are neglected because of transients and the statistics is obtained over 1000 non-dimensional time units. The mean friction factor and its fluctuations have been extracted in Tab. 5.3 and it can be seen that they are rather independent of the resolution, all the more when taking neglected statistical errors into account. The lowest of the three resolutions has been employed for extensive statistics on sensitivity, lifetimes and Lyapunov exponents that will be presented in detail in chapter 7. The close agreement of the above results gives

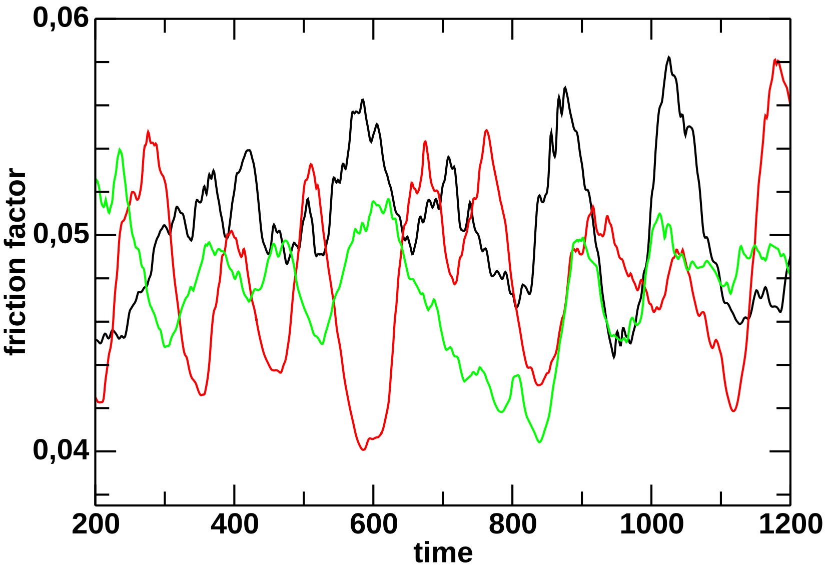

Figure 5.10: Turbulent friction factor fluctuations at $Re = 2500$. Comparison of three spatial resolutions: ’low’ (black line), ’medium’ (red line), and ’high’ (green line) resolution. For the statistics see Tab. 5.3.

resolution	f	rms
’low’	0.0503	2.90×10^{-3}
’medium’	0.0479	3.84×10^{-3}
’high’	0.0472	3.03×10^{-3}

Table 5.3: Turbulent friction factor and its rms fluctuations for three different spatial resolutions.

us considerable trust in the significance of this resolution for even lower Reynolds numbers between 1600 and 2200. Regularity and divergence are monitored continously during all time evolutions to guarantee that the relative errors stay below 10^{-12} throughout.

5.4 Conclusions

The new pipe code has been thoroughly tested and has passed all tests on the solution of linear and nonlinear pipe flow problems with spectral precision. In the framework of the Lagrange II mechanism, i.e. by a restriction to those velocity fields that obey the various constraints, the remaining number of degrees of freedom are minimized. This will be essential for the search for exact coherent states in chapter 6 which relies on algorithms that scale cubically with the total number of degrees of freedom. For simpler tasks like the solution of initial-boundary value problems in chapter 7 our code is not as optimized with respect to certain aspects such us memory usage and integration speed, but, nevertheless, the above test results have proven the significance of our simulations of turbulent pipe flow at transitional Reynolds numbers.

On the one hand an incredible amount of degrees of freedom (dof) is needed to quantitatively approximate experimental statistical results at twice the transitional Reynolds number, on the other hand there are severely truncated approximations to Navier-Stokes that already capture main features of transition in shear flows: in the thesis of A. Spille on plane Couette flow [80] from 1999 a severe approximation restricting to a total of four Fourier modes, corresponding to 108 degrees of freedom, could already identify the transitional Reynolds number to within 5%. In the work by Schmiegel & Eckhardt [73] from 1997 on the stability border in plane Couette 962 dof have been employed. In 2003 Meseguer [49] analysed the transition border in pipe flow with an emphasis on streak breakdown with a resolution of 1350 dof for Reynolds numbers of up to 10^4. These simulations are considerably lower resolved than the present simulations of turbulent trajectories that will be presented in chapter 7. There we will use the ’low’ resolution from section 5.3.2 which corresponds to 3.4×10^4 velocity coefficients and we will restrict ourselves to $Re \leq 2200$. This comparison further supports the significance of our results. When restricting the objective of the investigations to the simulation and analysis of only a single or very few turbulent trajectories, higher spatial resolutions are feasible [28, 46, 57, 66, 76, 90].

6 Exact coherent states in pipe flow

> “There are *no* good, general methods for solving systems of more than one nonlinear equation. Furthermore, it is not hard to see why (very likely) there *never will be* any good, general methods”
> *Numerical Recipes* [63]
>
> “…in one dimension, it is possible to [...] ’trap’ a root between bracketing values, and then hunt it down like a rabbit. In multidimensions, you can never be sure that the root is there at all until you have found it.” *Numerical Recipes* [63]
>
> “[...] multidimensional root finding becomes virtually impossible without insight”
> *Numerical Recipes* [63]

In the following we want to find exact coherent states in pipe flow. Previous studies of other shear flows [1, 15, 17, 29, 51, 53, 74, 93, 94] have shown that for sufficiently high Reynolds numbers 3-d coherent states exist beside the laminar profile. The existence of stationary states in plane Couette flow is connected with an inversion symmetry in the laminar profile. In the absence of such a symmetry in pipe flow the simplest states we can expect are travelling waves (TWs), i.e. coherent structures that move with constant wave speed.

Root finding to sets of nonlinear equations strongly relies on having good initial conditions from which the search is started. In low dimensional systems it is in general relatively easy to extract very good approximations to stationary and time periodic states from long chaotic time series [20, 78]. They serve as excellent initial conditions from which the exact solution can be quickly converged on by any standard root finding algorithm such as a Newton-Raphson method. This would be the method of choice as the dynamically most relevant states would be found most easily. But in high dimensions (in pipe flow we have to deal with thousands of degrees of freedom) this strategy is increasingly infeasible as the recurrence time to a neighborhood of an individual state grows rapidly with the number of dimensions.

Methods of high-dimensional root finding in this field often rely on brute force, where initial conditions are chosen more or less at random [80, 85], which is not satisfactory as it is an unsystematic and costly process. Alternatively it was tried to first find solutions to model systems that are generated by severe reductions of the spatial resolution. But when trying to increase the resolution again problems arise due to the very different phase-space structure of the model and the full system.

Embedding methods
have been highly successful in identifying coherent states in different linearly stable shear-flows. Here, the system is embedded into a family of systems. Consider, for instance, the example of plane Couette embedded into Taylor-Couette flow [33]. This results in a parameter dependence in such a way that for certain nonzero parameter values the flow is linearly destabilized. Series of symmetry breaking bifurcations can then be followed from the laminar profile and various coherent states can be identified (wavy-vortex flow in our example). A continuation of the states back to a vanishing parameter leads to exact coherent states in the original linearly stable system. Various examples exist for plane Couette flow. Its embedding into a rotating system, for instance, leads to nonlinear 3-d states that continue to the non-rotating system (rotating plane Couette flow [51, 54]; Taylor-Couette flow [33]). Further examples are plane Poiseuille-Couette flow [1, 15, 53, 94], Bénard-Couette flow [17], or the modification by an electrically conducting fluid in the presence of a transverse magnetic field [52].

Before presenting our strategy to find coherent states in pipe flow we give an instructive example of the embedding of pipe flow into rotating pipe flow. It has not been possible to continue 3-d solutions to the non-rotating system in this case.

6.1 Earlier attempts to find coherent states in pipe flow

Barnes & Kerswell [3] investigated in travelling waves in rotating pipe flow where fluid is driven by a constant pressure gradient along a pipe which is rotating axially as well as about a perpendicular diameter, i.e. a rotating and precessing pipe. For a sketch of their bifurcation diagram see Fig. 6.1 (taken from [3], modified). Low axial rotation rates are known to lead to a linear instability of the laminar profile [47] from which nonlinear two-dimensional helical waves emerge [86]. Different branches of travelling waves that bifurcate from the linearly unstable laminar flow have been followed but none of them could be continued to pure (non-rotating) Hagen-Poiseuille flow. As the type of the primary and secondary bifurcations stays a forward Hopf bifurcation the reduction of the rotation rates always leads to a reconnection with the laminar flow.

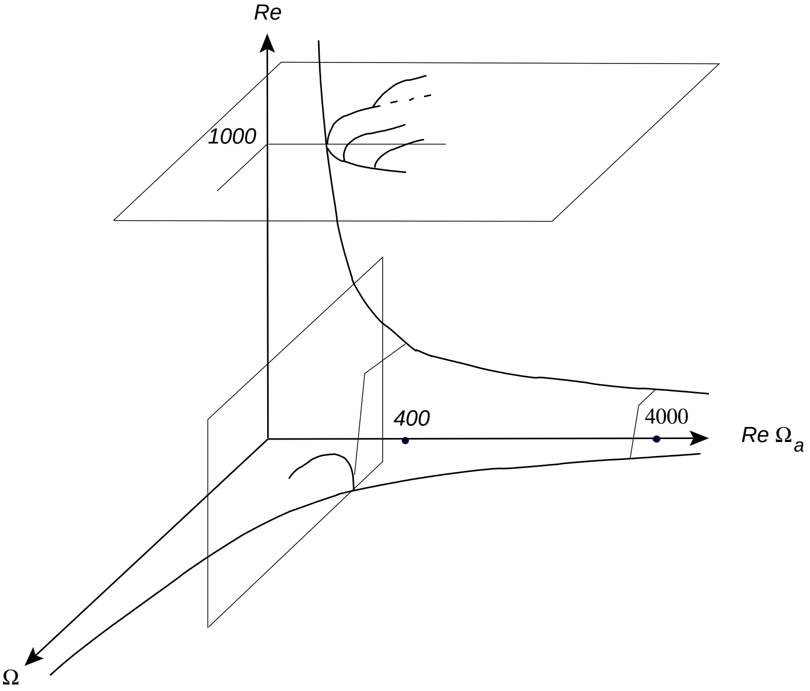

Figure 6.1: Sketch of the bifurcation diagram for travelling waves in *rotating* and *precessing* pipe flow, from [3]. The vertical axis denotes the usual Reynolds number Re based on the mean streamwise velocity, Ω_a denotes the axial rotation rate, and Ω depicts the perpendicular rotation around a diameter. Various branches of forward bifurcations have been followed that all reconnect to the laminar profile in the limit of the non-rotating pure Hagen-Poiseuille problem $\Omega = \Omega_a = 0$.

6.2 Embedding method with transversal volume force

Our search begins at a low Reynolds number of a few hundreds where a large amplitude volume forcing is added to generate a transverse flow. At first this is a mathematical trick only. But, presumably, approximations to these volume forces could be achieved experimentally by differential heating and cooling of the pipe wall as predicted by the symmetries of the states, or by magnetic forcing in an electrically conducting fluid [52]. For the types of forcing discussed further below and for a sufficiently low Reynolds number a narrow parameter interval can be identified where the forced 3c-2d solution (three velocity components as functions of the two spatial dimensions r and ϕ) dynamically follows a supercritical bifurcation which is due to an inflectional instability. The solution nonlinearly saturates into a stable 3c-3d forced travelling wave. A path following scheme (cf. section 4.7) is then used to track this state through parameter space: the Reynolds number is increased and the amplitude of the body force decreased. When the artificial volume forcing is reduced the ’natural’ internal forcing (i.e. the shear due to the laminar Hagen-Poiseuille profile) has to be increased and has to take over the driving of the TW-structure. We therefore need to design a forcing and a velocity field topology which finally can be driven solely by the Hagen-Poiseuille shear. If a situation with zero body force can be reached, a nonlinear TW for the original pipe flow is found. Here we do not restrict ourselves to volume forces that necessarily have a specific physical realisation such as centrifugal forces, for instance. This gives us the freedom to choose any topology of volume force that seems to be a good candidate. The big advantage here is that one can systematically probe the system for the existence of a state of a certain topology, so that even in the case when one does not find a solution one might have learned something about which topologies (of streaks and vortices) cannot be supported by the flow and why.

A similar approach has been employed by Waleffe [93] for plane Couette flow which in turn had been motivated by the work of Benney [4] on approximate steady states. The major difference, however, is that in that case the existence and properties of the wavy-vortex flow state to be found had been known in advance by the work of Nagata [51] and Busse & Clever [17] for the no-slip boundary-condition case.

So if a nonlinear TW for the original pipe flow is found it corresponds to an element of a two-dimensional continuum of waves, spanned by the viscosity ν and the streamwise periodicity L. In comparison to other shear flows, the parametric study is simplified due to the trivial periodicity in azimuthal direction. Here the fundamental azimuthal wavenumbers are discrete and only the lowest are relevant for transitional Reynolds numbers.

The continuation method is implemented with a spatial resolution of $|\tilde{n}|/10 + |m|/10 \leq 1$, i.e. up to 21 modes in azimuthal direction and downstream direction. In this chapter we modify the notation slightly as only integer multiples of n are needed as azimuthal wavenumbers, where n is fixed by the index of the C_n symmetry and the azimuthal expansion functions are $\exp(i\tilde{n}n\phi)$. Usually 44 Legendre polynomials have been used radially. These are about 8700 dynamically active velocity coefficients for the calculation of the Navier-Stokes equation. By single-value decomposition of the projector on the correct subspace of velocity fields (see section 4.6) the problem is reduced onto the ≈ 4300 dimensional span of the projector. For a check on the numerical convergence of the results the radial resolution has been increased up to 56 polynomials corresponding to about 11000 velocity coefficients and a 5600 dimensional span. Details on the numerical convergence of the states are discussed in Appendix B. Following a state through parameter space, a single small step takes about 2h on an IBM Power 4, 1.3 GHz processor. The memory demand without the preceding initial construction of the projection operators and its SVD is about 700MB RAM.

In the following we test pipe flow for the existence of most 'basic' TWs: $2n$-vortex TWs in section 6.3 and 6.4, spiral TWs in section 6.5. The conclusions will be given in section 6.6.

6.3 $2n$-vortex travelling waves

What structure do we expect for the most 'basic' travelling waves? We expect the lowest states to have high spatial symmetry and to be dominated by largest scale flow patterns that have smallest gradients, i.e. smallest dissipation, but to be still able to extract a maximum amount of energy from the laminar profile.

The first travelling waves we aim for are dominated by pairs of counter-rotating streamwise vortices. This choice is guided by various observations. First of all those vortical structures are most prominent in stationary and travelling states in other shear flows such as plane Couette, Taylor-Couette or plane Poiseuille flow. Large streamwise streaks have also been reported from the leading laminar-turbulent interface of turbulent puffs in pipe flow, both experimentally [30] and numerically [76]. Near-wall coherent structures in turbulent wall flow show similar streamwise streaks and vortices as well [41].

The forcing for the streamwise invariant $2n$-vortex flow is based on a simple lowest-order polynomial ansatz. We require zero divergence, no-slip boundary conditions, and a regular solution of the Poisson equation, from which the corresponding force field is derived in a next step[1]. With this ansatz for the model flows with azimuthal wavenumber $n > 1$ we constructed the following velocity field **u**,

$$\mathbf{u}_n(\mathbf{r}) = \begin{pmatrix} inr^2(r-1)^2 \\ r^2(-3+8r-5r^2) \\ 0 \end{pmatrix} e^{in\phi} + cc\,, \tag{6.1}$$

where *cc* denotes the complex conjugate. These are 2c-2d velocity fields, two velocity components as a function of two spatial dimensions. These $2n$-vortex flows of symmetry C_n are visualized in Fig. 6.2. The case of a single vortex pair ($n = 1$) will be discussed later in section 6.4.

To derive the corresponding volume forcing $\mathbf{F}(\mathbf{r})$ we start from the (forced) linearization of the Navier-Stokes equations 4.4 for the r and ϕ component,

$$\begin{aligned} \partial_t u_r + \mathbf{e}_r \cdot (\mathbf{u}\cdot\nabla)\mathbf{u}^0 + \mathbf{e}_r \cdot (\mathbf{u}^0\cdot\nabla)\mathbf{u} = \\ = \nu\left[u_r'' + \frac{1}{r}u_r' - \left(\frac{1-\partial_{\phi\phi}}{r^2} - \partial_{zz}\right)u_r - \frac{2}{r^2}\partial_\phi u_\phi\right] + F_r \end{aligned} \tag{6.2}$$

---

[1] Note that for this model flow we do not require analyticity in a neighbourhood of the pipe center line (cf. Theorem 4.1, page 20). In our numerics of course only (arbitrary close) analytical approximations are employed.

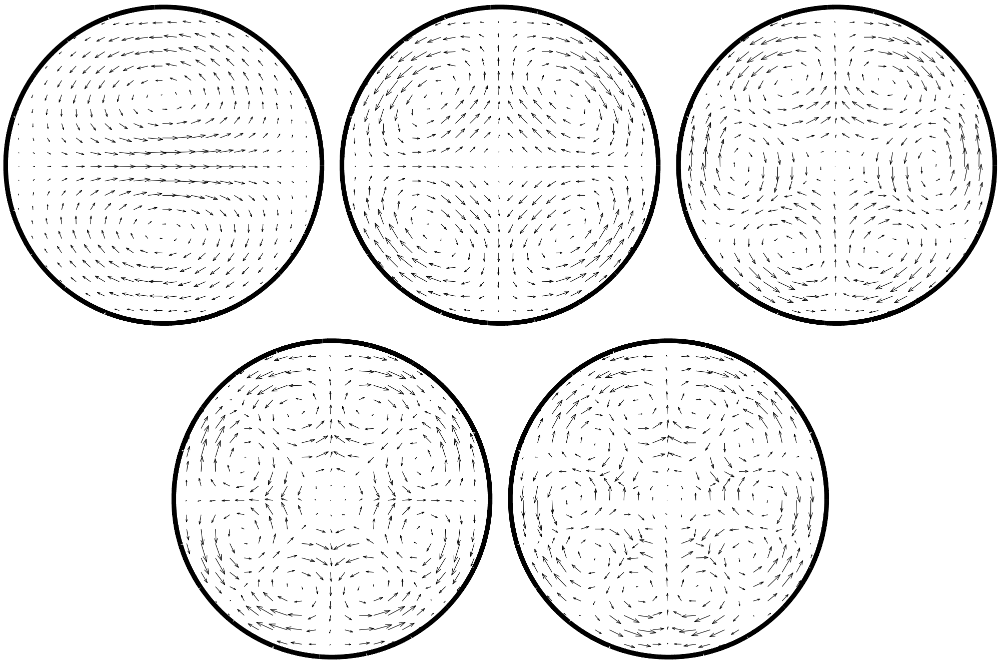

Figure 6.2: Model $2n$-vortex flows of C_n-symmetry, $n = 1, \ldots, 5$ (for the case $n = 1$ see section 6.4). These fields are not solutions to the Navier-Stokes equations but they are chosen to be divergence free and satisfy no-slip boundary conditions at the wall and their corresponding forcing is regular at the origin. They are streamwise invariant and they each consist of a single Fourier mode with azimuthal wavenumber n. With the corresponding volume forcing, which is the solution to the Poisson equation for these modes, one might be able to hunt down the travelling waves of same topology. The aspect ratio of an individual vortex seems to be optimal for the hexagonal 6-vortex mode which indeed leads to the travelling wave of lowest critical Reynolds number in the end.

$$\begin{aligned}\partial_t u_\phi + \mathbf{e}_\phi \cdot (\mathbf{u}\cdot\nabla)\mathbf{u}^0 + \mathbf{e}_\phi \cdot (\mathbf{u}^0\cdot\nabla)\mathbf{u} &= \\ = \nu\left[u''_\phi + \frac{1}{r}u'_\phi - \left(\frac{1-\partial_{\phi\phi}}{r^2} - \partial_{zz}\right)u_\phi + \frac{2}{r^2}\partial_\phi u_r\right] &+ F_\phi \,. \end{aligned} \tag{6.3}$$

If we assume a single stationary, streamwise invariant mode, $\mathbf{u} = \mathbf{u}(r)\exp(in\phi)$, the equations boil down to the Poisson equation for this mode,

$$\begin{aligned} 0 &= \nu\left[u''_r + \frac{1}{r}u'_r - u_r\frac{1+n^2}{r^2} - \frac{2}{r^2}inu_\phi\right] + F_r \\ 0 &= \nu\left[u''_\phi + \frac{1}{r}u'_\phi - u_\phi\frac{1+n^2}{r^2} + \frac{2}{r^2}inu_r\right] + F_\phi \,. \end{aligned} \tag{6.4}$$

As the Poisson equation is linear the forcing $\mathbf{F}(\mathbf{r})$ will be divergence free as well. The volume forcing which is a solution to the Poisson equation (6.4) for the $2n$-vortex model

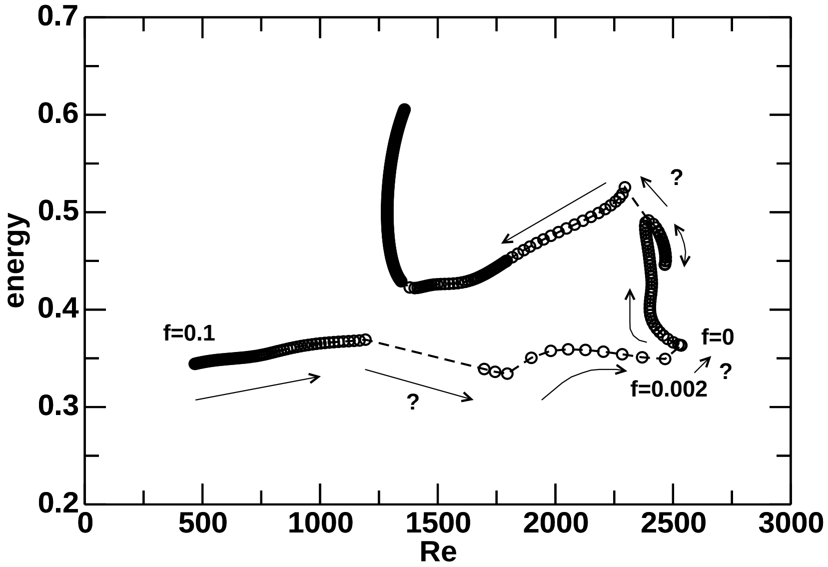

Figure 6.3: Energy vs. Re diagram of the non-trivial continuation process from the forced to the unforced C_3-symmetric state. The development of the solution is often surprising and far from straightforward. Sometimes larger parameter changes help to overcome being stuck in an unwanted solution branch like the rightmost C_3-symmetric unforced branch that does not seem to be connected to the TW that is discussed below and bifurcates at $Re = 1250$. A reduced numerical solution is employed here.

flow (6.1) is

$$\mathbf{F}_n(\mathbf{r}) = f\nu \begin{pmatrix} in(n^2 - 9 + r(32 - 2n^2) + r^2(n^2 - 25)) \\ 9 - n^2 + r(4n^2 - 64) + r^2(75 - 3n^2) \\ 0 \end{pmatrix} e^{in\phi} + cc\,. \tag{6.5}$$

Here an additional factor f has been introduced as a scalar forcing amplitude. Note that the above choices are not unique as other functional forms are possible. If they are successful a whole class of model-velocity and force fields will exist that all converge to the same travelling wave. Of course the transverse velocity fields constructed above are only solutions to the *linear* forced Navier-Stokes equations. The nonlinear dynamical time evolution will lead to a modified mean profile which then gives rise to a nonlinear feedback on the modes: the corresponding streamwise streaks will develop.

The continuation process of reducing the force and finding the unforced TW is far from being straightforward. Some of the difficulties become obvious in Fig. 6.3 where the C_3 symmetric case is shown exemplarily.

Finally, the above techniques have been successful and a family of three-dimensional (unforced) travelling waves has been identified.

They originate in finite amplitude saddle-node bifurcations so that away from the bifurcations there is an upper (nodal) and a lower (saddle) branch. We have identified four different states of discrete rotation symmetry C_n. An n-fold symmetry C_n is defined by the invariance under rotation around the pipe axis by an angle $2\pi/n$, i.e.

$$\begin{pmatrix} u_r \\ u_\phi \\ u_z \end{pmatrix} (r, \phi, z) = \begin{pmatrix} u_r \\ u_\phi \\ u_z \end{pmatrix} (r, \phi + 2\pi/n, z)\,. \tag{6.6}$$

The lowest critical Reynolds number, $Re = 1250$, is obtained for the TW with three-fold rotational symmetry in azimuthal direction, C_3, for which the arrangement of vortices is optimal in the sense of being closest to a hexagonal packing, the preferred pattern in other systems.

In analogy to the instability of wakes and other model streaky flows [92] two types of linear instability could be expected: one leading to ’fundamental sinusoidal’ modes, the other leading to ’subharmonic sinucose’ modes. The first type is invariant with respect to the shift-and-reflect symmetry,

$$\begin{pmatrix} u_r \\ u_\phi \\ u_z \end{pmatrix} (r, \phi, z) = \begin{pmatrix} u_r \\ -u_\phi \\ u_z \end{pmatrix} (r, -\phi, z + L/2)\,, \tag{6.7}$$

the latter is invariant with respect to the simple reflection symmetry without the streamwise shift.

The 3-d states that bifurcated first always showed the first type of symmetry which was then explicitely exploited in the following continuation as described in section 4.6. It is based on a streamwise shift of half a pipe length and an additional reflection with respect to a midplane of the cross-section. This is completely analogous to the shift-and-reflect symmetry of the lowest coherent state, wavy-vortex flow, in plane Couette, plane Poiseuille and Taylor-Couette flow [17, 51, 94].

Fig. 6.4 shows cross-sections of the travelling C_n-symmetric waves for $n = 2, \ldots, 5$. All these states have a similar topology: they have $2n$ streaks of fast fluid close to the wall and streaks of slow fluid towards the center. The high-speed streaks near the wall remain fairly stationary over one period of the wave, and the low speed streaks in the center oscillate vigorously.

The structure of the waves is governed by vortices which have a predominant downstream orientation and which are slightly tilted inside the volume. They resemble near wall coherent structures which have been observed experimentally and numerically in turbulent wall flows [41]. They are responsible for the ’lift-up’, that is, they transport slow fluid towards the center and fast fluid towards the wall, thus producing the high- and low-speed streaks (all speeds are relative to the laminar profile for that Reynolds number). The resulting steeper gradients near the wall imply higher friction losses, i.e. higher dissipation and higher pressure gradients for the same flow speed. So the main flow features depend on these vortices and any modifications lead to drastic changes: non-Newtonian additives as well as constant axial rotation or axial oscillation interfere with near-wall vortical structures (although by different mechanisms) and considerably reduce the growth of streamwise streaks and therefore the turbulent friction (’drag reduction’, up to 40% by axial oscillations [66], up to 80% by polymer additives [65, 81]).

To further clarify the three-dimensional structure of the dominant streamwise vortices Fig. 6.5 shows a contour plot of the streamwise vorticity field for the C_3-symmetric state. It can be seen how the contours of positive and negative vorticity are entwined. The vortices emerge near the wall and they are tilted azimuthally depending on the sign of rotation. Clockwise and counter-clockwise vortices are advected in clockwise and counter-clockwise direction, respectively. At the same time they develop towards the bulk where pairs of vortices annihilate.

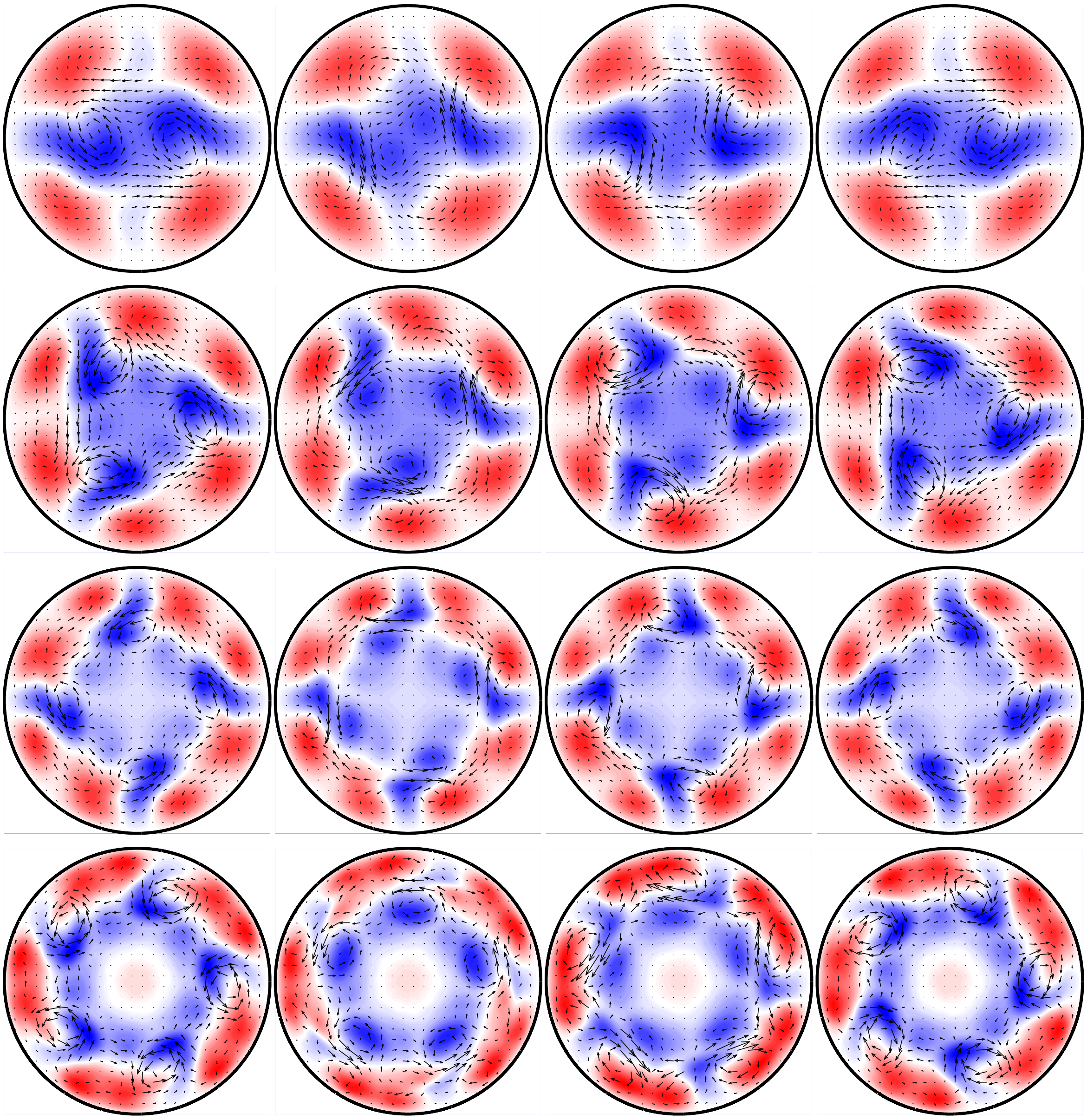

Figure 6.4: Cross-sections of travelling waves at their respective bifurcations. C_2,…,C_5-symmetric waves are displayed from top to bottom. From left to right the frames are cross sections at different downstream positions separated by $\Delta z = L/6$. Only half a period is shown: the last frame is the same as the first one up to a reflection at the horizontal diameter ($\phi \to -\phi, u_\phi \to -u_\phi$). Note that the high speed streaks near the wall move much less than the low speed streaks closer to the center. Velocity components in the plane are indicated by arrows, the downstream component by color coding: velocities faster than the parabolic profile are shown in red, slower ones in blue. For quantitative details see Tab. 6.1. The C_1-symmetric situation is discussed in section 6.4.

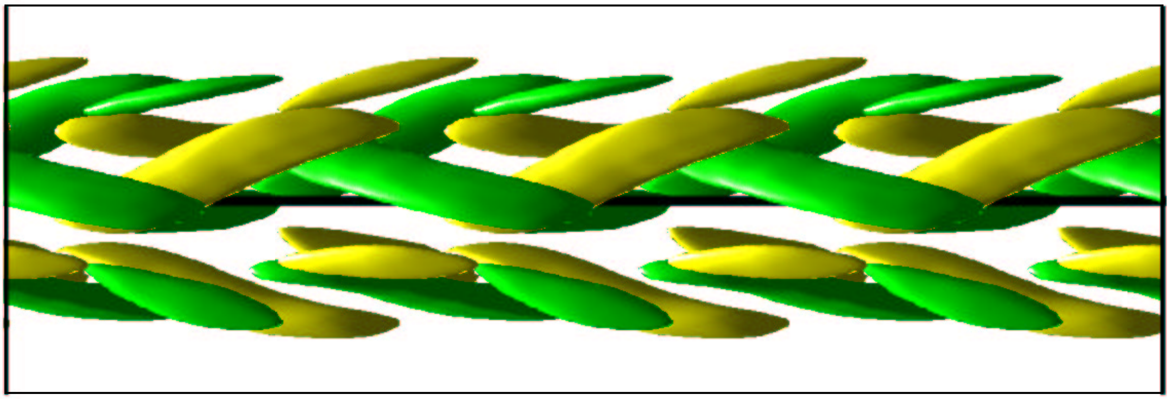

Figure 6.5: Three-dimensional side view of iso-contours of the streamwise vorticity field ω_z for the C_3-symmetric travelling wave at the bifurcation to clarify the spatial structure of the streamwise vortices. Three fundamental streamwise periods of total length $L/R = 7.44$ are shown. The two iso-contours are at $\pm 40\%$ of the maximum streamwise vorticity. The black line is the pipe center-line for orientation. The flow goes from left to right.

Several properties of these states are listed in Tab. 6.1. The state with C_5-symmetry is not included in the table as it seems to be the one which is most sensitive to the numerical resolution and not fully converged. A preliminary estimate for its critical Reynolds number is about 2600. The C_1-symmetric situation is discussed in section 6.4.

symmetry	C_2	C_3	C_4
Re_c	1350	1250	1590
L_c/R	4.19	2.58	2.51
v/U	1.43	1.29	1.17
n_u	2	1	4
u_s/U	0.38	0.35	0.34
u_p/U	0.035	0.046	0.045
E	0.621	0.555	0.574
$E_{3d}/10^{-3}$	0.828	1.82	1.47

Table 6.1: Selected properties of travelling waves at the saddle-node bifurcation. Given is the critical Reynolds number Re_c at the optimal wave length L_c, the phase velocity v and the number n_u of unstable dimensions. u_s is the maximum deviation of the streamwise velocity from the laminar flow, u_p is the maximum in-plane velocity component. E is the total energy and E_{3d} the energy content in the streamwise dependent part of the velocity field, both in units of the laminar energy.

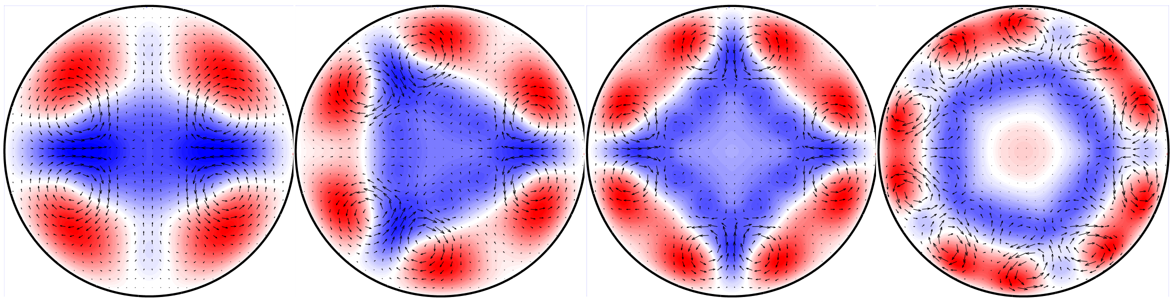

Figure 6.6: Travelling waves with symmetries C_n with $n = 2, 3, 4$ and 5 at the bifurcation. In order to highlight the topology of the states all states are averaged in downstream direction. The representation of the velocity field by vectors (in-plane motion) and color (downstream component) is as in Fig. 6.4. The absolute scale for the velocity fields is given in Tab. 6.1. Note the respective structural similarity between the C_2- and C_3-symmetric states and the linear eigenmodes ’EV2’ in Fig. A.3 and A.4 in Appendix A.

The Reynolds number is not a good continuation parameter as it explicitely depends on the state’s mean profile, i.e. on a *small* fraction of the velocity coefficients. Instead the kinematic viscosity ν is kept as a free parameter for the continuation method and the Reynolds number is determined by the mean downstream velocity U of the TW. The mean flow velocity as well as the phase velocity v of the wave depend on its shape and structure and are not known in advance.

The C_n-symmetric travelling waves are axially averaged in Fig. 6.6 in order to highlight the dominant streamwise elements of the vector fields. The close relationship between the vortical structures and the original model flows in Fig. 6.2 is noticeable, however, two vortices each arrange in pairs along the side of their radial inwards flow.

Fig. 6.7 shows the averaged effect of the high speed streaks near the boundary and the low speed streaks in the bulk: the mean profile is steeper at the wall and flatter in the center, a feature it has in common with the mean turbulent profile. The maximum relative deviation from the laminar profile is 15%.

The amplitudes of the velocity fields reflect the non-normal amplification that dominates the linear evolution: small transverse components can produce strong downstream streaks. Tab. 6.1 shows that for the TWs the transverse components are about an order of magnitude smaller than the differences between the downstream components of the laminar profile and the TW.

Each TW is part of a continuum of states that exists for a range of downstream wave lengths. The range increases with Reynolds number and varies with the symmetry (Fig. 6.8). The

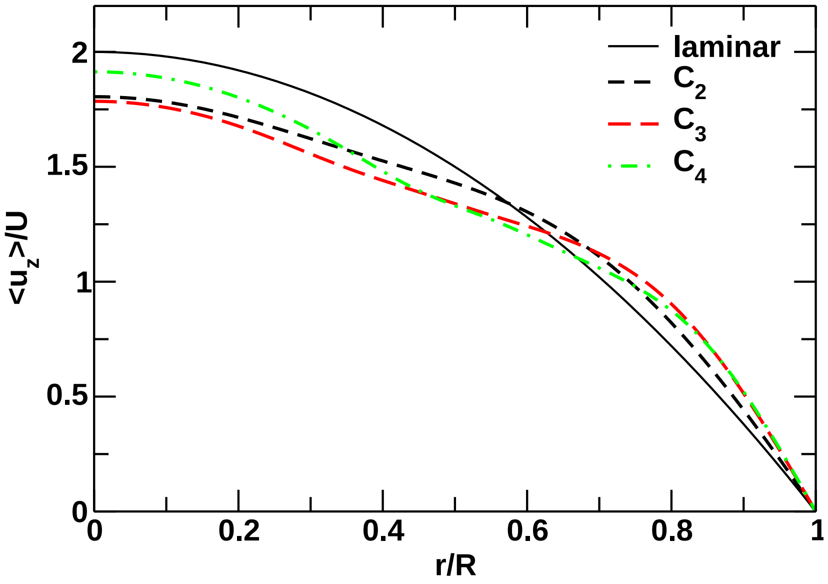

Figure 6.7: Mean downstream velocity profile of the travelling waves with C_n-symmetry, $n = 2, 3, 4$, in units of the mean streamwise velocity at the bifurcation. The TWs steepen the profile at the wall and flatten it in the bulk.

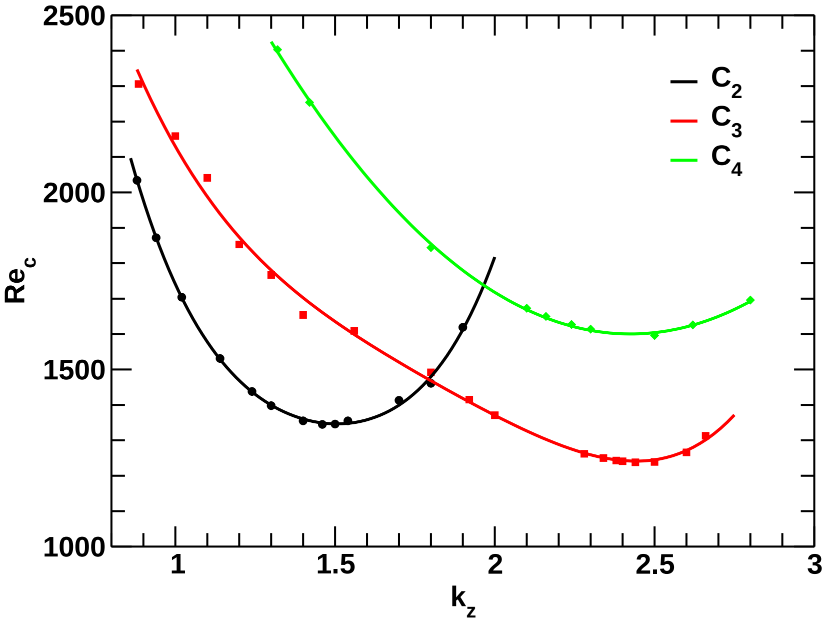

Figure 6.8: Dependence of the critical Reynolds number on the downstream wavenumber for the two-, three-, and fourfold symmetric state. The numerical values (symbols) are interpolated by a 4th-order polynomial fit (lines). The solutions extend to higher and lower wavenumbers than shown.

lowest critical Reynolds number is obtained for a wavelength of about $4.2R$ for the twofold symmetry and about $2.5R$ for the three- and fourfold symmetric state. This seems to be

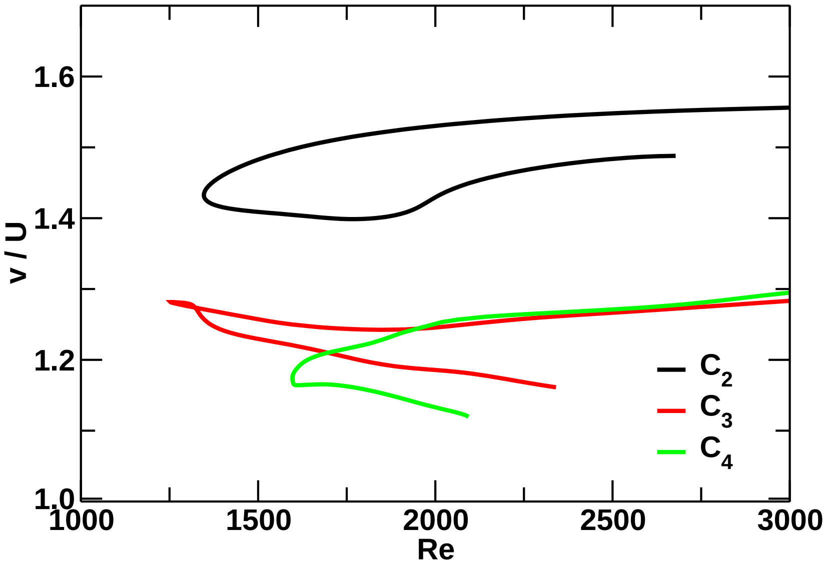

Figure 6.9: Phase velocities of the travelling states at optimal wavelength as a function of Reynolds number. The velocities are normalized by the respective downstream velocity. The solutions extend to higher Reynolds numbers than shown.

shorter than the lowest state in plane Couette flow where the optimal wavelength is about $2\pi d$ with d the gap width. However, when the wedge shape of the boundary is taken into account and the lengths are compared to the widths, the comparison is more favorable: the ratio widths to lengths is about 2π:4π = 1:2 in plane Couette flow and about 1:2.5 in pipe flow.

The fact that the maximum optimal wavelength is just below $L = 5R$ nicely fits together with the numerical observation by Eggels *et al.* [28] that velocity fluctuations in turbulent flows are decorrelated for streamwise distances larger than $5R$ at transitional Reynolds numbers.

All the above wavelengths are at least an order of magnitude smaller than the typical extension of turbulent slugs or puffs. These reproducible enveloping structure have typical extensions of 60 pipe radii or more and are based on unknown large scale effects.

The downstream phase speed v of the TWs is a function of both parameters, length and Reynolds number. Its Reynolds number dependence at optimal wavelengths is shown in Fig. 6.9. In all cases the phase speed is slower than the maximal speed possible with a laminar fluid and larger than the mean speed , i.e. the wave still propagates downstream when viewed from a frame of reference moving with the mean flow velocity. This is similar to the leading laminar-turbulent interface of a turbulent puff and slug, which propagates with a speed larger than the mean flow (see chapter 3), and where wave-like solutions could be active.

Bifurcation diagram

We compare the friction properties of the waves with experimental and numerical results for turbulent friction as well as with laminar friction in Fig. 6.10.

The friction factor f is defined as

$$f := \frac{\Delta p}{L} \frac{2R}{\frac{\rho}{2} U^2} \tag{6.8}$$

with the pressure drop Δp over the pipe length L and with the fluid density ρ [62]. It is equal to four times the skin-friction coefficient, $f = 4C_f$. From the laminar Hagen-Poiseuille profile a laminar friction law of $f_{\text{lam}} = 64/Re$ follows. Approximating the mean turbulent profile by a logarithmic profile and fitting the constants to experimental data leads to Prandtl's friction law for smooth pipes [62], which is an implicit formula for the turbulent friction as a function of Reynolds number

$$\frac{1}{\sqrt{f}} = 2 \log(\sqrt{f} Re) - 0.8 \, . \tag{6.9}$$

The saddle-node bifurcations take place at Reynolds numbers significantly below the values where typical perturbations induce turbulent dynamics. At the bifurcation the friction factor is higher than the value extrapolated from turbulent states at higher Re. With increasing Reynolds number the friction factor for the TWs seems to follow the laminar scaling. This has not been expected. The upper branches in Fig. 6.10 correspond to the lower branches in Fig. 6.9: states with higher friction have lower phase velocity and vice versa.

Stability analysis

Information about the linear stability of the states has been obtained by solving the full eigenvalue problem for the equations of motion linearized around the travelling waves. All states have shown to be already unstable at the saddle-node bifurcation. This is in contrast to plane Couette flow where at least the lowest state has an interval of stability, although a tiny one [17]. However, the unstable manifold is extremely low-dimensional, see Tab. 6.1. Exemplarily the eigenvalue spectrum of the C_3-symmetric wave at its bifurcation is shown in Fig. 6.11, where one unstable and one neutral eigenvalue from the saddle-node bifurcation can be identified, as compared to thousands of stable ones. One additional neutral eigenvalue corresponding to the streamwise translation invariance of the wave is not captured in the numerics. The upper branch (node) of the saddle-node bifurcation initially has one more stable eigenvalue than the lower branch (saddle) until both of them independently undergo further bifurcations leading to higher ('quaternary') states, which are beyond the present analysis.

Let us consider whether the maximal growth rates of the travelling waves at the bifurcation are 'large' or 'small'. The appropriate time scale to compare with seems to be the period

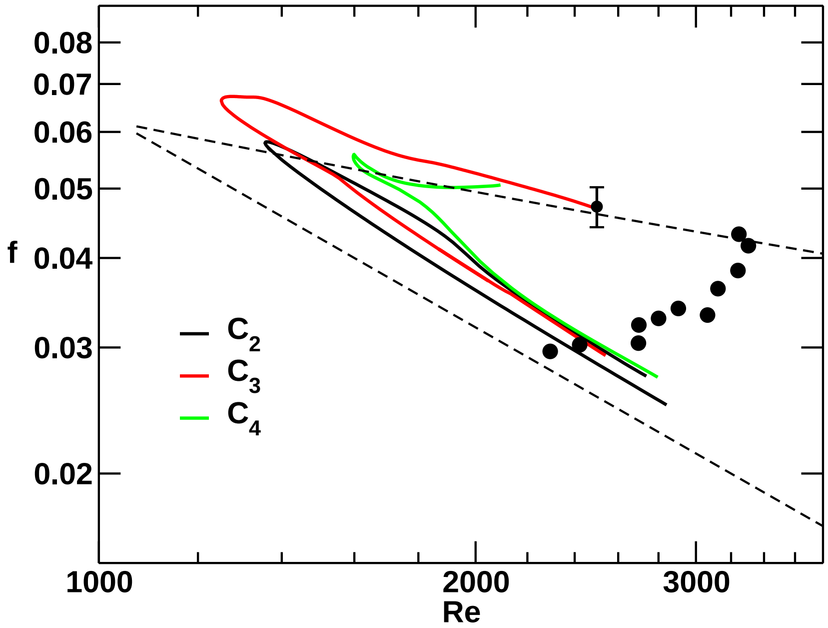

Figure 6.10: The bifurcation diagram for travelling waves together with turbulent states in pipe flow. Shown is the friction factor as defined in Eq. (6.8) vs. Reynolds number. The lower dashed straight line indicates the strict lower bound from the laminar profile, the upper dashed line corresponds to Prandtl's friction law, Eq. (6.9). The full circles are experimental data taken from [71] or from the present numerical simulations (the value at $Re = 2500$ with rms deviation). The wave solutions extend to higher Reynolds numbers than shown.

of the wave, i.e. the time it takes the phase of the wave to travel one wavelength. For this quantity, $\lambda/[v/L]$, we get the values $0.022, 0.018, 0.047$ for $n = 2, 3, 4$, respectively. This is considerably smaller than 1, so all three waves are only slightly unstable and the growth rates of the linear instability are 'small'. This enhances the experimental chances to stabilize and control these structures.

Comparison at $Re = 2000$

Let us look at the changes of the individual solution branches with increasing Reynolds number. The upper and lower branches of the C_2, C_3 and C_4 state are compared at $Re = 2000$ in Fig. 6.12 at their respective optimal wavelength. Again the streamwise averaged flow is shown in order to concentrate on the streamwise streaks and vortices.

Both the upper and the lower C_2-symmetric branch have a structure which is still very similar to that at the bifurcation, only the middle horizontal stripe of low speed streaks becomes narrower in the lower branch. For the C_3- and C_4-symmetric wave the most prominent change is the fusion of two neighbouring high-speed streaks in the lower branch. In summary, the lower branches appear to develop a more streamlined structure.

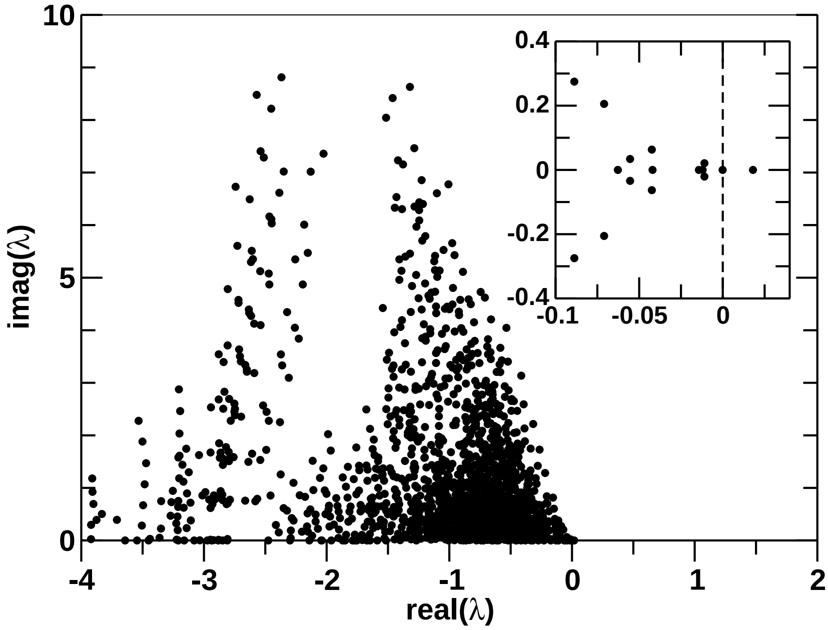

Figure 6.11: Part of the eigenvalue spectrum of the lowest travelling wave (C_3) at the bifurcation. Eigenvectors are real or come in complex conjugate pairs. One unstable and one neutral eigenvalue from the saddle-node bifurcation can be identified.

	$C_{2,u}$	$C_{2,l}$	$C_{3,u}$	$C_{3,l}$	$C_{4,u}$	$C_{4,l}$
u_s/U	0.19	0.175	0.13	0.15	0.11	0.13
u_p/U	0.011	0.008	0.012	0.013	0.012	0.017

Table 6.2: u_s is the maximum deviation of the streamwise velocity from the laminar flow, u_p is the maximum in-plane velocity component.

6.4 Search for C_1-symmetric two-vortex travelling waves

For the n=1 case we have chosen to force Zikanov's optimal mode (see section 5.2) since it already has the topology of streaks we are looking for and since it fulfills the same conditions as the fields for the case $n > 1$ above (no-slip, divergence free, regular forcing, low order polynomial) [2]. The precise velocity field has already been introduced in Eqn. 5.6 in section 5.2. The corresponding forcing is

$$\mathbf{F}_1(\mathbf{r}) = f\nu \begin{pmatrix} 24 - 30r \\ i(24 - 60r) \\ 0 \end{pmatrix} e^{i\phi} + cc, \tag{6.10}$$

which is obtained from the Poisson equation for the $n = \pm 1, z = 0$ mode.

---

[2] As for the $2n$ model flows we do not require analyticity in a neighbourhood of the pipe center line (cf. Theorem 4.1, page 20). In our numerics of course only (arbitrary close) analytical approximations are employed.

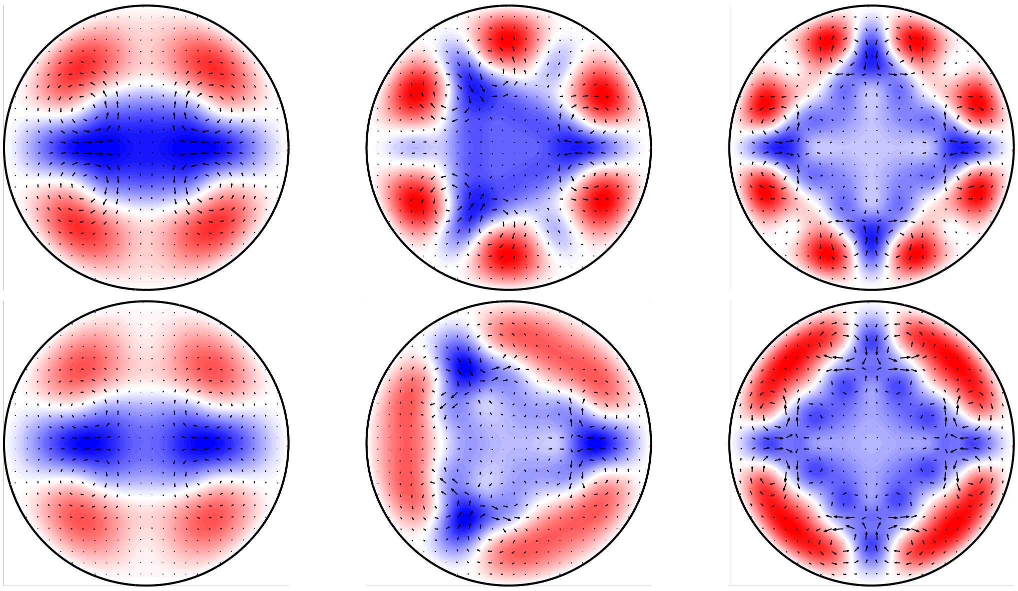

Figure 6.12: Axially averaged upper and lower branch of the C_n-symmetric states, $n = 2, 3, 4$, at $Re = 2000$.

The upper row shows the upper branch, the lower row shows the lower branch; n increases from left to right. For the vector plots of the in-plane velocity the same scale has been used so they are directly comparable. The streamwise velocity component is as usual given by color-coding, with red faster than the laminar flow and blue slower, but the color scaling has been optimized for each individual graph. The maximum in-plane and streamwise velocities are listed in Tab. 6.2.

This two-vortex ('Zikanov'-) flow is visualized in Fig. 6.2.

At a low Reynolds number ($Re = 100$) and a high forcing amplitude ($f = 0.3$) the state dynamically bifurcates with a critical streamwise wavelength of about ($\pi \pm 20\%$). So we begin our search with $k_z = 2$ as in the above $2n$-vortex case. Fig. 6.13 shows the structure of the forced two-vortex travelling wave. In order to prevent the TW from relaminarizing when reducing the forcing k_z has to be adjusted and ν has to be reduced. But at Reynolds numbers as high as 4000 the forcing can still not be reduced below $f = 5.10^{-3}$ without the decay of the forced TW.

We offer the following explanation for this failure: when the artificial forcing is reduced the 'natural' internal forcing, i.e. the shear due to laminar Hagen-Poiseuille profile, has to be increased and has to take over the driving of the TW-structure. For our forced two-vortex flow a driving across the pipe diameter was necessary but this is not provided by the Hagen-Poiseuille shear profile.

So our list of TWs does not include a state of C_1- symmetry to which the mode with strongest linear transient growth belongs [5]. This should have implications for lowest-dimensional

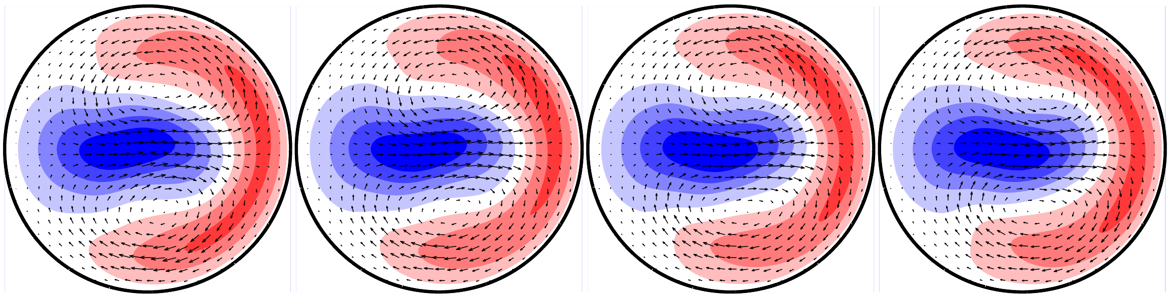

Figure 6.13: *Forced* travelling two-vortex wave at $Re = 640, f = 0.05, k_z = 2$. The frames are cross sections at different downstream positions separated by $\Delta z = L/6$. Only half a period is shown: the last frame is the same as the first one up to a reflection at the horizontal diameter. Upon a reduction of the force to zero the forced travelling wave dies to the laminar Hagen-Poiseuille flow, even for Re of up to 4000.

model building [6, 12] where linear arguments might have led to an overemphasis of the mode with C_1-symmetry.

In an asymptotic analysis by Smith & Bodonyi [77] neutral modes were identified in high Reynolds number pipe flow which is subject to small but finite 3-d disturbances and modeled with a nonlinear critical layer. These modes exist for azimuthal wavenumber $n = 1$ but not for $n > 1$, which is exactly the other way round as for the above C_n-symmetric travelling waves.

6.5 Search for spiral $2n$-vortex travelling waves

Completely analogous to the construction of the $2n$-vortex travelling waves in the previous section we now go on to what seems to be one of the the next more complicated topology of vortices, spiral travelling waves. We make a low order ansatz for the forced velocity field of a spiral 2n-vortex flow where the vortices are azimuthally rotated when going downstream, which leads to a helical structure. A simple realization of such a (forced) spiral velocity (n,m)-mode which fulfills the various constraints is

$$\mathbf{u}_{n,m}(\mathbf{r}) = \begin{pmatrix} inr^2(r-1)^2 \\ r^2(-3+8r-5r^2) \\ 0 \end{pmatrix} e^{in\phi} e^{imk_z z} + cc\,. \tag{6.11}$$

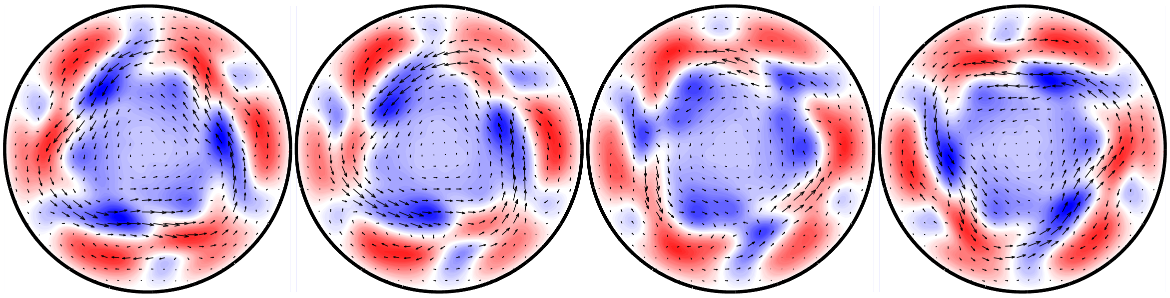

Figure 6.14: *Forced* travelling six-vortex helical wave ($n = 3, m = 1$) at $Re = 1751, f = 0.3, k_z = 2$. The frames are cross sections at different downstream positions separated by $\Delta z = L/6$. Only half a period is shown, here the first and last frame are connected by an axial rotation of $\pi/3$. Upon a reduction of the force to zero the forced spiral travelling wave dies to the laminar Hagen-Poiseuille flow, even for Reynolds numbers of up to 4000.

In the appropriate spiral coordinates we again have a 2c-2d velocity field. The corresponding regular volume forcing that follows from the Poisson equation (6.4) is

$$\begin{aligned} &\mathbf{F}^{n,m}(\mathbf{r}) = \\ &= f\nu \begin{pmatrix} in(n^2 - 9 + r(32 - 2n^2) + r^2(n^2 - 25) + m^2 k_z^2 r^2 (r-1)^2) \\ 9 - n^2 + r(4n^2 - 64) + r^2(75 - 3n^2) + m^2 k_z^2 r^2(-5r^2 + 8r - 3) \\ 0 \end{pmatrix} \times \\ &\qquad \times e^{in\phi} e^{imk_z z} + cc \,. \end{aligned} \tag{6.12}$$

We test pipe flow for the existence of a ($n = 3, m = 1$)-spiral travelling wave. At $Re = 750$, $f = 0.4$ and $k_z = 2$ the flow dynamically relaxes onto a forced 3-d TW. The spatial symmetry of the bifurcated state is helical,

$$\mathbf{u}(r, \phi, z) = \mathbf{u}(r, \phi + \frac{\pi}{n}, z + \frac{L}{2}) \,. \tag{6.13}$$

The structure of the forced flow can be seen in Fig. 6.14. A strong mean azimuthal flow is induced by this configuration of vortices. It is possible to continue the state down to $f = 5 \times 10^{-3}$ but a further reduction of the forcing leads to a reconnection with the laminar profile, even upon extensively optimizing Re and L. So far, no spiral travelling wave can be identified as solution to the unforced pipe flow problem below $Re = 4000$. This seems to be in agreement with the findings of Barnes & Kerswell [3] whose TWs in the rotating pipe presumably also excite a non-vanishing mean azimuthal flow, which does not seem to be easily supported by unforced Hagen-Poiseuille pipe dynamics. This has not been obvious a priori, as, for instance, in Taylor-Couette flow secondary states exist that induce a mean flux in the ’neutral’ spanwise direction (e.g. spiral vortices). Stable spiral waves have been searched for numerically by Landman [44] but without success whereas experimentally helical wave-like structures have been reported from the central part of the upstream region of a turbulent puff [2, 19].

6.6 Conclusions

The existence of exact coherent states in pipe flow has been an object of speculation for some time [7, 12, 19] but different earlier attempts to find them numerically have failed [3, 44].

In the present work a whole family of exact coherent states has been identified as nonlinear solutions to the full Navier-Stokes equations for an incompressible fluid. Their structure is dominated by streamwise vortices and is similar to coherent states observed in other shear flows. This underlines the significance of vortex-streak interactions in shear flows and opens alternative routes to modeling and controlling pipe flow.

The numerical task of representing them accurately is considerably more expensive than for stationary states in plane shear flows. About five times more active degrees of freedom are necessary here although full spectral precision has been used. The reason is not obvious as the states do not seem to be of considerably richer structure than those in plane Couette. On the other side, the parametric study is markedly simplified due to the trivial periodicity in azimuthal direction.

Compared to travelling waves in plane Couette flow, which we also investigated in (not presented here), TWs in pipe flow are easier to handle. In plane Couette states have to break the inversion symmetry of the laminar profile to obtain a mean drift velocity in the laboratory system. This leads to a much richer spatial structure which in turn induces numerical difficulties.

Besides the TWs presented here we can expect many other states. Future search for TWs should be based on a further symmetry decomposition of the problem. First of all it would be interesting to look for states that are invariant with respect to a simple reflection symmetry. Numerically imposing this symmetry in advance suppresses the bifurcation to the shift-and-reflect symmetry and along the lines of the above method we expect to find a second family of travelling waves. Further inspiration by the structure of selected linear eigenmodes seems possible. Travelling waves with an additional nodal radius which (streamwise averaged) resemble the modes labeled EV4 in Fig. A.3 and A.4 in Appendix A can be expected. On the assumption that narrower vortices will require stronger driving we anticipate that they will have critical Reynolds numbers higher than the 1250 found for the C_3-symmetric state. States of the present family of C_n-symmetric waves for all $n > 1$ are expected to exist, but with increasing numerical demands on the radial resolution. The scaling of critical Reynolds number and optimal wavelength with n would be of great interest.

In addition there are all the states that bifurcate from the TWs as well as periodic and aperiodic states that bifurcate in further bifurcations. There will be homoclinic and heteroclinic connections between them. All these states together then form a chaotic saddle in phase space that supports the turbulent dynamics. It will be interesting to see to which extend these states can be used to approximate properties of the turbulent flow. Further evidence for this transition scenario will be given in the next chapter.

Travelling waves are steady fields in the comoving frame of reference. Its dynamics at a cross-section of fixed position in the lab frame is, however, far from trivial. Nevertheless, it has a considerably less complexity than a turbulent dynamics at transitional Reynolds numbers. In order to systematically approximate the dynamical properties of the turbulent state within the framework of periodic orbit theory [25] states of more complex dynamics, especially periodic orbits, are still missing. Also, for a clearer manifestation of a temporal regeneration cycle [92] periodic orbits should show the different phases of downstream vortices generating streaks whose instability in turn regenerates the downstream vortices.

We would like to speculate about the possibility that the C_n-symmetric travelling waves restricted to a wedge shaped section of the pipe of angle $2\pi/n$ are homotop to wavy-vortex flow in plane Couette (which in turn is homotop to wavy-vortex flow in Taylor-Couette and plane Poiseuille flow, with no-slip or free-slip boundary conditions). This is motivated by structural similarities of the C_n-symmetric states and wavy-vortex flow: in both flows counter-rotating vortices are aligned in spanwise direction which are again modulated in spanwise direction. This suggests a common ground state for a large fraction of shear flows which would not only be of great interest for a study of the effects of curvature and boundary conditions on the states.

Experimentally, Darbyshire & Mullin [19] observed a 'wave-like flow' triggered in less than 1% of their transition experiments with rather large initial amplitudes. Since they could not determine whether it decayed or not and they did not give a description of the wave structure we can not compare with these findings.

Due to the very low-dimensional unstable manifold of the travelling waves it appears promising to try to stabilize them experimentally. This should be possible with a closed loop control, consisting of real-time monitoring of the velocity field [22], a quickly adjustable volume forcing and any standard method of chaos control [8, 58]. This is assisted by the fact that the growth rate of the linear instabilities of the waves is slow.

Selected results of this chapter have been submitted for publication to Physical Review Letters [35].

7 Transition to turbulence in constant-flux pipe flow

In the present chapter we want to propose that the transition to turbulence in pipe flow is connected with the formation of a chaotic strange saddle (repellor) in phase space. This repellor is a presumably fractal invariant manifold with a complex domain of attraction and with an unstable manifold along which the escape of turbulent trajectories is enabled. It is composed of nonlinear three-dimensional exact coherent states like travelling waves or periodic orbits, and their homoclinic and heteroclinic connections, all of which are expected to be linearly unstable. The first have been identified and analysed in the previous chapter. A turbulent dynamics on the repellor then corresponds to trajectories that are scattered between these states in an irregular, chaotic manner, attracted by their large stable manifolds but then again quickly repelled along their unstable manifolds.

As indicators for this scenario we analyse the sensitive dependence on initial conditions and on parameters, the Lyapunov exponent of the turbulent state, the scaling near the boundary to the turbulent state, and the distribution of turbulent lifetimes. All our findings are consistent with the formation of a strange saddle in phase space.

7.1 Numerical lifetime experiments

Our analysis will be based on the time evolution of initial perturbations in circular pipe flow with periodic boundary conditions in the downstream direction. For an accurate simulation of turbulent dynamics at transitional Reynolds numbers the streamwise periodicity L is set to $10R$ which is about the minimal value that is necessary to justify periodic boundary conditions [28], i.e. for velocity fluctuations to be decorrelated at a streamwise separation of half the pipe length. This is about 2.4 to 4 times the optimal wavelength of a travelling wave, cf. Tab. 6.1. As in the experiments of Darbyshire & Mullin [19] we keep the volume flux constant. This simplifies the analysis as the Reynolds number is constant in time and a possible decay is not connected to a drop in flux, i.e. in Re.

We want to study the dependence of the lifetime of intermittent trajectories on parameters to identify transition thresholds, stability boundaries and the statistical distribution of lifetimes.

In order to do so we first have to discuss our definition of a lifetime experiment, that is, our choice of initial conditions, decay threshold, maximum observation time, and numerical resolution.

Initial conditions

The first question is what type of initial condition should be used. Possible choices are:

- an element of the turbulent state, i.e. a snapshot of a turbulent velocity field. This, however, is not suitable as the turbulent state drifts in phase space as a function of Reynolds number (cf. Fig.7.11 below). Thus a snapshot from the turbulent state at some Reynolds number is no longer a good initial condition at 20% higher or lower Reynolds numbers as the probability for a more or less direct decay is rather high.
- simulation of suction and blowing from the wall. Presumably a good choice and closest to the laboratory experiment but not without problems. Plane Poiseuille flow experiments [61] have shown a nontrivial dependence of the receptivity of a jet disturbance on the jet amplitude: intermediate jet amplitudes did not trigger transition whereas higher and a range of lower amplitudes did. This might be connected to interactions of the near wall and far wall laminar boundary layers with the jet.
- Zikanov's nearly optimal initial condition with a small additional 3-d perturbation. As shown in section 5.2, Zikanov's 2-d mode develops inflection points of the mean profile and becomes linearly unstable with respect to 3-d disturbances which grow and take over to a turbulent dynamics. This streak breakdown mechanism is a smooth and well controlled way into turbulence but it depends too much on a linear process: for different Reynolds numbers the linear transient amplification and thus the maximum linear growth of the 3-d initial disturbance changes considerably which again complicates the comparison for different Reynolds numbers. Here the amplitude of the 2-d mode as well as the amplitude of the 3-d disturbance has to be defined.
- 3-d uncorrelated superposition of all spectral modes. The amplitudes for the real and imaginary part of all velocity coefficients are chosen once by a random process for independent and uniformly distributed random variables over the interval (-1,+1). In comparison to the above initial condition that relies on streak-breakdown, this corresponds to taking only the 3-d disturbance part. Its spatial structure is so rich that the probability to trigger turbulent dynamics is maximal for a wide range of Reynolds numbers.

We decided on the latter type of initial condition. With a fixed structure of variable amplitude a one dimensional cut through the space of all initial conditions is obtained.

For a measurement of statistical properties of the turbulent state (such as escape rates and Lyapunov exponents) it should not matter which type of initial condition has been used as long as transition to the turbulent state has been triggered: due to positive Lyapunov exponents (see below) the trajectory quickly 'forgets' which part of phase space it came from. Furthermore, it seems to be evident that they all approach the same turbulent state, regardless of the type of disturbance. This is confirmed experimentally where, for instance, wall-normal and azimuthal jets or a combination of jets and suction lead to very similar results [19]. Rubin *et al.* [69] also report on the independence of the downstream structures of transitional flow of the method of production.

Disturbance amplitude

We define the amplitude of an initial disturbance as its kinetic energy in units of the energy of the laminar profile $\mathbf{u}^{(0)}$,

$$\frac{\int dV(\mathbf{u}-\mathbf{u}^{(0)})^2}{\int dV(\mathbf{u}^{(0)})^2}\,. \tag{7.1}$$

This definition trivially depends on the Reynolds number - various alternative choices are possible and have been employed in laboratory and numerical experiments, for a discussion see [88].

Decay threshold

We define a turbulent lifetime beginning from the time integration of the initial condition up to the time when the energy content in the streamwise modulated part of the velocity field, E_{3d}, has decreased below a threshold. E_{3D} is defined as

$$E_{3d}=\frac{\sum_{m\neq 0}\int dV|\mathbf{u}_{n,m}(r)|^2}{\int dV(\mathbf{u}^{(0)})^2}\,. \tag{7.2}$$

The energy content of the streamwise invariant part of the flow may still be fairly large at that stage. E_{3d} has shown to be a much more sensitive measure for turbulence intensity than the total energy. In section 5.2 we have seen that 3c-2d streamwise invariant velocity fields ($E_{3d}=0$) can show oscillations and may have long transients although they are known to be about to decay. By analysing many turbulent trajectories we realized that none of them dropped below $E_{3d}=10^{-3}$ without decay. So we decided on a decay threshold of $E_{3d}=10^{-4}$, which is two orders of magnitude below the turbulent mean. (For the turbulent mean and fluctuations in the total energy and in E_{3d} see Fig. 7.11.)

Maximum lifetime

We extended our numerical investigations to dimensionless times of 2000 or more, far exceeding the maximal observation time of the experiments by Darbyshire & Mullin [19] ($T_{\text{max}}\approx L/D$=100) and exceeding the values accessible in the longest currently available pipe flow setup, which to our knowledge is the one at the J.M. Burgers Centre, Delft University of Technology. Its total length is 32m and its diameter is 40mm, i.e. $T_{\text{max}}\approx L/D$ = 800, but the test section for the measurement is only a fraction of it [23] [1].

---

[1] Here we assumed the turbulent puff's leading laminar-turbulent interface to travel at about the bulk velocity, as discussed in chapter 3.

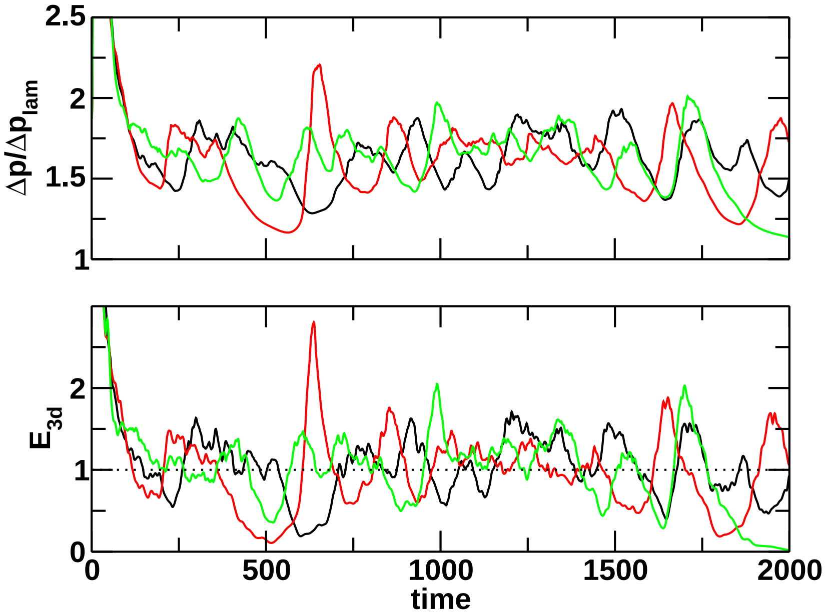

Figure 7.1: Typical turbulent time evolution of initial perturbations in pipe flow at $Re = 2100$. The initial energies are chosen high above the turbulent mean and the trajectories relax onto the turbulent state within approximately 200 time units. Three initial disturbances of same spatial structure but slightly different amplitudes have been chosen. The top frame shows the total pressure drop needed to sustain the volume flux at its laminar value. The bottom frame shows the kinetic energy of the streamwise modulated part of the velocity field, E_{3d}, normalized by its turbulent mean as a measure of the velocity fluctuations. It is strongly correlated to the pressure drop. Within statistical fluctuations the averages of the turbulent dynamics are the same for all trajectories including the green trajectory which just happens to decay near $t = 2000$.

Numerical resolution

If not stated otherwise the spatial resolution used for the results presented in this chapter is $|n|/16 + |m|/14 \leq 1$, i.e. up to 33 Fourier-modes in azimuthal direction and 29 Fourier-modes in downstream direction, and 50 Legendre polynomials radially. It is a compromise between maximum resolution, maximum cut-off lifetime and largest statistics. It is justified by a comparison with lower and higher resolutions which give no qualitatively different results, as discussed in section 5.3.2. This resolution is an order of magnitude higher than for the travelling waves in the previous chapter as the algorithmic demands on the solution of initial-boundary problems are considerably lower.

The typical time evolution of turbulent trajectories in our lifetime experiments is shown in Fig. 7.1. Immediately after onset high dimensional dynamics on many temporal and spatial scales is observed.

7.1.1 Sensitivity on initial conditions and on parameters

In this section we present extensive measurements of lifetimes of turbulent trajectories for various disturbance amplitudes and Reynolds numbers. We want to give evidence that the overall features of our results are rather robust with respect to the spatial resolution and, therefore, present lifetime diagrams are based on two different types of simulations.

First we show preliminary calculations that were considerably lower resolved than all the following ones. Here a spatial resolution of $|n|/10 + |m|/10 \leq 1$, i.e. up to 21 modes in azimuthal and streamwise directions, and 40 Legendre polynomials in radial direction has been used, which is close to the resolution of the travelling waves in the previous chapter. The streamwise wavelength has been restricted to $L/R = 2\pi$. Fig. 7.2 shows the turbulent lifetime of trajectories as a function of Reynolds number and initial disturbance amplitude for these runs. In spite of these limitations various conclusions can be drawn from these lifetime experiments that have all been validated by higher quality numerical simulations which are presented in Fig. 7.3. Those and all the following are based on the resolution with $|n|/16 + |m|/14 \leq 1$ and 50 Legendre polynomials for a length $L/R = 10$.

The turbulent lifetimes in Fig. 7.2 and Fig. 7.3 show large fluctuations that imply an extreme sensitivity with respect to small changes in initial conditions and parameters. A complicated, fuzzy stability boundary between decaying and sustained turbulent solutions is observed. First long-living solutions are identified at around Re=1800. A more or less complex network of states in phase space must exist at this stage and be sufficiently entwined to enable repeated scattering without decay. From $Re \lesssim 2000$ on a large fraction of initial conditions trigger long-living turbulence that reach the cut-off lifetime of t=2000. We observe a double threshold to turbulence, that is, in order for a transition to take place a sufficient Reynolds number as well as a sufficient amplitude is needed. The minimum amplitude to trigger a long living turbulent dynamics decreases with Reynolds number.

All these findings are in agreement with laboratory experiments by Darbyshire & Mullin [19], which in parts have been presented in chapter 2, as well as with transition scenarios in other shear flows that are not dominated by linear instabilities [9, 33, 73].

Scaling near the transition boundary

Let us investigate the situation at $Re = 2000$ in more detail. The parameter region inside the red rectangle in the lower left graph ($Re = 2000$) in Fig. 7.3 is successively magnified by orders of magnitude in Fig. 7.4. Two separate regions of different behaviour can clearly be distinguished, above and below a critical disturbance amplitude. Below the critical amplitude lifetimes vary smoothly. Up to a certain disturbance amplitude the lifetime grows linearly with the amplitude as the dynamics is dominated by linear terms. Then nonlinear dynamics

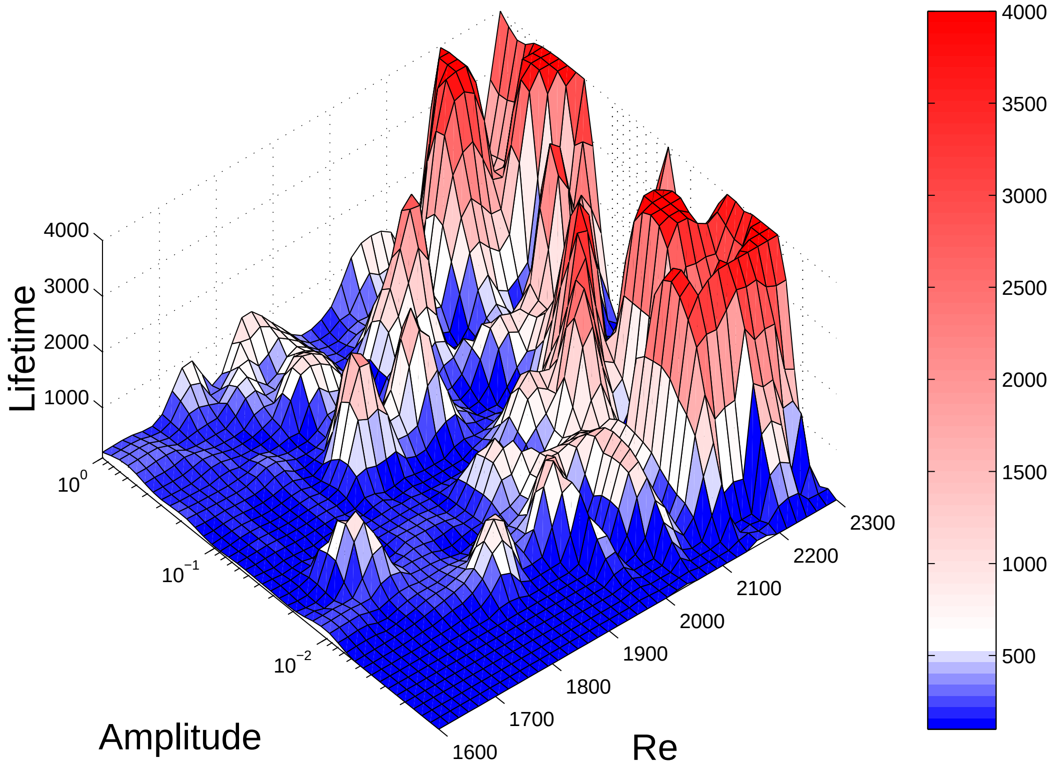

Figure 7.2: Turbulent lifetime as a function of Reynolds number and of initial disturbance amplitude. Simulations were done with a reduced numerical resolution. The color-coding separates runs that would have decayed within usual experimentally accessible lifetimes and those that would have appeared as sustained. A grid of 15×15 parameter points underlies this surface plot.

quickly accelerates the increase in lifetime. By further increasing the amplitude the dynamics approaches the stable manifold of the repellor and long lifetimes of the order of 1000 are observed. This critical amplitude region is magnified in the right graph in Fig. 7.4. Above the critical amplitude the lifetime varies irregularly and depends very sensitively on the initial amplitude. Supported by numerical simulations [73] as well as by models for plane shear flow [26] even a fractal behaviour could be suggested. The sensitivity of this flow is enhanced by the ability to amplify small perturbations through non-normal amplification.

Energy traces of selected trajectories from these lifetime experiments at $Re = 2000$ are shown in the following. Fig. 7.5 shows trajectories from the 'smooth' side that are very close to the transition boundary. As the initial amplitude is slightly increased, with relative changes of approximately 10^{-4}, the trajectory lives longer and undergoes more and more nonlinear regeneration cycles before it finally decays towards the laminar state.

The non-monotonous but still smooth dependence of lifetime on the initial amplitude close to the turbulence transition boundary at $Re = 2000$ is shown in Fig. 7.6. As the boundary

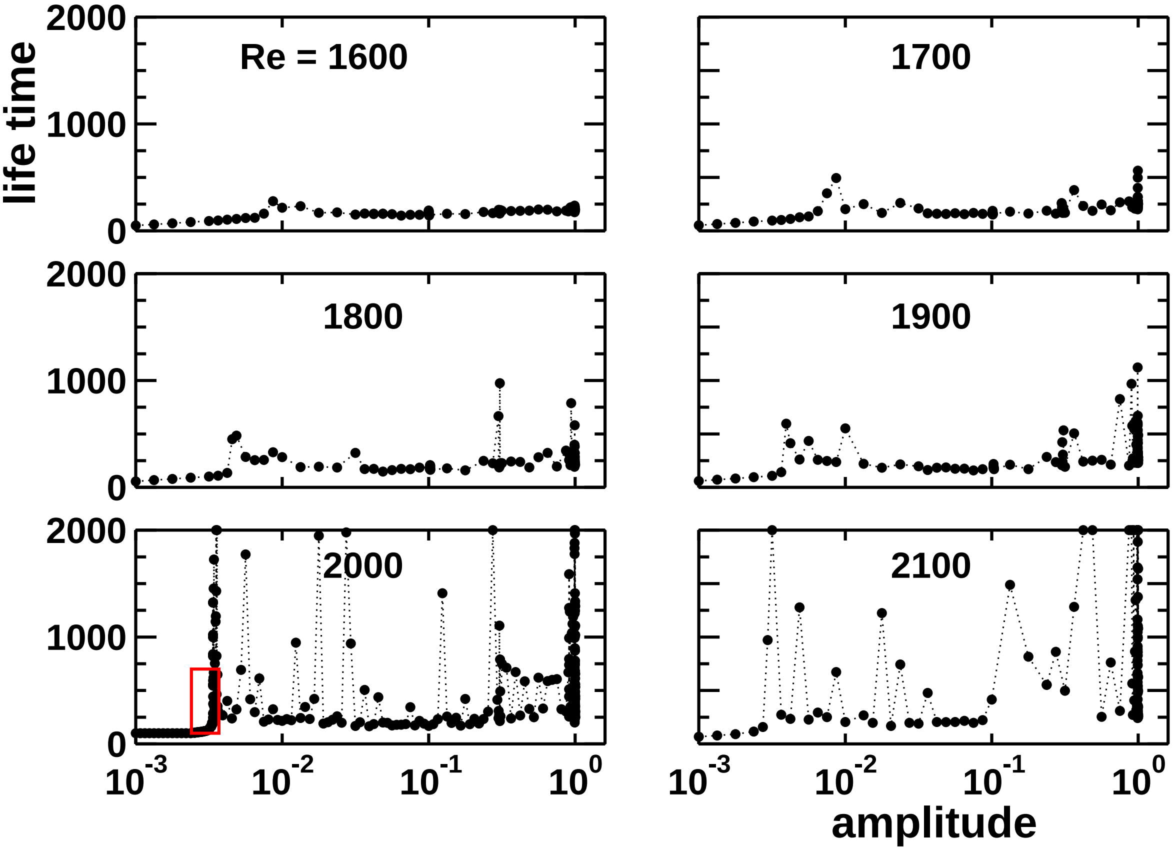

Figure 7.3: Turbulent lifetime vs. perturbation amplitude for different Reynolds numbers. For all Reynolds numbers a smooth region with short-lived states can be observed for small amplitudes. With increasing Reynolds number this region is followed by a ragged region of highly fluctuating lifetimes. The threshold amplitude that divides the two regions decreases with Reynolds number and is shown in Table 7.1 The red marked parameter range at $Re = 2000$ is further investigated in the following. The data obtained at amplitude ≈ 1 are analysed statistically in section 7.1.2.

is approached the amplitude and frequency of oscillations in lifetime as functions of parameters quickly increase. This is a footprint of the complex structure of the stability boundary between decaying and sustained solutions, and a hint on the folding of the stable manifold of the repellor.

With a re-definition of the disturbance amplitude based on the L_2-norm predictions exist for an algebraic scaling for the minimal disturbance amplitude that triggers transition as Re^{γ} with an exponent $\gamma < -1$. However, according to [88], laboratory experiments only give rough estimates of $-1.8 < \gamma < -1.15$ for the investigations of Darbyshire & Mullin [19] and $-2 < \gamma < 1$ for Draad & Nieuwstadt's experiments [23]. It is of course not clear whether the different injected perturbations really have maximal efficiency in triggering turbulence.

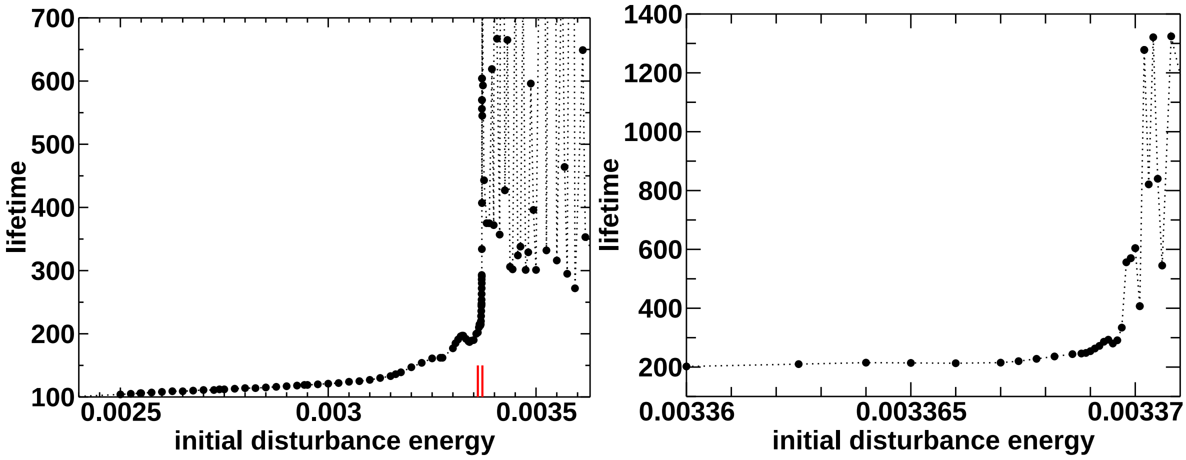

Figure 7.4: Successive magnifications of the lifetime diagram at the transition boundary at $Re = 2000$. The left graph is a magnification of the red marked parameter region in Fig. 7.3, the right graph is a further magnification of the red marked tiny parameter range in the left graph. The lifetimes do not simply increase like a logarithm when approaching the boundary as might be expected at smooth boundaries of simple basins of attraction (see text). Instead, oscillations in lifetime of increasing amplitude and frequency are observed.

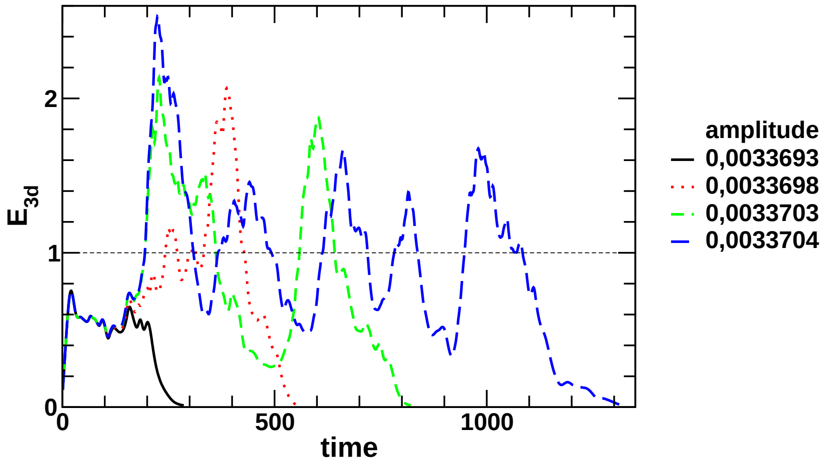

Figure 7.5: Energy measure of trajectories in units of the turbulent mean as a function of time at $Re = 2000$ when approaching the stability boundary from the 'smooth' side. These trajectories correspond to data points in Fig. 7.3 and 7.4.

We give the data on the lowest perturbation amplitude where a first maximum in lifetime is observed in Tab. 7.1 but we do not dare to extrapolate on an asymptotic value for the scaling of the transition threshold with Re for $Re \to \infty$ as we know our limitations in Reynolds number.

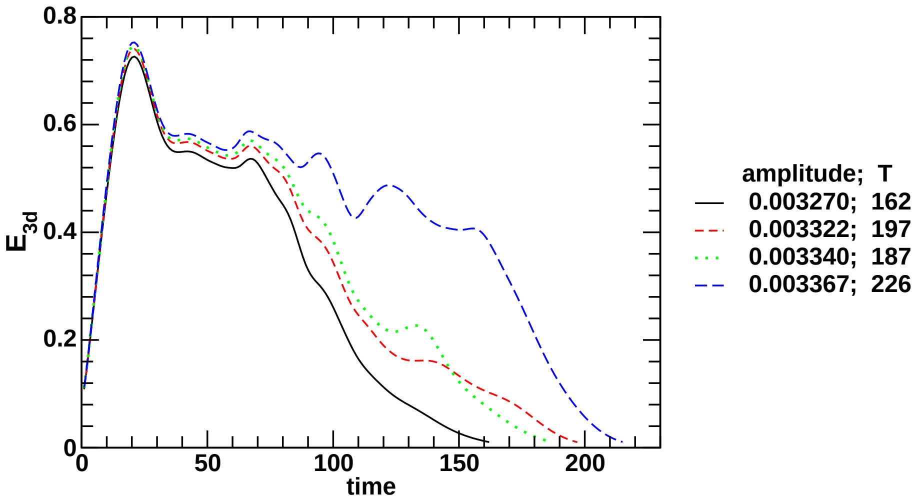

Figure 7.6: Non-monotonous but still smooth dependence of life time on the initial amplitude close to the turbulence transition boundary at $Re = 2000$. These trajectories correspond to data points in Fig. 7.3 and 7.4.

Parameter dependence of the turbulent lifetime

We observe sensitivity not only with respect to the initial disturbance but also with respect to Reynolds number and other external parameters. The turbulent lifetime as a function of the Reynolds number at a fixed initial disturbance amplitude $E(t{=}0){=}0.00327$ is shown in Fig. 7.7. Again two parameter regimes can be identified. Below a transition boundary the dependence of lifetime on Reynolds number is smooth, whereas it is irregular above. The magnification of the neighbourhood of the boundary in the right graph in Fig. 7.7 further exemplifies the extreme parameter sensitivity above the threshold and the increasingly non-trivial dependence when approaching the boundary. A relative change of 10^{-5} in Re can already lead up to a factor of four in the change in lifetime. Again, no simple scaling can be observed.

But what scaling could have been expected when approaching the transition boundary from the ’smooth’ side? For the most simple dynamical systems, which show smooth and simple boundaries in parameter space, with smooth seperatrices in phase space that correspond to simple configurations of the stable and unstable manifolds, a logarithmic behaviour could be expected. A simple saddle fixed point as well as the 2-d Henon-map, for instance, show this

Reynolds number	1600	1700	1800	1900	2000	2100
amplitude/10^{-3}	8.66	8.67	4.56	3.95	3.37	3.16

Table 7.1: Lowest perturbation amplitude where a first maximum in lifetime is observed. The data have been extracted from Fig. 7.3.

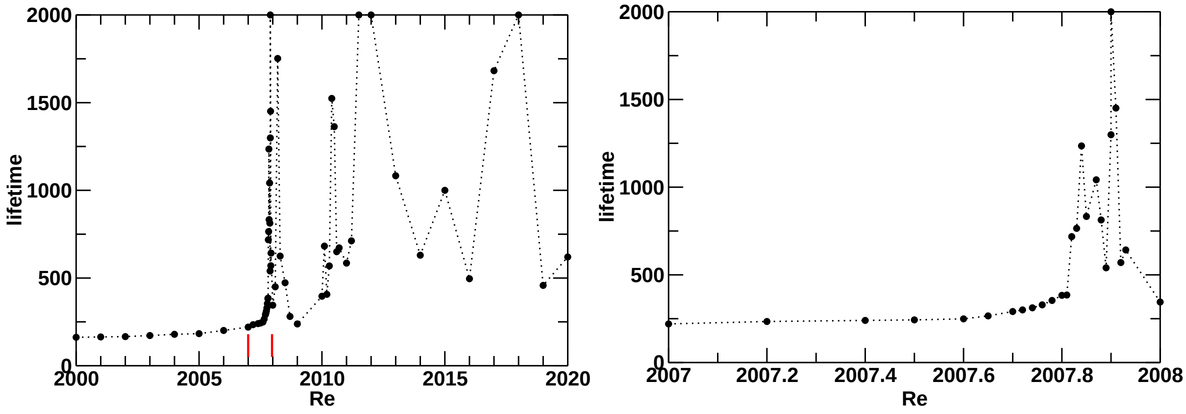

Figure 7.7: A complementary approach to the turbulence transition boundary: turbulent lifetime vs. Reynolds number at a fixed initial disturbance amplitude $E(t{=}0){=}0.00327$. The parameter range adjacent to the transition boundary, marked by red lines, is magnified in the right graph .

logarithmic scaling behaviour, for instance. It is also possible to have a smooth algebraic increase in lifetime when approaching a transition boundary, but as soon as the boundary structure becomes too complex the stable and unstable manifolds are twisted in an irregular manner and a simple scaling can no longer be observed. All this is illustrated in a low-dimensional example that already exhibits logarithmic, algebraic as well as irregular scaling, depending on the direction of approach to the transition boundary. This example will be presented in Appendix C.

7.1.2 Exponential distribution of lifetimes

As explained in the last section, the turbulent lifetimes show an extreme sensitivity with respect to changes in parameters, which leads to a complicated, fuzzy stability boundary between decaying and sustained turbulent solutions. This calls for a statistical description. More than 50 trajectories have been analysed each for transitional Reynolds numbers from 1600 up to 2200. Only very high initial amplitudes of ≈ 1 have been chosen for this task and their lifetimes have been included in Fig. 7.3 in the previous section 7.1.1. A total real time of 3 CPU-years on 2.2 GHz Pentium 4/Xeon processors has been necessary to obtain these statistics. The resulting probability $p(t)$ for a single trajectory to stay turbulent for a certain time is shown in Fig. 7.8. Despite the large fluctuations an exponential dependence can be identified, which we interpret as a constant escape rate, ϵ, which is a major characteristic of a chaotic saddle in phase space. Neglecting the initial relaxation time to the repellor, the probability to stay turbulent is $p(t) = \epsilon e^{-\epsilon t}$. The median lifetime τ, where $p(\tau) = 0.5$, as a function of Reynolds number is extracted in Fig. 7.9. Below $Re = 1800$ the increase is mainly due to non-normal transient linear dynamics. When the Reynolds number

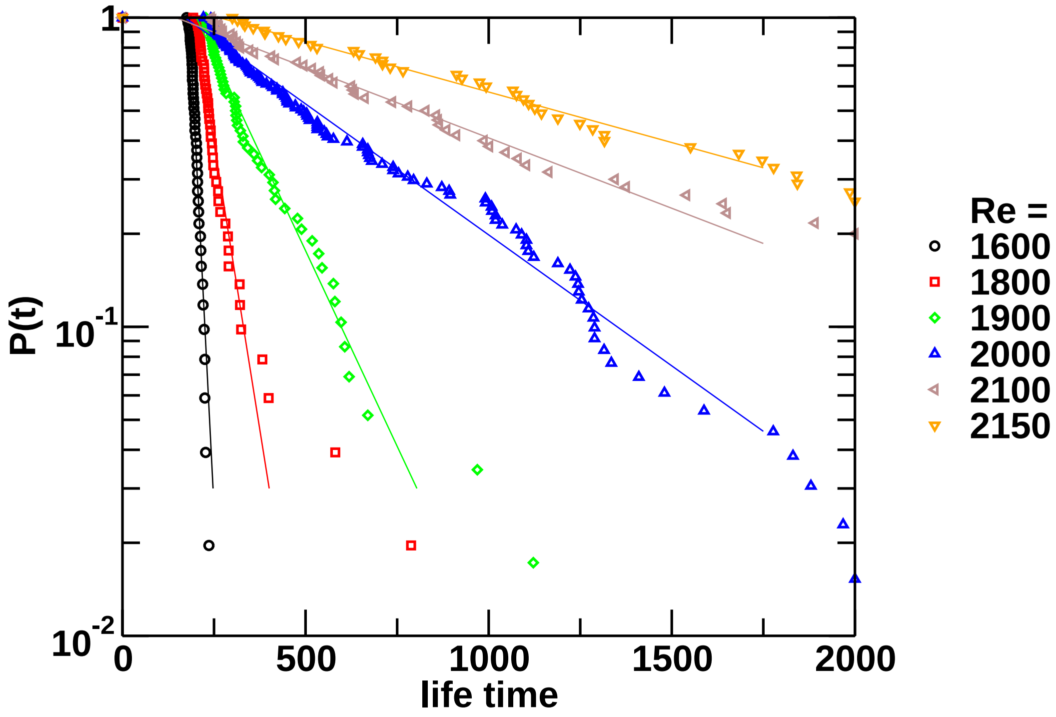

Figure 7.8: Distribution of turbulent lifetimes for different transitional Reynolds numbers. The probability for a single trajectory to still be turbulent after a certain time is displayed. Six Reynolds numbers are shown from 1600 to 2150. Between 50 and 100 trajectories have been evaluated per Reynolds number. The distributions are in agreement with exponential distributions though the fluctuations are strong, especially in the tails.

is increased above $Re = 2000$ the median of the turbulent lifetimes as well as the fluctuations raise rapidly until the median reaches the cut-off lifetime of 2000 at $Re \approx 2200$. From the exponential distribution it follows that the rms fluctuations increase linearly with the median.

The analysis of transient turbulent trajectories for $Re < 2200$ suggests that at the end of each individual nonlinear regeneration cycle there is a certain probability to decay to the laminar state. The conclusion from the exponential distribution of lifetimes is that this probability remains constant during the evolution, independent of the 'age' of the trajectory.

Exponential distributions of lifetime have been identified before in plane Couette flow, experimentally [9] and numerically [74], as well as in Taylor-Couette flow [27]. This is evidence for a further generic feature of transition in shear flows that are not dominated by linear instabilities.

We see that no sharp, reproducible critical Reynolds number for the transition to turbulence in pipe flow exists. But what is the transitional Reynolds number in pipe flow? First of all, how can we define it? Accepting the exponential distribution of lifetimes any defini-

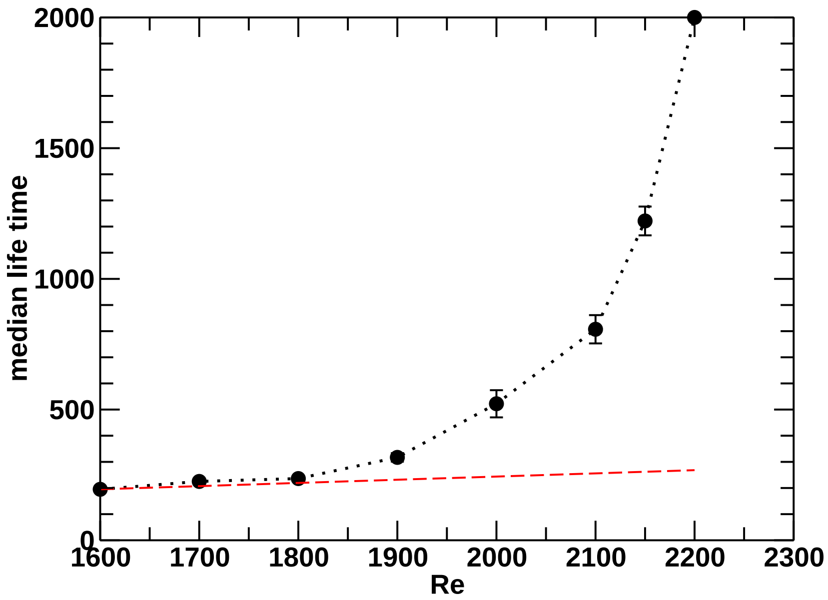

Figure 7.9: The median of the turbulent lifetimes as a function of Reynolds number. The median and the fluctuations increase rapidly with Reynolds number until the median reaches the cut-off lifetime of 2000. The error bars indicate the statistical uncertainty of the median. The rms fluctuations about the mean lifetime are expected to grow linearly with the median and are not displayed. The straight dashed line marks the linear increase in lifetime expected due to purely non-normal linear dynamics.

tion of a transitional Reynolds number, Re_{tr}, must be probabilistic. It might be based on a certain value of the median lifetime or, equivalently, on the escape rate, which calls for measurements at different downstream distances. An alternative would be to extrapolate to the Reynolds number where the median lifetime seems to diverge, which, however, is much more problematic since the behaviour in this limit is not yet clear.

The energy Reynolds number, Re_E, below which all trajectories monotonously decay, is a very conservative approximation to the transitional Reynolds number in shear flows. The Reynolds number where the first nonlinear exact coherent state (travelling wave) is observed, Re_{TW}, is a much better approximation, $Re_E (= 81.5) < Re_{TW} (= 1250) < Re_{tr} \approx$ 2000, but it is still a considerable underestimation.

7.2 Lyapunov exponents

It is our aim here to analyse Lyapunov exponents in order to quantify the sensitive dependence on initial conditions and the spatially chaotic motion.

The largest Lyapunov exponent λ along a trajectory $\mathbf{u}(t), t \in [0, T)$,

$$\lambda = \lim_{||\delta u(0)|| \to 0} \lim_{T \to \infty} \log \frac{||\delta u(T)||}{||\delta u(0)||}, \tag{7.3}$$

governs the mean exponential escape $\propto e^{\lambda t}$ of closely neighbouring trajectories in phase space. For the norm in the definition of λ we take the L_2 norm of the velocity coefficients. We approximate λ numerically by ensembles of finite-time ($T = 200$) Lyapunov exponents, which have been extracted from the integration of series of closely neighboured pairs of turbulent trajectories. We measure the distance of the trajectories every 200 time steps and reduce it back to $||\delta u|| = 10^{-9}$. This time interval appears to be appropriate as up to this time no nonlinear effects take over and the escape is still exponential. Taking too short time intervals non-normal effects dominate the time evolution. We have to omit an initial and final time interval of 200 time steps where the relaxation on to and the escape from the repellor give too large and too small values, respectively, for the Lyapunov exponent of the turbulent dynamics on the repellor. Due to the large fluctuations we have to evaluate a total of 10^4 time units each, taking the center part of the trajectories only, in order to obtain sufficiently reliable results. This makes it difficult to acquire a sufficient statistics below $Re = 2000$. As shown in Fig. 7.10 the largest Lyapunov exponent increases with Reynolds number, but not as quickly as the lifetimes. Its typical value is about 6.5×10^{-2} at transitional Reynolds numbers. This corresponds to an amplification factor of the order of 10^6 over 200 time units which is a typical time interval for a regeneration cycle. The short-time Lyapunov exponents are strongly correlated with the large energy fluctuations shown in Fig. 7.1. When new large scale structures are generated the energy grows strongly and the Lyapunov exponent increases. Towards the end of a nonlinear regeneration cycle the energy goes down and the Lyapunov exponent decreases as well. Therefore, the fluctuations in the exponent are large and long statistics over many turbulent trajectories have to be gathered. The coupling between energy and Lyapunov exponent is also reflected in their very similar slope as functions of Reynolds number, see Fig. 7.10 and 7.11, where the latter shows the slow drift in the turbulent mean of the total energy and in E_{3d} together with their rms-fluctuations. The positive Lyapunov exponent also measures the mean loss in predictability with time. The uncertainty in the state doubles all $\ln(2)/\lambda \approx 10$ time units at transitional Reynolds numbers.

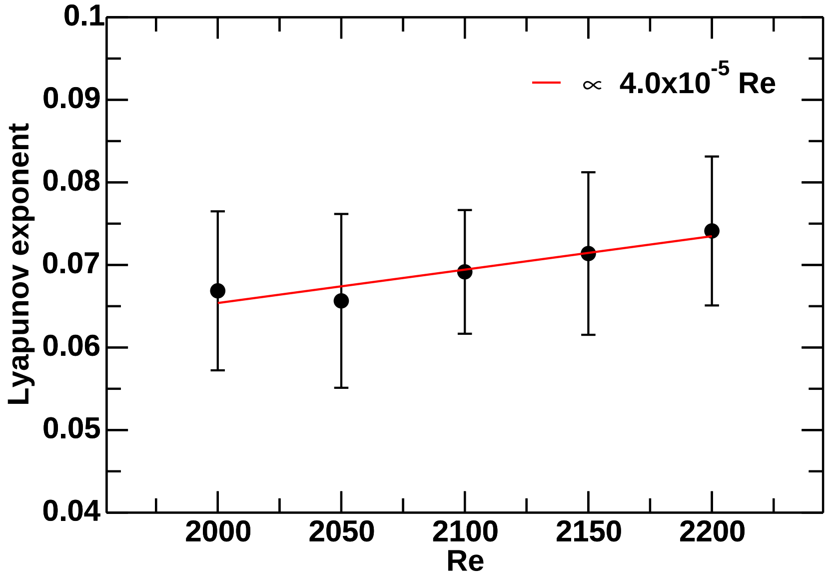

Figure 7.10: Largest Lyapunov exponent of the turbulent state and rms fluctuations as a function of Reynolds number.

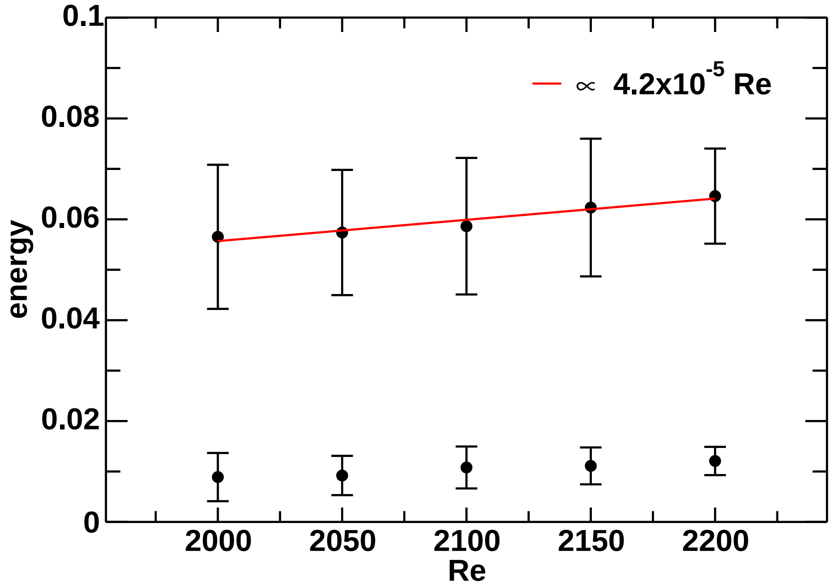

Figure 7.11: Turbulent mean of the total kinetic energy (upper data) and E_{3d} (lower data) together with rms fluctuations as a function of Reynolds number. Both the energy and the Lyapunov exponent in Fig. 7.10 increase with a similar slope.

7.3 Conclusions

In this chapter we investigated in turbulent trajectories that were triggered by finite amplitude disturbances at Reynolds numbers between 1600 and 2200. For Reynolds numbers above 1800 and a disturbance above a threshold amplitude we observe strong sensitivity on initial conditions as well as on parameters which results in large fluctuations in turbulent lifetimes. The regions of quickly decaying and long-living trajectories are separated by complicated, fuzzy stability borders, which might have fractal properties. Lifetime experiments reveal an exponential distribution which suggests a constant escape rate from the turbulent state. These findings strongly suggest the existence of a chaotic repellor which supports the turbulent dynamics. Above Re=2100 lifetimes quickly reach the maximum observation time of 2000. It might even be the case that the escape routes from the repellor are closed and the repellor is turned into a strange attractor at a finite Reynolds number.

We give evidence that the above results are not numerical artefacts of low numerical resolution or of periodic boundary conditions of a too short pipe by successfully comparing results for two spatial resolutions and two pipe lengths.

The prediction of an exponential distribution of lifetimes should be accessible to experimental investigations provided that the observation time is of the order of at least 1000 units. Repeated measurements with similar perturbations are necessary in order to obtain the probability to find a turbulent state that exists at least up to time t. This is a property of the turbulent state in the transition region and can be studied by sampling different initial conditions. Exact reproduction of an initial condition is not critical here since all initial conditions relax to the same turbulent state. The mechanism studied here, the formation of a chaotic saddle, is fairly independent of the boundary conditions, but the quantitative characteristics may depend on it. Whereas in laboratory experiments turbulent spots evolve as slugs or puffs we numerically simulate only their turbulent core region, modelled with periodic boundary conditions in streamwise direction. It will be interesting to see whether this will affect the lifetimes or their distribution. In principle, the detailed analysis of the distribution of lifetimes is a task which is (still) much better suited for experiments than for numerics: it is not necessary to prepare the initial disturbance with highest precision, and the experimental observation time is of the order of 1 minute for the run and at most 30 minutes for the water to come to rest in the head-tank, whereas the numerical calculation of a single trajectory takes up to 10 days on a 2.2 GHz Pentium IV processor. Sensitivity measurements on the other hand are much better suited for numerical investigations due to the high demands on the accuracy of the initial flow state for both the laminar profile and the disturbance. But inspite of these and further differences between numerics and experiment listed in Tab. 7.2 the agreement in key features of the results is notably high.

	laboratory experiment	numerical simulation
axial length $[R]$	puff, slug $\gtrsim 60$	10
laminar profile	$90-95\%$ developed	100% developed
type of initial disturbance	single jet / six jets	uncorrelated
relative error in initial disturbance	$5-10\%$	10^{-12}
relative error in Reynolds number	$\lesssim 1\%$	10^{-12}
maximal observation time [D/U]	100	2000
real time / run	60s + 30min	12h$\ldots10$d

Table 7.2: Differences between laboratory and numerical turbulence transtion experiments

The experimental uncertainty in a suction/blowing experiment seems to be of the order of at least 5%. With a Lyapunov exponent of 0.07 the flow field cannot be controlled for more than about 40 time units. If the disturbance develops into a localized turbulent patch (puff or slug, see chapter 3) the envelope of the patch might be under control for much larger times. These large scale patterns are beyond the scope of the present analysis.

When approaching the transition boundary no simple scaling can be observed. A simple example in Appendix C shows that this is not necessarily due to the high dimensionality of the problem but rather a hint on the complex boundary structure where the stable and unstable manifolds are twisted in a complicated, irregular manner.

All observations are in agreement with pipe flow experiments as well as with observations in plane shear flows and confirm the universal character of the turbulence transition scenario in shear flows that are not governed by linear instabilities:
First unstable exact coherent states appear in phase space below transitional Reynolds numbers. With increasing Re the number of coherent states like TWs and periodic orbits is expected to grow fast. Together with their growing number of homoclinic and heteroclinic connections they span a complex network, a chaotic repellor, which is then able to support a turbulent dynamics for a long time.

Appendix A Eigenvalue analysis

To verify the spectral accuracy of our code we here present tables of eigenvalues to the linearized Navier-Stokes equations at $Re = 3000$. To identify the spatial structure of the least stable linear modes in pipe flow visualizations of selected eigenfunctions are shown.

A.1 Eigenvalues

Only those leading digits of the eigenvalues are given that coincide with literature values [48]. In this way we get a lower limit for our numerical accuracy of the linearized problem. Note that apart from the (n=0, m=0)-mode all eigenvalues come in pairs (real and twice degenerate for m=0, complex conjugate else).

Eigenvalues are reproduced with spectral accuracy of up to 12 decimal places with 64 Legendre polynomials used for the radial discretization (see Tab. A.1, A.2, A.3). There are two factors limiting the accuracy: for the first leading eigenvalues the accuracy is mainly limited by the finite number of digits available in double precision arithmetic whereas for higher eigenvalues it is mainly limited by the finite spectral resolution.

Table A.1 gives the eigenvalues for the streamwise and azimuthally invariant modes. The first column shows the eigenvalues for the constant-pressure-drop calculation, the second column is for the constant-flux case. Fixed volume flux changes the eigenvalue spectrum of the (0,0)-mode only. In this case all eigenfunctions with nonvanishing axial component are affected and only those. The eigenvalue of the least stable eigenfunction is changed to zero, for instance. This is because it only consists of an axial component which is purely parabolic, so it is immediately absorbed by a change in the axial pressure drop. For the case of fixed volume flux we do not have literature data, and we have chosen to show the first 12 leading digits as we expect about the same accuracy as in the unconstrained case.

	n=0, m=0; $\Delta p/L$ =const.	n=0, m=0; flux=const.
1	-0.001927728654	0.000000000000
2	-0.004893990214	-0.004893990214
3	-0.0101570874478	-0.008791538809
4	-0.01640615210723	-0.016406152107
5	-0.0249623355969	-0.023616666456
6	-0.034499817965	-0.034499817965
7	-0.0463467614754	-0.045006903098
8	-0.059173588937	-0.059173588937
9	-0.07431076787255	-0.072973397694
10	-0.0904272180909	-0.090427218091
11	-0.1088544509774	-0.107518373150
12	-0.1282606350342	-0.128260635034
13	-0.1499778428393	-0.148642526686
14	-0.1726738136706	-0.172673813671
15	-0.1976809565519	-0.196346121179
16	-0.2236667425409	-0.223666742541
17	-0.2519637982613	-0.250629298821
18	-0.2812394159789	-0.281239415979
19	-0.3128263711585	-0.311492098465
20	-0.3453918309236	-0.345391830924

Table A.1: Eigenvalues for the n=0, m=0 mode. The first column gives the values for the unconstrained problem. The second column shows the eigenvalues for the system with fixed volume flux.

	n=1, m=0	n=2, m=0	n=3, m=0
1	-0.00489399021	-0.008791538	-0.0135688219
2	-0.0087915388	-0.0135688219	-0.0191943136
3	-0.0164061521	-0.0236166663	-0.03175919084
4	-0.0236166663	-0.03175919085	-0.040809265355
5	-0.03449981796	-0.04500690295	-0.0564651499
6	-0.045006902955	-0.05646514994	-0.06885660345
7	-0.059173588937	-0.0729733963	-0.087733618
8	-0.072973396381	-0.08773361808	-0.10344075328
9	-0.090427218091	-0.1075183721	-0.1255751331
10	-0.107518372097	-0.12557513314	-0.14458704546
11	-0.128260635034	-0.1486425215	-0.1699932252
12	-0.148642521512	-0.16999322529	-0.19230443298
13	-0.1726738136	-0.19634611723	-0.2209893628
14	-0.196346117238	-0.22098936279	-0.2465967917
15	-0.22366674254	-0.2506292846	-0.278564248
16	-0.250629284603	-0.27856424829	-0.3074660355
17	-0.281239415979	-0.3114920878	-0.342718253
18	-0.311492087829	-0.34271825329	-0.37491320196
19	-0.345391830923	-0.3789345626	-0.4134515895
20	-0.378934562605	-0.41345158953	-0.4489388946

Table A.2: Eigenvalues for streamwise wavenumber m=0

	n=0, m=1		n=1, m=1	
1	-0.0519731112828	+ i 0.9483602220505	-0.0412756447	+ i 0.9114655676
2	-0.0519731232053	+ i 0.948360198487	-0.06161901800	+ i 0.3709350926
3	-0.103612364039	+ i 0.896719200867	-0.0883460251	+ i 0.95820554298
4	-0.103612889227	+ i 0.8967204441	-0.088870156	+ i 0.854788817
5	-0.112217160388	+ i 0.412396334210	-0.11687715358	+ i 0.21680386299
6	-0.121310028246	+ i 0.2184358147279	-0.13749034	+ i 0.79969946
7	-0.15522016529	+ i 0.8450717997	-0.144346144486	+ i 0.910037309
8	-0.15525266720	+ i 0.84508066812	-0.186433	+ i 0.7453043
9	-0.2004630477669	+ i 0.376242360025	-0.19583946	+ i 0.54931158
10	-0.206476811	+ i 0.793784129	-0.19864610	+ i 0.86074946
11	-0.2068928490	+ i 0.7934407990	-0.204955511	+ i 0.376431414
12	-0.2274656214	+ i 0.6262969981	-0.23433	+ i 0.69346232
13	-0.25731571584	+ i 0.50203731043	-0.25180909	+ i 0.50264251
14	-0.258508467	+ i 0.741757503	-0.2521234	+ i 0.8108448
15	-0.25888061	+ i 0.7470464672	-0.270458582	+ i 0.325130263
16	-0.29752650276	+ i 0.34739229185	-0.28964	+ i 0.6550
17	-0.301051765	+ i 0.610862594	-0.305126	+ i 0.760702
18	-0.30816630	+ i 0.69260621	-0.30901	+ i 0.60793
19	-0.3243181	+ i 0.7103043	-0.34479	+ i 0.587438
20	-0.3705329	+ i 0.67457959	-0.35914	+ i 0.71123
	n=2, m=1		n=3, m=1	
1	-0.06028568955	+ i 0.88829765875	-0.08325397694	+ i 0.86436392104
2	-0.08789898037	+ i 0.352554927087	-0.105708407362	+ i 0.34640195338
3	-0.1088383407	+ i 0.8328933609	-0.11687792134	+ i 0.214919869761
4	-0.11200161615	+ i 0.939497219531	-0.1323924331	+ i 0.8097468023
5	-0.115514380221	+ i 0.215491816529	-0.13603545952	+ i 0.91671917468
6	-0.15810861	+ i 0.77858498	-0.182036372	+ i 0.755879315
7	-0.16729404595	+ i 0.8906185726	-0.190639836903	+ i 0.8674136555
8	-0.207591466	+ i 0.725077139	-0.2127794121	+ i 0.37123649827
9	-0.20931432998	+ i 0.37502653759	-0.23181786	+ i 0.70300722
10	-0.2214747313	+ i 0.8409753749	-0.244111241	+ i 0.551731632
11	-0.2282286376	+ i 0.5516823128	-0.2444955726	+ i 0.817569997
12	-0.249803052	+ i 0.5008719091	-0.251142783	+ i 0.499292178
13	-0.25796791	+ i 0.67522075	-0.2619068832	+ i 0.36144947997
14	-0.26313897737	+ i 0.34209716626	-0.2851531	+ i 0.655473
15	-0.275037018	+ i 0.790895108	-0.29784493	+ i 0.76744555
16	-0.30889763	+ i 0.6027732	-0.30736554	+ i 0.5978281
17	-0.32819903	+ i 0.74092549	-0.3468856	+ i 0.6237010
18	-0.3321112	+ i 0.6400873	-0.3509874	+ i 0.71809663
19	-0.3430168	+ i 0.6141604	-0.3762043	+ i 0.652416
20	-0.3829978	+ i 0.6929646	-0.4110346	+ i 0.677885

Table A.3: Eigenvalues for streamwise wavenumber m=1

A.2 Eigenfunctions

For streamwise invariant modes (m=0) the eigenfunctions are real and directly correspond to a velocity field of which a cross-section is visualized (as before) with color-coding for the axial component and arrows for the in-plane motion. For the sake of clarity of the in-plane pattern an optimal scaling of the arrows has been chosen for each mode. For the streamwise dependent modes (A.5,A.6) only the velocity field corresponding to the real part has been visualized, which is sufficient to see the spatial structure of the mode.

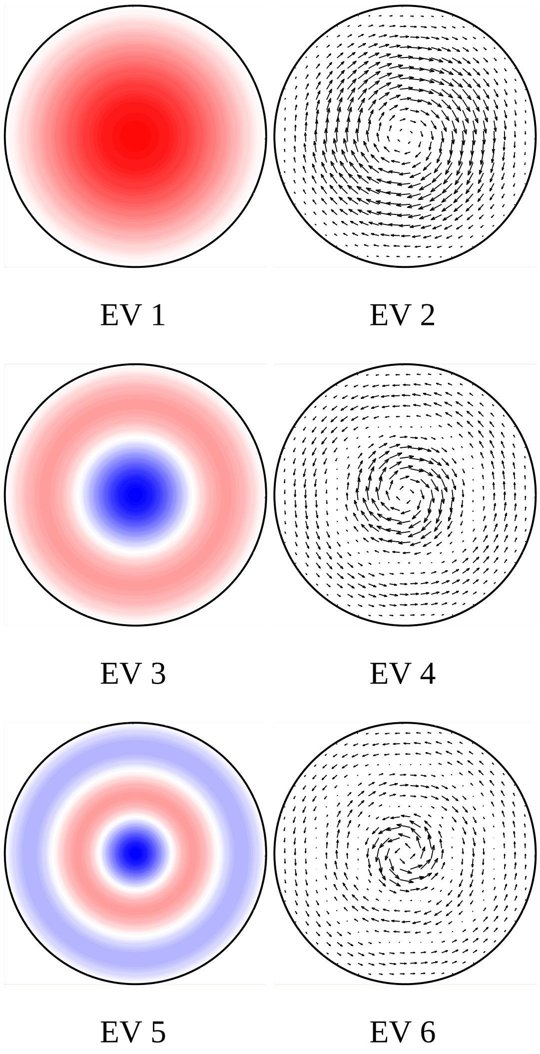

EV 1 EV 2

EV 3 EV 4

EV 5 EV 6

Figure A.1: Visualisation of the first six eigenvectors (EV) of the linearized Navier-Stokes operator at $Re = 3000$ for the streamwise and azimuthally invariant problem: (0,0)-mode. For the eigenvalues see table A.1.

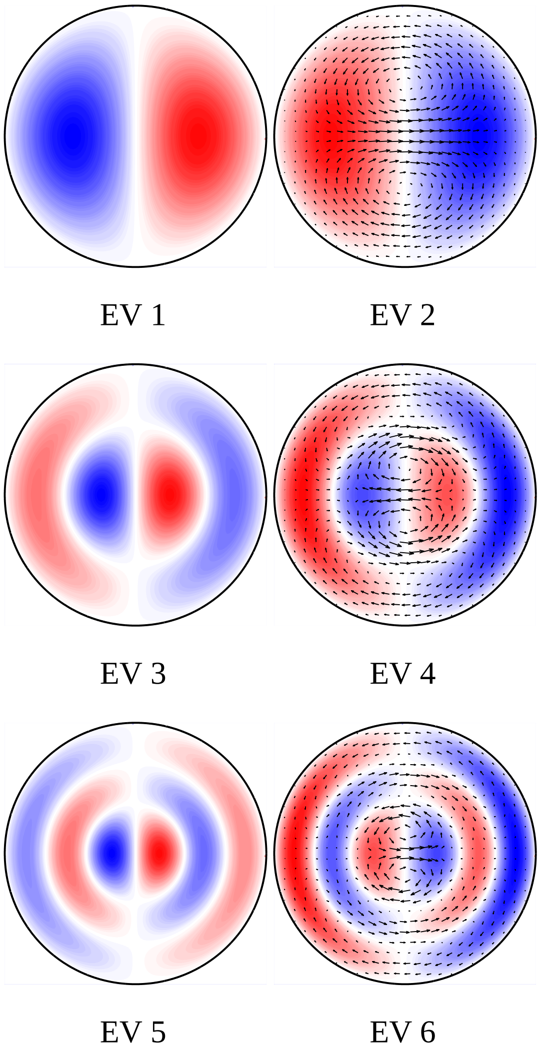

EV 1 EV 2

EV 3 EV 4

EV 5 EV 6

Figure A.2: Least stable eigenfunctions for the (1,0)-mode. For the eigenvalues see table A.2.

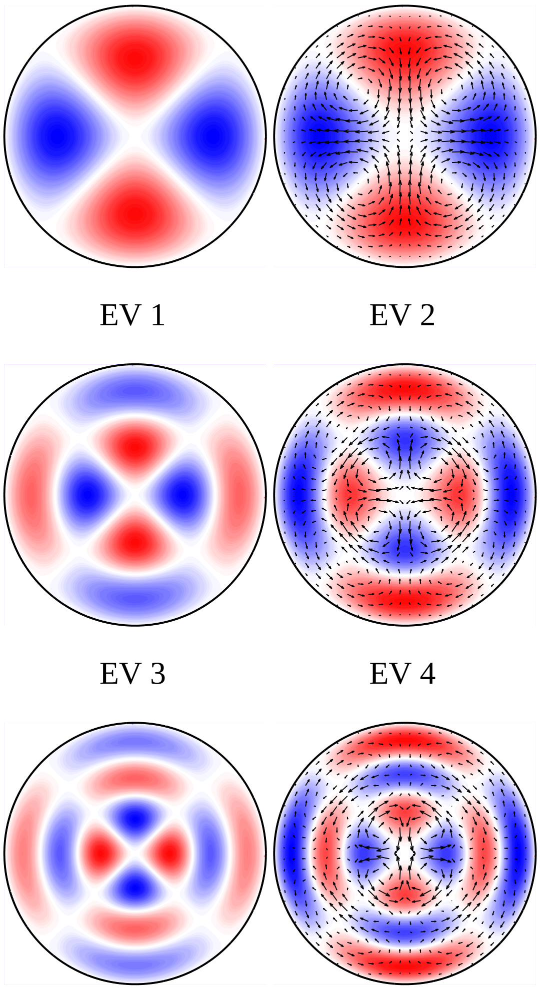

EV 1 EV 2

EV 3 EV 4

EV 5 EV 6

Figure A.3: Least stable eigenfunctions for the (2,0)-mode. For the eigenvalues see table A.2.

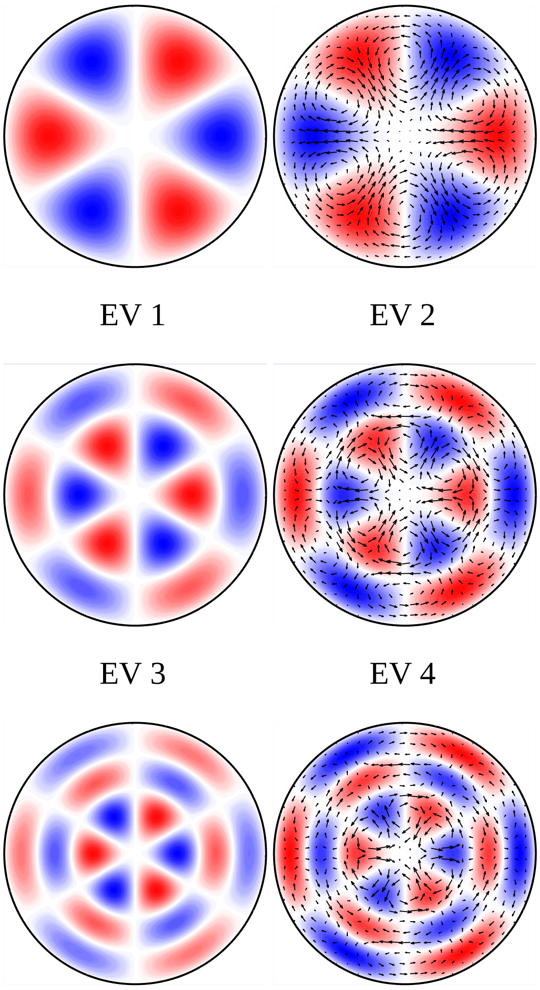

EV 1 EV 2

EV 3 EV 4

EV 5 EV 6

Figure A.4: Least stable eigenfunctions for the $(3,0)$-mode. For the eigenvalues see table A.2.

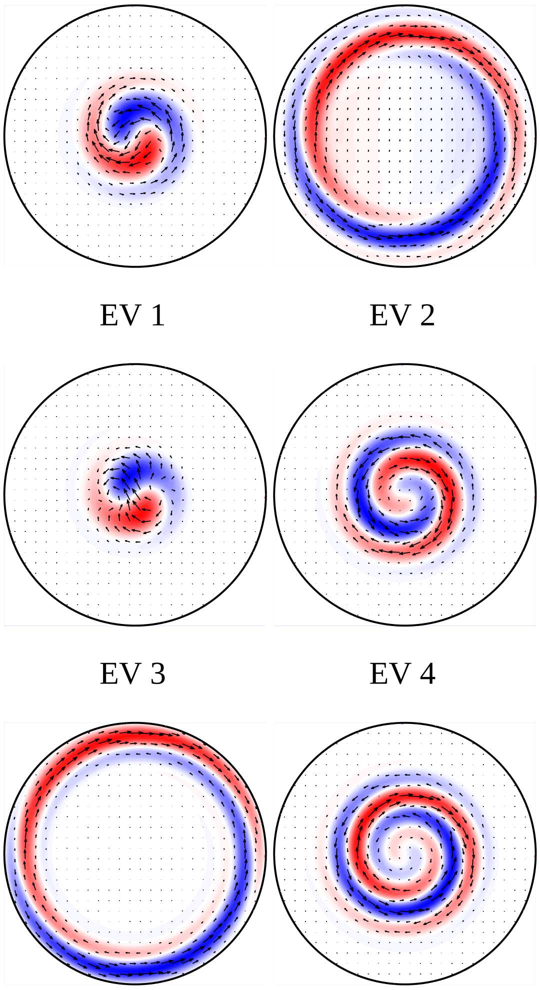

EV 1 EV 2

EV 3 EV 4

EV 5 EV 6

Figure A.5: Least stable eigenfunctions for the $(1,1)$-mode. Streamwise wavenumber is $k_z = 2$. Eigenvectors 2 and 5 are wall modes, EV's $1,3,4,6$ are center modes. For the eigenvalues see table A.3.

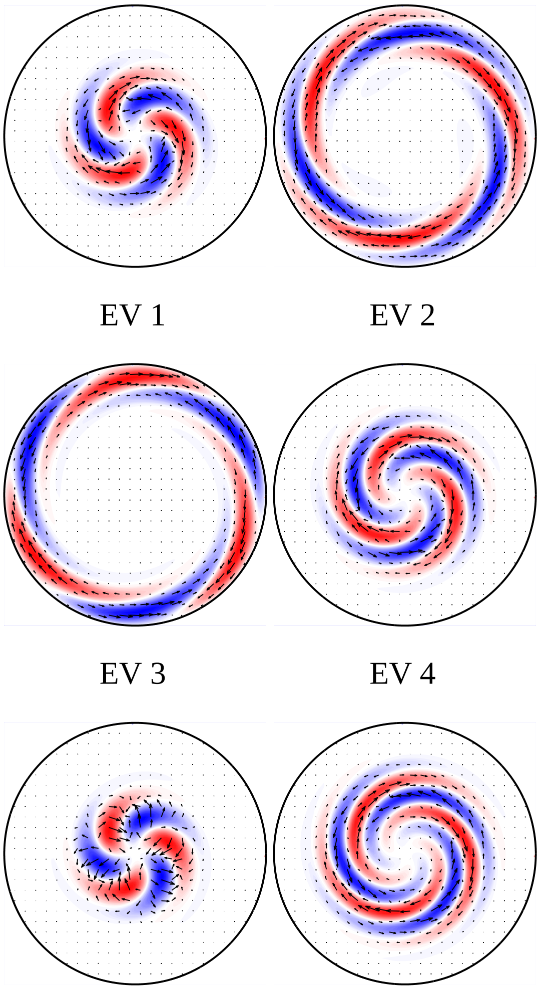

EV 1 EV 2

EV 3 EV 4

EV 5 EV 6

Figure A.6: Least stable eigenfunctions for the $(3,1)$-mode. Eigenvectors 2 and 3 are wall modes, EV's $1,4,5$, and 6 are center modes. For the eigenvalues see table A.3.

Appendix B Numerical convergence of travelling waves

For the travelling waves of C_n symmetry the structures of the velocity field in radial and azimuthal direction are getting smaller with increasing n like $1/n$. The effective resolution in azimuthal (and streamwise) direction stays the same for all C_n states as only integer multiples of the fundamental azimuthal wavenumber n are needed due to the symmetry of the state. This is in contrast to the radial resolution which can only be improved with considerably increased numerical efforts. The usual number of independent Fourier modes corresponding to $|n|/10+|m|/10 \leq 1$ is 66. The radial resolution is most critical and it is changed primarily. Figs. B.1 and B.2 show the changes in the turbulent friction due to the change in resolution.

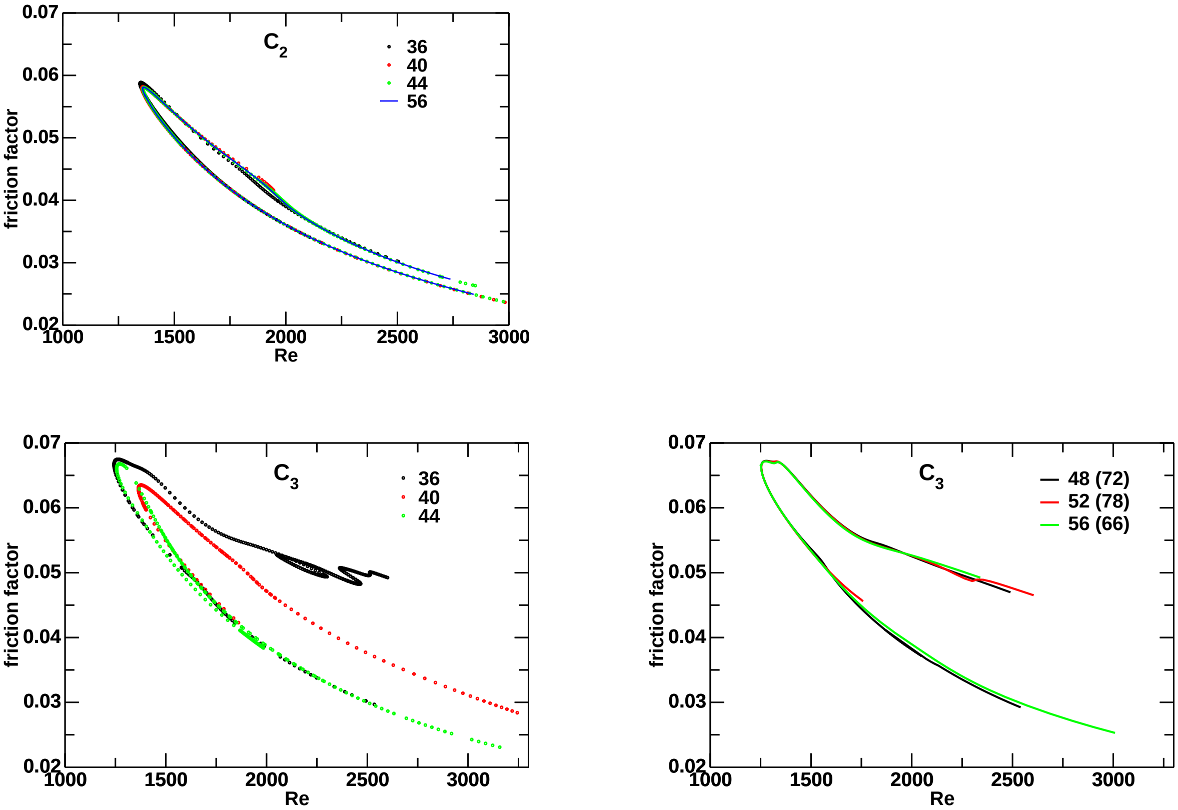

Figure B.1: Changes in the turbulent friction factor due to the change in spatial resolution for the C_2- and C_3-symmetric travelling waves. The C_2 state hardly changes when the number of Legendre polynomials is increased from 36 to 56. For the C_3 state 48 polynomials are necessary for numerical convergence: the lower right frame shows three different radial resolutions with three different numbers of Fourier modes (in brackets) that overlap.

The relative radial resolution is getting worse with increasing n and we already observe difficulties in accurately representing C_4 and C_5 .

In the following we show the amplitude spectra for the travelling waves of C_2, C_3, and C_4 symmetry, both for the Fourier modes and for the Legendre Polynomial expansion. No explicit piling up of energy can be observed at small scales. The C_2 state has shown to be nicely converged, the highest resolution seems appropriate for the C_3 state.

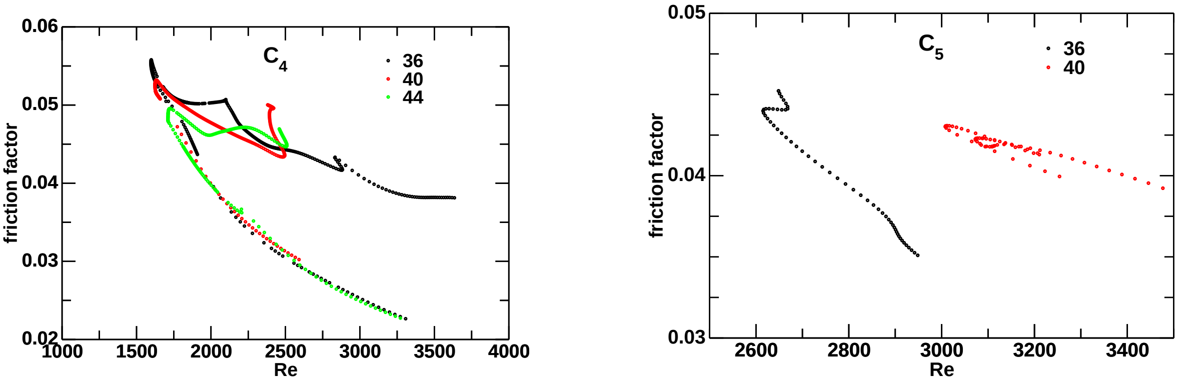

Figure B.2: Changes in the turbulent friction factor due to the change in radial resolution from 36 Legendre polynomials up to 44 for the C_n-symmetric travelling waves. The problems with convergence increase with n.

C_2-symmetric travelling wave

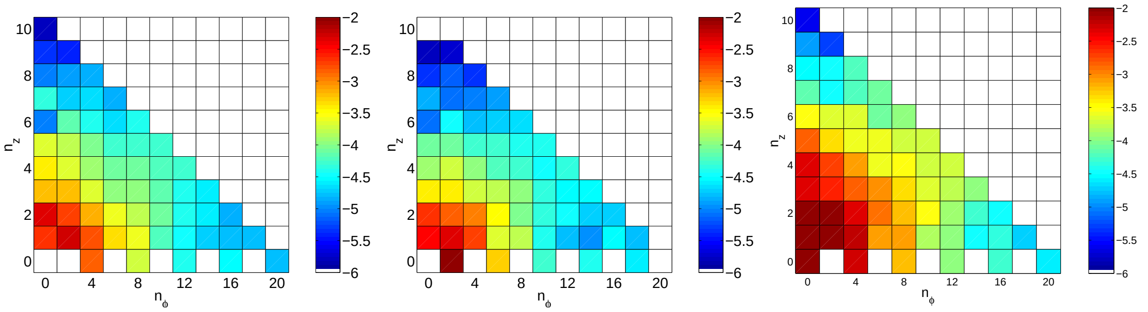

Figure B.3: Log$_{10}$ of the maximum amplitude of each Fourier mode for the C_2 wave

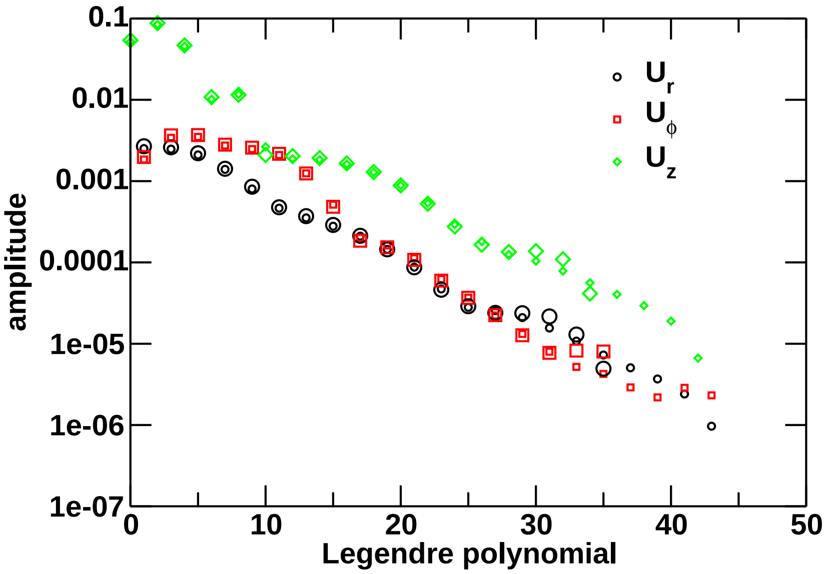

Figure B.4: Maximum amplitudes in the Legendre polynomial expansion, comparison 36 (large symbols) vs. 44 (small symbols) polynomials for the C_2 wave.

C_3-symmetric travelling wave

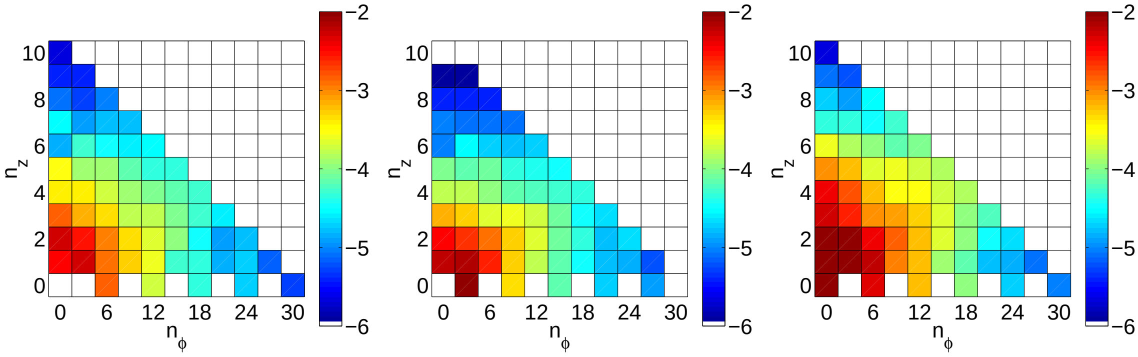

Figure B.5: Log_{10} of the maximum amplitude of each Fourier mode for the C_3 wave

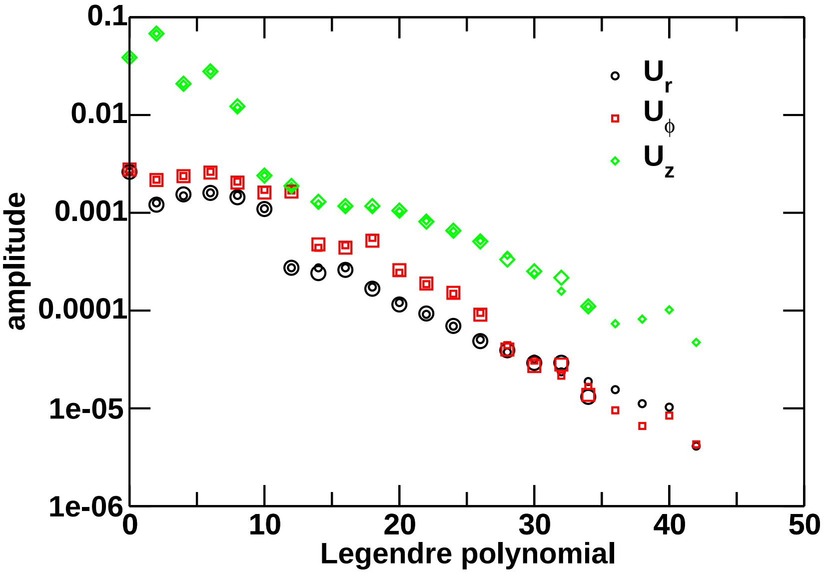

Figure B.6: Maximum amplitudes in the Legendre polynomial expansion, comparison 36 (large symbols) vs. 44 (small symbols) polynomials for the C_3 wave.

C_4-symmetric travelling wave

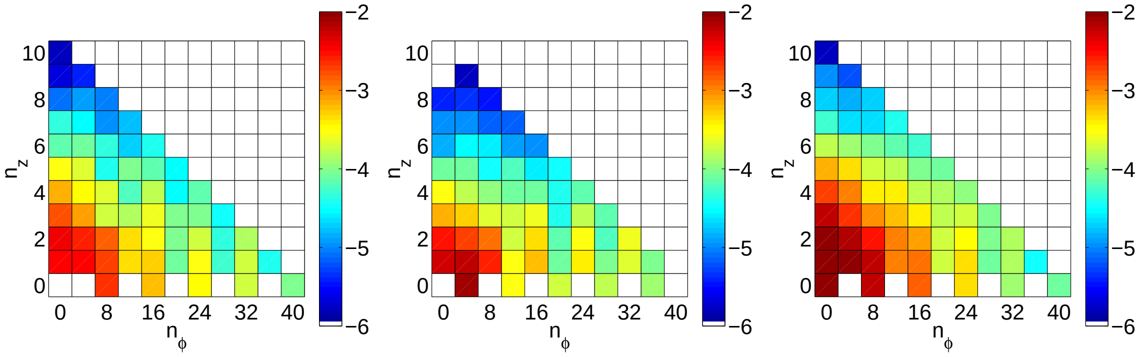

Figure B.7: Log_{10} of the maximum amplitude of each Fourier mode for the C_4 wave.

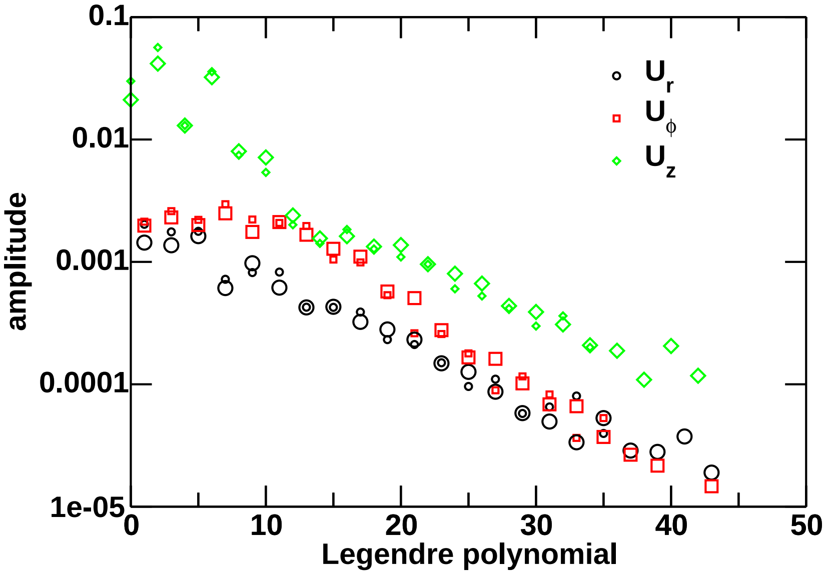

Figure B.8: Maximum amplitudes in the Legendre polynomial expansion, comparison 36 (large symbols) vs. 44 (small symbols) polynomials for the C_4 wave.

Appendix C Scaling at a complex boundary: the Mandelbrot set

The various types of behaviour that can arise when approaching a boundary of basins of attractions is presented here in a low-dimensional example.

Consider the simple map $z_n \to z_{n+1}$, $n \in \mathbb{N}$, where

$$z_{n+1} = z_n^2 + c\,. \tag{C.1}$$

The set of all those complex c-parameters for which the corresponding trajectory (orbit) $\{z_n\}$ that starts in $z_0 = 0$ does not escape to infinity is called the Mandelbrot set. For an introduction to the Mandelbrot set and related problems see [59] and references therein. Let us define the lifetime of a trajectory by the number of iteration it takes until it first leaves a circle of radius 2 around the origin, it is then known to tend to infinity. We want to draw the (loose) analogy between this escape to infinity to the decay of a turbulent trajectory in pipe flow.

We measure chaotic lifetimes for various complex parameters c starting at z_0=0. Parameter values with lifetimes larger than 100 are marked by black dots in Fig. C.1.

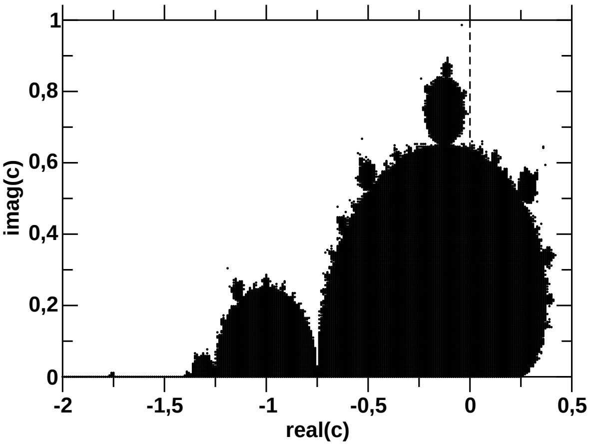

Figure C.1: Plane of the complex parameter c (see Eqn. C.1). Lifetimes larger than 100 are marked by black dots. The black area is a (poor man's) approximation to the Mandelbrot set. For the beauty of the Mandelbrot set see, for instance, [59].

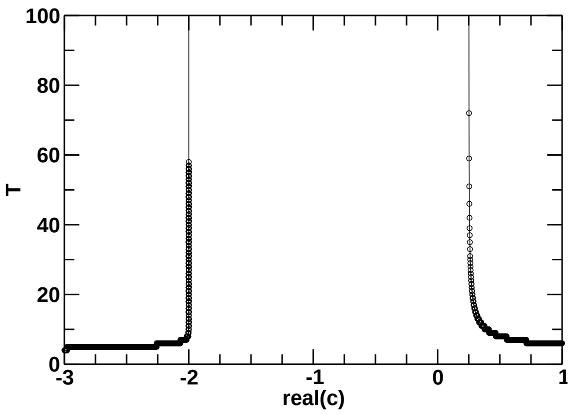

Figure C.2: Lifetimes for real parameters, $c \in \mathbb{R}$. Approaching the boundary of the Mandelbrot set at -2 from the left and at 0.25 from the right. The boundary region is magnified in Fig. C.3.

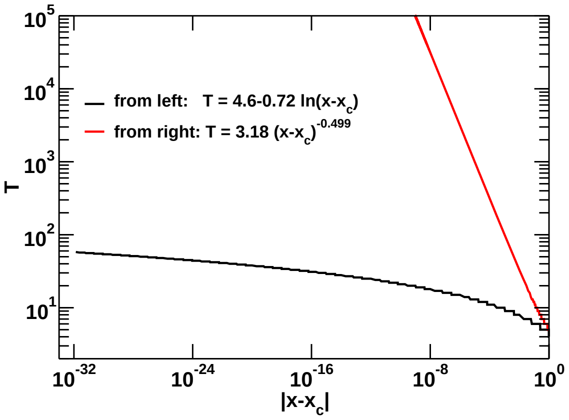

Figure C.3: Scaling of lifetimes T on the 'smooth' side of the boundary of the Mandelbrot set. Lifetimes vs. distance from the boundary for real parameters c.

In the following we approach the complex boundary of the Mandelbrot set along the horizontal (real) and vertical (imaginary) axis.

Horizontal cut

Choosing parameter values from the horizontal (real) axis, $c \in \mathbb{R}$, we approach the boundary from the left and from the right, see Fig. C.2. The left (right) threshold is exactly at -2 (0.25) and the scaling in their neighborhood is magnified in the following.

Approaching from the left, i.e. $c < 0$, calculations in quad precision are necessary in order to reach a maximum lifetime of 58 on the 'smooth' side of the boundary. Moving the initial condition by 10^{-35} to the right results in an increase in lifetime from 58 to infinity. Fig. C.3 shows the smooth logarithmic increase in lifetime when approaching the boundary of the Mandelbrot set.

Approaching from the right, i.e. for $c > 0$, the situation changes as now the lifetime diverges algebraically as $1/\sqrt{x - x_c}$. This is due to the tangential approach to the boundary, cf. Fig. C.1.

Vertical cut

Now we choose parameter values from the vertical (imaginary) axis. Only positive imaginary parts are needed as the problem has reflection symmetry with respect to the real axis. The lifetime as a function of the imaginary parameter is shown in Fig. C.4.

There is no longer a single well defined threshold but the lifetime shows a fractal dependence on the imaginary parameter and self-similarity. This is much closer to the fuzzy stability

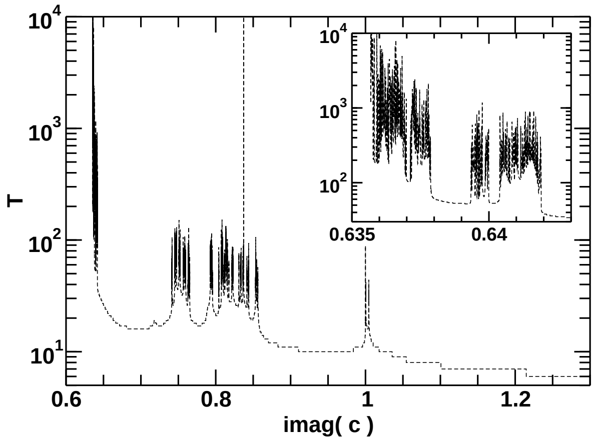

Figure C.4: Lifetimes for 10^5 parameters on the imaginary parameter axis. The inset shows a magnification of the region near the boundary of the Mandelbrot set. No clear scaling is observed for this vertical cut through the parameter plane, the lifetimes show a fractal dependence as a function of the parameter.

border observed in the high-dimensional pipe flow turbulence transition region.

In summary, the scaling of lifetimes can change dramatically with the direction of approach to the boundary, especially when approaching on a symmetry subspace (as is the case for real parameters c). It might, therefore, be interesting to approach the transition region in pipe flow by different families of initial conditions, especially with ones of highest spatial symmetry.

References

[1] P. Balakumar. Finite-Amplitude Equilibrium Solutions for Plane Poiseuille-Couette Flow. *Theoret. Comput. Fluid Dynamics*, **9**, 103–119, (1997).

[2] P.R. Bandyopadhyay. Aspects of the equilibrium puff in transitional pipe flow. *J. Fluid Mech.*, **163**, 439–458, (1986).

[3] D.R. Barnes, R.R. Kerswell. New results in rotating Hagen-Poiseuille flow. *J. Fluid Mech.*, **417**, 103–126, (2000).

[4] D.J. Benney. The evolution of disturbances in shear flows at high Reynolds numbers. *Stud. Appl. Math.*, **70**, 1–19, (1984).

[5] L. Bergström. Optimal growth of small disturbances in pipe Poiseuille flow. *Phys. Fluids A*, **5**(11), 2710–2720, (1993).

[6] L. Bergström. Self-sustained amplification of disturbances in pipe Poiseuille flow. *Eur. J. Mech. B*, **18**, 635–647, (1999).

[7] L. Boberg, U. Brosa. Onset of Turbulence in a Pipe. *Z. Naturforsch.*, **43a**, 697–726, (1988).

[8] S. Boccaletti, C. Grebogi, Y.-C. Lai, H. Mancini, D.Maza. The control of chaos: theory and applications. *Physics Reports*, (329), 103–197, (2000).

[9] S. Bottin, F. Daviaud, P. Manneville, O. Dauchot. Discontinuous transition to spatiotemporal intermittency in plane Couette flow. *Europhys. Lett.*, **43**(2), 171–176, (1998).

[10] U. Brosa. Turbulence without Strange Attractor. *J. Stat. Phys.*, **55**, 1303–1312, (1989).

[11] U. Brosa. *Z. Naturforsch.*, **46a**, 473, (1991).

[12] U. Brosa, S. Grossmann. Minimum description of the onset of pipe turbulence. *Eur. Phys. J. B*, **9**, 343–354, (1999).

[13] U. Brosa, S. Grossmann. Hydrodynamic vector potentials. *Eur. Phys.J B*, **26**, 121–132, (2002).

[14] C. Canuto, M.Y. Hussaini, A. Quarteroni, T.A. Zang. *Spectral Methods in Fluid Dynamics*. Springer-Verlag, (1988).

[15] A. Cherhabili, U. Ehrenstein. Finite-amplitude equilibrium states in plane Couette flow. *J. Fluid Mech.*, **342**, 159–177, (1997).

[16] E.B. Christiansen, H.E. Lemmon. Entrance region flow. *AIChE J.*, **11**, 995–999, (1965).

[17] R.M. Clever, F.H. Busse. Tertiary and quaternary solutions for plane Couette flow. *J. Fluid Mech.*, **344**, 137–153, (1997).

[18] D. Coles. Mechanique de la turbulence. *Paris: C.N.R.S.*, page 229, (1962).

[19] A.G. Darbyshire, T. Mullin. Transition to turbulence in constant-mass-flux pipe flow. *J. Fluid Mech.*, **289**, 83–114, (1995).

[20] M. Dhamala, Y.-C. Lai, E.J. Kostelich. Detecting unstable periodic orbits from transient chaotic time series. *Phys. Rev. E*, **61**(6), (2000).

[21] E.J. Doedel, H.B. Keller, J.P. Kernévez. Numerical analysis and control of bifurcation problems, part I : bifurcation in finite dimensions. *Int. J. Bifurcation and Chaos*, **1**(3), 493–520, (1991).

[22] C.W.H. van Doorne, J. Westerweel, F.T.M. Niewstadt. Stereoscopic PIV measurements of transition in pipe flow. In *Applications of laser techniques to fluid mechanics, 11th International Symposium*, (2002).

[23] A.A. Draad, G.D.C. Kuiken, F.T.M. Nieuwstadt. Laminar-turbulent transition in pipe flow for Newtonian and non-Newtonian fluids. *J. Fluid Mech.*, **377**, 267–312, (1998).

[24] P.G. Drazin, W.H. Reid. *Hydrodynamic Stability*. Cambridge University Press, (1981).

[25] B. Eckhardt. Periodic orbit theory. In G. Casati, I. Guarneri, U. Smilansky, editor, *Proceedings of the International School of Physics "Enrico Fermi", Course CXIX, Quantum Chaos*, pages 77–118. North Holland, (1993).

[26] B. Eckhardt, A. Mersmann. Transition to turbulence in a shear flow. *Phys. Rev. E*, **60**, 509–517, (1999).

[27] B. Eckhardt, H. Faisst, A. Schmiegel. Turbulence transition in shear flows. In I.P. Castro, P.E. Hanock, T.G. Thomas, editor, *Advances in turbulence IX*, page 701, Barcelona, (2002).

[28] J.G.M. Eggels, F. Unger, M.H. Weiss, J. Westerweel, R.J. Adrian, R. Friedrich, F.T.M. Nieuwstadt. Fully developed turbulent pipe flow: a comparison between direct numerical simulation and experiment. *J. Fluid Mech.*, **268**, 175–209, (1994).

[29] U. Ehrenstein, W. Koch. Three-dimensional wavelike equilibrium states in plane Poiseuille flow. *J. Fluid. Mech.*, **228**, 111–148, (1991).

[30] S. Eliahou, A. Tumin, I. Wygnanski. Laminar-turbulent transition in Poiseuille pipe flow subjected to periodic perturbation emanating from the wall. *J. Fluid Mech.*, **361**, 333–349, (1998).

[31] A. Esser, S. Grossmann. Analytic expression for Taylor-Couette stability boundary. *Phys. Fluids*, **8**(7), 1814–1819, (1996).

[32] H. Faisst. Transition from the Taylor-Couette system to the plane Couette system. Diplomarbeit, (1999).

[33] H. Faisst, B. Eckhardt. Transition from the Couette-Taylor system to the plane Couette system. *Phys. Rev. E*, **61**, 7227, (2000).

[34] H. Faisst, B. Eckhardt. Sensitive dependence on initial conditions in transition to turbulence in pipe flow. *to be published*.

[35] H. Faisst, B. Eckhardt. Travelling waves in pipe flow. *preprint nlin.CD/0304029*, (2003).

[36] http://gams.nist.gov, Guide to Available Mathematical Software. Module HYBRJ in MINPACK package.

[37] D. Gottlieb, S.A. Orszag. *Numerical Analysis of Spectral Methods*. SIAM, (1977).

[38] S. Grossmann. The onset of shear flow turbulence. *Rev. Mod. Phys.*, **72**, 603–618, (2000).

[39] J.M. Hamilton, J. Kim, F. Waleffe. Regeneration mechanisms of near-wall turbulence structures. *J. Fluid Mech.*, **287**, 317–348, (1995).

[40] G. Han, A. Tumin, I. Wygnanski. Laminar-turbulent transition in Poiseuille pipe flow subjected to periodic perturbation emanating from the wall. Part 2. Late stage of transition. *J. Fluid Mech.*, **419**, 1–27, (2000).

[41] P. Holmes, J.L. Lumley, G. Berkooz. *Turbulence, Coherent Structures, Dynamical Systems and Symmetry*. Cambridge University Press, (1996).

[42] A. Jachens. Numerische Verfahren zur Simulation der Rohrströmung in drei Dimensionen. Diplomarbeit, (2000).

[43] G. Kawahara, S. Kida. Periodic motion embedded in plane Couette turbulence: regeneration cycle and burst. *J. Fluid Mech.*, **449**, 291, (2001).

[44] M.J. Landman. On the generation of helical waves in circular pipe flow. *Phys. Fluids*, pages 738–747, (1990).

[45] A. Leonard, A. Wray. A new numerical method for the simulation of three dimensional flow in a pipe. In E. Krause, editor, *8th Int. Conf. on Numerical Methods in Fluid Dynamics*. Springer Verlag, Berlin, (1982).

[46] B. Ma, C.W. van Doorne, Z. Zhang, F.T.M. Nieuwstadt. On the spatial evolution of a wall-imposed periodic disturbance in pipe Poiseuille flow at $Re = 3000$. Part 1. Subcritical disturbance. *J. Fluid Mech.*, **398**, 181–224, (1999).

[47] P.A. Mackrodt. Stability of Hagen-Poiseuille flow with super-imposed rigid rotation. *J. Fluid Mech.*, **73**, 153–164, (1976).

[48] A. Meseguer, L.N. Trefethen. A spectral Petrov-Galerkin formulation for pipe flow. Technical report, Oxford University Computing Laboratory, Oxford, England, (2001).

[49] A. Meseguer. Streak breakdown instability in pipe Poiseuille flow. *Phys. Fluids*, **15**(5), 1203–1213, (2003).

[50] K. Mohseni, T. Colonius. Numerical treatment of polar coordinate singularities. *J. Comput. Phys.*, **157**, 787–795, (2000).

[51] M. Nagata. Three-dimensional finite-amplitude solutions in plane Couette flow: bifurcation from infinity. *J. Fluid Mech.*, **217**, 519–527, (1990).

[52] M. Nagata. Nonlinear solutions of modified plane Couette flow in the presence of a transverse magnetic field. *J. Fluid Mech.*, **307**, 231–243, (1996).

[53] M. Nagata. Three-dimensional traveling-wave solutions in plane Couette flow. *Phys. Rev. E*, **55**(2), 2023–2025, (1997).

[54] M. Nagata. Tertiary solutions and their stability in rotating plane Couette flow. *J. Fluid Mech.*, **358**, 357–378, (1998).

[55] E. Nino, C. Serio. Laser doppler velocimetry analysis of transitional pipe flow. *Eur. Phys. J. B*, **14**, 191–200, (2000).

[56] S. Novopashin, A. Muriel. Is the critical Reynolds number universal? *J. Exp. Theor. Phys.*, **95**(2), 262–265, (2002).

[57] P. Orlandi, M. Fatica. Direct simulations of turbulent flow in a pipe rotating about its axis. *J. Fluid Mech.*, **343**, 43–72, (1997).

[58] E. Ott, C. Grebogi, J.A. Yorke. Controlling chaos. *Phys. Rev. Lett.*, **64**(11), 1196, (1990).

[59] H.O. Peitgen, P.H. Richter. *The beauty of fractals. Images of complex dynamical systems*. Springer, (2000).

[60] W. Pfenniger. Transition in the inlet length of tubes at high Reynolds numbers. In G.V. Lachman, editor, *Boundary Layer and Flow Control*, pages 970–980. Pergamon, (1961).

[61] R. Piva. private communication,. (2002).

[62] S.B. Pope. *Turbulent Flows*. Cambridge University Press, (2000).

[63] W.H. Press, B.P. Flannery, S.A. Teukolsky, W.T. Vetterling. *Numerical Recipes*. Cambridge University Press, (1989).

[64] V.G. Priymak, T. Miyazaki. Accurate Navier-Stokes investigation of transitional and turbulent flows in a circular pipe. *J. Comp. Phys.*, **142**, 370–411, (1998).

[65] P.K. Ptasinski, F.T.M.Nieuwstadt, M.A. Hulsen, B.H.A.A. v. d. Brule. Experiments in turbulent pipe flow with polymer additives at maximum drag reduction. *Flow, Turbulence and Combustion*, **66**, 159–182, (2001).

[66] M. Quadrio, S. Sibilla. Numerical simulation of turbulent flow in a pipe oscillating around its axis. *J. Fluid Mech.*, **424**, 217–241, (2000).

[67] G. Reich, H. Beer. Fluid flow and heat transfer in axially rotating pipe. 1. Effect of rotation on turbulent pipe flow. *Intl. J. Heat Mass Transfer*, **32**, 551–561, (1989).

[68] O. Reynolds. An experimental investigation of the circumstances which determine whether the motion of water shall be direct or sinuous and the law of resistance in parallel channels. *Phil. Trans. R. Soc.*, **174**, 935–982, (1883).

[69] Y. Rubin, I.J. Wygnanski, J.H. Haritonidis. Further observations on transition in a pipe. In R. Eppler, F. Hussein, editor, *Laminar-Turbulent Transition*, pages 19–26. Springer, (1980).

[70] H. Salwen, F.W. Cotton, C.E. Grosch. Linear stability of Poiseulle flow in a circular pipe. *J. Fluid Mech.*, **98**, 273–284, (1980).

[71] H. Schlichting. *Boundary-Layer Theory*. New York: McGraw-Hill, (1979).

[72] P.J. Schmid, D.S. Henningson. Optimal energy density growth in Hagen-Poiseuille flow. *J. Fluid Mech.*, **277**, 197–225, (1994).

[73] A. Schmiegel, B. Eckhardt. Fractal stability border in plane Couette flow. *Phys. Rev. Lett.*, **79**(26), 5250–5253, (1997).

[74] A. Schmiegel. *Transition to turbulence in linearly stable shear flows*. PhD thesis, Philipps-Universität Marburg, (1999).

[75] H.G. Schuster. *Deterministisches Chaos*. VCH, Weinheim, (1994).

[76] H. Shan, B. Ma, Z. Zhang, F.T.M. Nieuwstadt. Direct numerical simulations of a puff and a slug in transitional cylindrical pipe flow. *J. Fluid Mech.*, **387**, 39–60, (1999).

[77] F.T. Smith, R.J. Bodonyi. Amplitude-dependent neutral modes in the Hagen-Poiseuille flow through a circular pipe. *Proc. R. Soc. Lond. A*, **384**, 463–489, (1982).

[78] P. So, E. Ott, S.J. Schiff, D.T. Kaplan, T. Sauer,C. Grebogi. Detecting unstable periodic orbits in chaotic experimental data. *Phys. Rev. Lett.*, **76**, 4705–4708, (1996).

[79] A. Solomonoff, E. Turkel. Global Collocation Methods for Approximation and the Solution of Partial Differential Equations. *ICASE Rep. No. 86-60 (NASA Langley Research Center, Hampton,VA)*, (1986).

[80] A. Spille. *Nichtlineare Stabilitätsanalyse der 3D-Couette-Strömung unter Berücksichtigung der Energietransfererhaltung*. PhD thesis, Univ. Oldenburg, (1999).

[81] K.R. Sreenivasan, C.M. White. The onset of drag reduction by dilute polymer additives, and the maximum drag reduction asymptote. *J. Fluid Mech.*, **409**, 149–164, (2000).

[82] J. Stoer, R. Bulirsch. *Introduction to numerical analysis*. Springer, (1983).

[83] P.A. Stone, F. Waleffe, M.D. Graham. Toward a Structural Understanding of Turbulent Drag Reduction: Nonlinear Coherent States in Viscoelastic Shear Flows. *Phys. Rev. Lett.*, **89**(208301), (2002).

[84] C.J. Swanson, B. Julian, G.G. Ihas, R.J. Donnelly. Pipe flow measurements over a wide range of Reynolds numbers using liquid helium and various gases. *J. Fluid Mech.*, **461**, 51–60, (2002).

[85] S. Thomae, S. Biermann. private communication,. (2003).

[86] N. Toplosky, T.R. Akylas. Nonlinear spiral waves in rotating pipe flow. *J. Fluid Mech.*, **190**, 39–54, (1988).

[87] L.N. Trefethen, A.E. Trefethen, S.C. Reddy, T.A. Driscol. Hydrodynamics stability without eigenvalues. *Science*, **261**, 578–584, (1993).

[88] L.N. Trefethen, S.J. Chapman, D.S. Henningson, A. Meseguer, T. Mullin, F.T.M. Nieuwstadt. Threshold amplitudes for transition to turbulence in a pipe. *http://xxx.uni-augsburg.de/abs/physics/0007092*, (2000).

[89] D.J. Tritton. *Physical Fluid Dynamics*. Oxford University Press, 2nd edition, (1988).

[90] C. Wagner, T.J. Hüttel, R. Friedrich. Low-Reynolds-number effects derived from direct numerical simulations of turbulent pipe flow. In *Proceedings of the Third Asian Computational Fluid Dynamics Conference*, volume **2**, (1998).

[91] F. Waleffe. Transition in shear flows. Nonlinear normality versus non-normal linearity. *Phys. Fluids*, **7**, 3060–3066, (1995).

[92] F. Waleffe. On a self-sustaining process in shear flows. *Phys. Fluids*, **9**, 883–900, (1997).

[93] F. Waleffe. Three-dimensional coherent states in plane shear flows. *Phys. Rev. Lett.*, **81**(19), 4140–4143, (1998).

[94] F. Waleffe. Exact coherent structures in channel flow. *J. Fluid Mech.*, **435**, 93–102, (2001).

[95] I.J. Wygnanski, F.H. Champagne. On transition in a pipe. Part 1. The origin of puffs and slugs and the flow in a turbulent slug. *J. Fluid Mech.*, **59**, 281–335, (1973).

[96] I.J. Wygnanski, M. Sokolov, D. Friedman. On transition in a pipe. Part 2. The equilibrium puff. *J. Fluid Mech.*, **69**, 283–304, (1975).

[97] O.Y. Zikanov. On the instability of pipe Poiseuille flow. *Phys. Fluids*, **8**(11), 2923–2932, (1996).

Zum Abschluß dieser Arbeit möchte ich all denen danken, die zu ihrer Entstehung direkt oder indirekt beigetragen haben.

Allen voran gilt mein Dank meinem Doktorvater, Herrn Prof. Bruno Eckhardt, insbesondere für die Vielzahl inspirierender Diskussionen mit ihm.
Ein Dankeschön geht auch an Prof. Peter Lenz für die spontane Bereitschaft zur Übernahme der Begutachtung dieser Arbeit.

Allen Mitgliedern der Arbeitsgruppe danke ich für das hervorragende Arbeitsklima.
Arne Jachens möchte ich danken für seinen Anteil an der Entwicklung des Rohrcodes sowie die zahlreichen Diskussionen über die Tücken der Rohrströmung.

Ein besonderer Dank gilt natürlich meiner Lebensgefährtin Andrea, die alle Höhen und Tiefen dieser Arbeit mitgetragen hat.